Physics of plasma plumes accelerated by magnetic nozzles: an experimental and theoretical research

by

Sara Correyero Plaza

A dissertation submitted by in partial fulfillment of the requirements for the degree of Doctor of Philosophy in

Mecánica de Fluidos Programa Interuniversitario

Advisors:

Eduardo Ahedo Galilea

Denis Packan

Tutor:

Eduardo Ahedo Galilea

April 2020

This thesis is distributed under license "Creative Commons **Attribution – Non Commercial – Non Derivatives**".

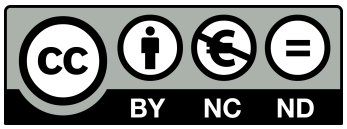

Dedicado a
mis padres y hermanas

Illustration by María Correyero

Contents

List of Tables

List of Figures

Acknowledgments

I will like to start thanking my Thesis supervisors, Eduardo and Denis, for giving me the opportunity of doing a PhD in one of the most amazing research fields I could have ever imagined. Eduardo, gracias por tu apoyo, sentido crítico y tu paciencia. Denis, thank you for making my stay at ONERA not only very successful, but also enjoyable and fun.

Gracias a mis padres, por haberme enseñado los valores que me han hecho llegar hasta aquí y que me van a acompañar siempre en la vida: trabajo, humildad, capacidad de superación, empatía y amor. Y gracias también por haberme dado lo mejor de mi vida: mis hermanas. María, hermana, amiga, compañera de piso y de vida, ya sabes que siempre vas a ser mi médico de referencia y yo tu paciente VIP. Gracias por quererme, cuidarme (y diagnosticarme) todo este tiempo. Lydia, mi pequeña guerrera, ni te imaginas lo que vas a llegar a conseguir en la vida. Aunque no te lo creas, tú me enseñas mucho más cada día que yo a ti. Gracias por ser como eres, tan cariñosa y especial. Las tres formamos un trío excepcional, y lo sabéis.

Gracias a la Comuna Summer Party, Rebe, Lau, Anita, Mari y Miri. No puedo tener un grupo de amigas mejor, gracias por entender que no puedo quedar porque estoy con la Tesis (ahora a ver que excusa pongo). Cuando tengamos 70 años nos vamos a reir mucho (más incluso que ahora) de todas las cosas que hemos vivido juntas. Os adoro.

Miri, gracias por esas cosas que solo tú y yo entendemos. Prométeme un Rajoy cuando sea Doctora, por favor.

Gracias a Laura, Eric y Andrés, por haberos quedado conmigo desde Lisboa. Es maravilloso teneros como amigos, y no sabéis lo afortunada que me siento de saber que estaréis ahí siempre.

Hablando de Lisboa...gracias a Marta. Porque no sé si te acuerdas, pero la primera entrevista que tuve para entrar en este grupo de investigación estaba en tu habitación y tú detrás dormida. Me debiste dar suerte, porque ese fue el primer paso que me ha llevado hasta aquí. Gracias por creer en mí como nadie, dentro de poco te toca a ti.

It's the turn for Paris. I want to thank all the team at ONERA for their

support, and their valuable comments and suggestions. Julien, I am deeply grateful for having the opportunity to work with you. You are an exceptional researcher, and I will always remember with affection all the moments we shared in the Lab. Paul-Quentin, I really need to thank you for making possible what we say in spanish "La niña bonita" of my PhD. Your idea of building a diamagnetic loop was very smart, and I appreciate a lot all your help and support. Théo, thank you for being the perfect Lab-mate. I am very grateful for all the moments we shared. Simon, Rafael, Julien (x3), Clement, Sebastien, thank you for all your support, comments and good mood.

Thank you Inside Voices Paris. Joining the choir was one of the most amazing experiences of my whole life. Thank you Sheilah, Morgane, Lucie, Viola, Philippe, and all the others. You were an incredible support during my stay in Paris. Thank you Notre Dame, for all the afternoons we spent together. This Thesis belongs to you. And thanks to my flatmates, Charlotte and Theodore. Thanks for being my family and taking care of me.

Gracias a todos los compañeros de doctorado del departamento de Ingeniería Aeroespacial de la UC3M y a los profesores. Un GRACIAS muy grande a Jaume, sabes que te admiro como profesional y como persona. Sin ti, esta Tesis hubiera sido muy diferente.

Gracias a Mick, por permitirme aprender de ti cada día. Eres la persona con la mente más brillante que he conocido nunca. Javi, gracias por ser como eres, de apasionado por la vida y buena gente. Quién nos iba a decir que un día íbamos a ser socios. Gracias por formar parte de ienai SPACE. Espero que esta locura nos lleve muy lejos y pongamos pronto nuestro primer cohete en el espacio.

Y por último, GRACIAS a la persona que ha hecho posible todo esto; por apoyarme y entenderme aunque no me entienda ni yo, por sacarme de mi zona de confort, por tu creatividad, por ser un feminista nato, por confiar en mi, por enseñarme a amar LIBRE. Sé que eres para toda la vida. Gracias, Dani.

This work was supported by the Spanish R & D National Plan (Grant No. PN ESP2016-75887) and by the European Union Horizon 2020 project MINOTOR, that has received funding from the research and innovation program under grant agreement No 730028.

Published and submitted content

The contents of the following publications are fully or partially included in this Thesis.

Paper 1

S. Correyero (SC), M. Merino (MM), P-Q. Elias (PQE), J. Jarrige (JJ), D. Packan (DP) and E. Ahedo (EA). "Characterization of diamagnetism inside an ECR thruster with a diamagnetic loop". *Physics of Plasmas*, **26**, 053511 (2019). DOI: 10.1063/1.5093980. The original idea is attributed to PQE. The experiments were carried out by SC under the supervision of JJ and DP. The paper has been written by SC, with feedback and comments by MM and EA. The contents are wholly included in Chapter 2 of this Thesis. Whenever material from this source is included in this thesis, it is singled out with typographic means and an explicit reference.

Paper 2

S. Correyero, J. Jarrige (JJ), D. Packan (DP) and E. Ahedo (EA). "Plasma beam characterization along the magnetic nozzle of an ECR thruster". *Plasma Sources Science and Technology*, **28**(9), 095004 (2019). DOI: 10.1088/1361-6595/ab38e1. The experimental work was carried out by SC, supervised by JJ and DP. EA provided support on the theoretical side. The paper has been written by SC, with feedback from DP and EA. The contents are wholly included in Chapter 3 of this Thesis. Whenever material from this source is included in this thesis, it is singled out with typographic means and an explicit reference.

Paper 3

E. Ahedo, S. Correyero, J. Navarro-Cavallé (JNC) and M. Merino. "Macroscopic and parametric study of a kinetic plasma expansion in a paraxial magnetic nozzle". *Plasma Sources Science and Technology*, **29**(4), 045017 (2020). DOI: 10.1088/1361-6595/ab7855. The research has been carried out by SC and EA, with comments

and feedback from MM and JNC. Results and figures have been obtained by SC. The text has been written by EA. The Appendix has been written by MM. The contents are wholly included in Chapter 4 of this Thesis. Whenever material from this source is included in this thesis, it is singled out with typographic means and an explicit reference.

Conference proceeding 1

S. Correyero, E. Ahedo and M. Merino. "Effect of the initial VDFs in magnetic nozzle expansions". In *36th International Electric Propulsion Conference*, paper IEPC-2019-818, Vienna, Austria, September 2019. Electric Rocket Propulsion Society. The paper has been written by SC, with feedback from MM. The contents are partially included in Chapters 4 and 5 of this Thesis. Whenever material from this source is included in this thesis, it is singled out with typographic means and an explicit reference.

Conference proceeding 2

S. Correyero, J. Jarrige, D. Packan and E. Ahedo. "Ion acceleration in the magnetic nozzle of an ECR thruster: Comparison of experimental measurements with a quasi 1D kinetic model". In *6th Space Propulsion Conference*, Seville, Spain, May 2018. Association Aéronautique et Astronautique de France. The experiments were carried out by SC and JJ, supervised by DP. Theoretical support was given by EA. This paper was awarded with the **best PhD Communication Award** by the Technical Committee of the Conference. The paper has been written by SC. The contents are partially included in Chapter 3 of this Thesis. Whenever material from this source is included in this thesis, it is singled out with typographic means and an explicit reference.

Conference proceeding 3

S. Correyero, J. Jarrige, D. Packan and E. Ahedo. "Measurement of anisotropic plasma properties along the magnetic nozzle expansion of an Electron Cyclotron Resonance Thruster". In *37th International Electric Propulsion Conference*, paper

IEPC-2017-437, Atlanta, GA, USA, October 2017. Electric Rocket Propulsion Society. The experiments were carried out by SC supervised by JJ and DP. Theoretical support was given by EA. The paper has been written by SC, with feedback from DP. The contents are partially included in Chapter 2 of this Thesis. Whenever material from this source is included in this thesis, it is singled out with typographic means and an explicit reference.

Conference proceeding 4

J. Jarrige, S. Correyero, P-Q. Elias, and D. Packan. "Investigation on the ion velocity distribution in the magnetic nozzle of an ECR plasma thruster using LIF measurements". In *37th International Electric Propulsion Conference*, paper IEPC-2017-382, Atlanta, GA, USA, October 2017. Electric Rocket Propulsion Society. The experiments were carried out by JJ and SC, with support from PQE and DP. The paper has been written by JJ. The contents are partially included in Chapter 3 of this Thesis. Whenever material from this source is included in this thesis, it is singled out with typographic means and an explicit reference.

Other research merits

The following material, although related, are not included in this Thesis.

Papers

- M. Wijnen, N. Aguera-López, S. Correyero and D. Pérez. "Cubesat lunar positioning system enabled by novel on-board electric propulsion". *IEEE Transactions on Plasma Science*, **46.2**, 319-329 (2018). DOI: 10.1109/TPS.2017.2779756. This project was awarded with the **Young Visionary Paper Award** for the excellent paper and presentation, in *37th International Electric Propulsion Conference*, Atlanta, GA, USA, October 2017. Electric Rocket Propulsion Society.

Conference proceedings

- S. Correyero, J. Navarro-Cavallé and E. Ahedo. "Expansion of a collisionless magnetized plasma plume with bi-Maxwellian electrons". In *52nd Joint Propulsion Conference*, Salt Lake City, Utah, USA, July 2016. American Institute of Aeronautics and Astronautics.

- S. Correyero, J. Navarro-Cavallé and E. Ahedo. "Kinetic modelling of collisionless electron cooling on magnetized plasma expansions".In *Space Propulsion Conference*, paper SP2016-3124949, Rome, Italy, May 2016. Association Aéronautique et Astronautique de France.

Poster sessions

- S. Correyero, J. Navarro-Cavallé and E. Ahedo. "Electron thermodynamics in the magnetized expansion of a rarefied plasma". In *14th Spacecraft Charging Technology Conference*, ESTEC, April 2016.

Additional scientific communications

- S. Correyero, T. Vialis, J. Jarrige and D. Packan."Plume Properties Measurement of an Electron Cyclotron Resonance Accelerator". Oral presentation at *69th Annual Gaseous Electronics Conference*, Bochum, Germany, October 2016.
- S. Correyero. "Study of plasma plumes accelerated by magnetic nozzles". Annual presentation at *Journées des doctorants* at ONERA, Palaiseau, Paris, January 2017.

Abstract

This Thesis presents an experimental and theoretical investigation of the fundamental physical phenomena behind magnetic nozzle expansions. The work is motivated by the emerging electric propulsion thruster concepts which include magnetic nozzles to confine and accelerate the plasma beam. This research has been carried out under a bilateral agreement between the *Office National d'Etudes et de Recherches Aérospatiales* and the *Electric Propulsion and Plasma Team* from the University Carlos III de Madrid.

The first part of this research constitutes an experimental investigation of an Electron Cyclotron Resonance thruster. An innovative procedure based on the integration of a diamagnetic loop signal at the thruster shutdown for estimating the mean perpendicular electron pressure inside the thruster source is presented. The signal is then used to estimate the mean perpendicular electron temperature by means of 1D and 2D theoretical models. Results fairly agree with the direct magnetic thrust measurements of a previous experiment.

The magnetic nozzle of the thruster is characterized by means of electrostatic probes and non intrusive diagnostics (laser induced fluorescence). Profiles for the ambipolar plasma potential, ion velocity, plasma density and electron temperature are obtained as functions of the propellant mass flow rate. By combining Langmuir probes measurements with the optical measurements, complete profiles (from the thruster source exit to far downstream) of the ambipolar plasma potential are obtained, which allows to estimate the total potential drop along the magnetic nozzle. Different effective electron cooling rates are measured along the expansion for the thruster operating with permanent magnets and for the one with solenoids, which is linked to the different magnetic nozzle topologies. The experimental data are compared with a paraxial steady-state model, showing a good correlation with respect the plasma potential, ion velocity and plasma density. The comparison between the experimental data and the model allows to estimate the sonic transition of the plasma flow, which appears to be shifted from the magnetic throat. A recent publication from another research group verifies our results.

The second part of this Thesis presents a theoretical investigation of the ion

and electron thermodynamics along the magnetic nozzle expansion. A collisionless, paraxial, steady-state kinetic model is used to investigate in several directions: first, the macroscopic effect of the kinetic aspects along the expansion is discussed. Electrons are barely affected by magnetic mirroring, since anisotropy is only developed very far downstream. On the contrary, magnetic mirror is dominant for ions, especially in the "hot" ions limit. Parametric laws for the downstream properties are given, which can provide a quick estimate of the nozzle performance.

The electron distribution function at the upstream source is formulated different from Maxwellian. The case of two electron populations with different temperatures is presented, where the kinetic features of a quasi-neutral steepened layer are addressed. The total potential drop of the nozzle is a function of the density fraction of hot electrons and their temperature, and it determines the level of anisotropy of this population.

Finally, the electron distribution function at the upstream source is formulated as a bi-Maxwellian anisotropic function. The plasma response along the expansion is investigated in a convergent-divergent nozzle and in an only divergent one. The magnetic mirror causes an isotropization effect in the convergent side, while increases the initial anisotropy on the divergent side. Additional potential and density gradients are developed as a consequence of expanding a species with a non-isotropic pressure tensor. The gradients sign depends on the convergent/divergent character of the nozzle and on the type of anisotropy.

Resumen

Esta Tesis presenta una investigación experimental y teórica acerca de los principios físicos que rigen la expansión del plasma en toberas magnéticas. Este trabajo está motivado por el surgimiento de nuevos conceptos de cohetes de propulsión eléctrica que incluyen toberas magnéticas para confinar y acelerar el chorro de plasma. Esta investigación ha sido llevada a cabo mediante un acuerdo bilateral entre el *Office National d'Etudes et de Recherches Aérospatiales* de París y el *Equipo de Propulsión Eléctrica y Plasmas* de la Universidad Carlos III de Madrid.

La primera parte de este estudio consta de una investigación experimental en un motor de resonancia ciclotrónica de electrones. Se presenta un procedimiento innovador basado en la integración de la señal de una bobina diamagnética durante el apagado del motor para estimar la temperatura perpendicular media de los electrones dentro de la fuente. La señal se utiliza para estimar la temperatura perpendicular media a través de modelos teóricos 1D y 2D. Los resultados están en línea con medidas directas de empuje magnético en el motor llevadas a cabo en una investigación anterior.

La tobera magnética del motor se ha caracterizado con sondas electrostáticas y fluorescencia inducida por láser. Los perfiles del potencial ambipolar del plasma, velocidad de iones, densidad del plasma y temperatura de electrones se han obtenido para distintos valores del gasto másico de propelente. Combinando ambas técnicas, se han obtenido perfiles completos (desde la salida del motor a aguas abajo en la pluma) del potencial ambipolar, lo que permite estimar la caída de potencial total en la tobera. Se han obtenido distintas velocidades de enfriamiento de electrones para el motor de imanes permanentes y el de bobinas, lo que está ligado a la diferencia en la topología magnética de sus toberas. Los datos experimentales se han comparado con un modelo paraxial estacionario, mostrando una buena correlación en los perfiles de potencial, velocidad de iones y densidad del plasma. La comparación del modelo con los datos experimentales permite estimar la posición de la transición sónica en la tobera, que parece estar desplazada de la garganta magnética. Una publicación reciente de otro grupo de investigación confirma nuestros resultados.

La segunda parte de esta Tesis presenta una investigación teórica acerca de la

termodinámica de iones y electrones en la tobera magnética. Un modelo cinético no colisional, paraxial y estacionario se ha utilizado para investigar en varias direcciones: primero, se discute el efecto macroscópico de los aspectos cinéticos de la expansión. Los electrones apenas están afectados por espejo magnético, ya que solamente desarrollan anisotropía muy aguas abajo. En cambio, el espejo magnético es un efecto dominante para los iones, especialmente en el caso de iones "calientes". Se han obtenido leyes paramétricas para las propiedades asintóticas del plasma, lo que permite realizar una estimación rápida de las actuaciones de la tobera.

La función de distribución de electrones en la fuente se ha formulado diferente a Maxwelliana. Se presenta el caso de dos poblaciones de electrones con distintas temperaturas, evaluando los aspectos cinéticos de una capa acusada cuasineutra. La caída de potencial total en la tobera depende de la fracción de electrones calientes y de su temperatura, y determina el grado de anisotropía de esta población.

Finalmente, la función de electrones en la fuente se ha formulado como una bi-Maxwelliana anisótropa. Se discute la respuesta del plasma en una tobera convergente-divergente y en una totalmente divergente. El espejo magnético causa una isotropización de la función de distirbución de electrones en la región convergente, mientras que aumenta el grado de anisotropía en la región divergente. Se desarrollan gradientes fuertes de potencial eléctrico y densidad como consecuencia de expandir una especie con un tensor de presiones anisótropo. El signo de los gradientes depende del carácter convergente/divergente de la tobera y del tipo de anisotropía.

CHAPTER

ONE

Introduction

"The Earth is the cradle of humanity, but mankind cannot stay in the cradle forever"
— Konstantin Tsiolkovsky

1.1 Space transportation: The role of Electric Propulsion

New worlds exploration has been linked to the humankind since time immemorial, driven by our inherent curiosity to discover unknown worlds. The same way in the early 16th Century European explorers were encouraged to cross the Atlantic ocean in the search for new horizons, in April 12th of 1961, the Soviet Union put the first man, Yuri Gagarin, in outer Space, laying the foundations of *Space Exploration*. Since this historic event, humankind has made great achievements with respect to Human Space Travel; February 20th of 1962, the American John Glenn became the first man to orbit the Earth; July 21th of 1969, astronaut Neil Armstrong walked on the moon; July 25th of 1984 Svetlana Savitskaya became the first woman to walk in space. Even more *incredible* goals related to Space Travel have been achieved if we remove from the equation the manned factor (which is limited by our biological nature); the first Satellite, Sputnik I, was launched in October 4th of 1957 by the Russians. December 15th of 1970, the Russian probe Venera 7 landed on Venus surface. The Voyager I, launched in September 5th of 1977 by the Americans, is still *operational* at 22.000 millions of km from Earth. To have a global view, some of the main achievements of Space Exploration are represented in a timeline in Figure 1.1.

Undoubtedly, all of these milestones would have never been possible without the development of space rocketry. Konstantin Tsiolkovsky, in 1903, published the *ideal*

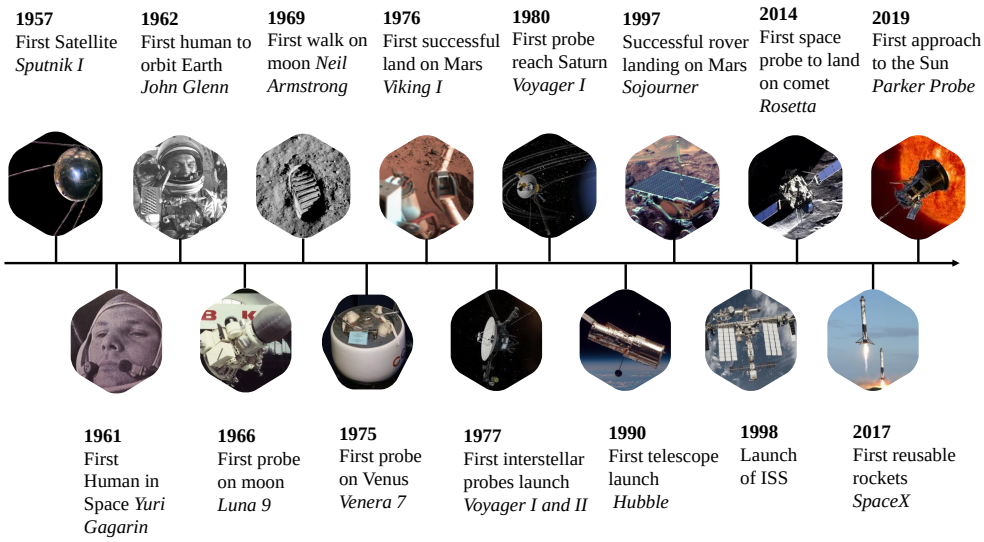

Figure 1.1: Timeline of main achievements in Space Exploration

rocket's equation,

$$\Delta V = v_e \log \frac{m_0}{m_f}, \tag{1.1}$$

where ΔV is the total change in velocity of a spacecraft which ejects mass at a constant exhaust velocity v_e, decreasing its total mass from m_0 to m_f, without external forces. This equation, apparently simple, reveals a critical aspect of space transportation: If a significant fraction of the initial mass needs to be brought to the final velocity, exhaust velocities of the order of ΔV shall be provided. Notice that if the total ΔV required for a specific mission is higher than the exhaust velocity of the propellant, a large amount of the total rocket mass may be needed only for propellant mass. For instance, the Saturn V rocket, which took astronauts to the Moon within the Apollo NASA program, was 85 % propellant mass. However, the total required ΔV varies significantly from one mission to another; from Earth to Low Earth Orbit (LEO), 10^4 m/s; from LEO to Geostationary Earth Orbit (GEO), $4 \cdot 10^3$ m/s; from LEO to Mars Orbit, $7 \cdot 10^3$ m/s [65].

Instead of the exhaust velocity, the Specific Impulse *Isp* is commonly used due

to historical reasons, and it is defined by

$$Isp = \frac{u_e}{g_0}, \tag{1.2}$$

where g_0 is the gravitational acceleration at sea-level.

Together with the Isp, the total thrust of the rocket T, given by (1.3), constitute the two main figures of merit of a spacecraft propulsion system. Notice that $\dot{m}$ represents the propellant mass flow rate.

$$T = \dot{m} u_e \tag{1.3}$$

Rockets can be generally classified into two main categories: chemical and electric. In the first group, the maximum Isp is an internal characteristic of the propellant, since it depends directly in its calorific energy. Conversely, in an electric rocket, the Isp is external to the propellant, and depends on how much electric energy can be transferred into it. Nowadays, the main limitation in electric rockets is the available on-board power. Actually, the large amount of thrust and power needed for launching a vehicle from Earth to the outer Space, makes chemical propulsion the exclusive solution for launchers. However, for spacecraft on-board propulsion, electric rockets are becoming a main player. The fact that they can achieve much larger Isp implies that a significant fraction of propellant mass can be saved (and therefore a significant amount of money). But apart from the economical point of view, electric engines also open a whole new scope of more ambitious interplanetary missions, which may be unfeasible with chemical rockets, due to the large ΔV they require.

Within the electric rockets, it is important to distinguish between the *ion-driven* and the *non-ion-driven* devices. The first ones use electric energy to accelerate the propellant carried within the spacecraft, while the ones from the second group do not expel propellant (e.g., solar sails, electrodynamic tethers, photonic thrusters). Regarding the ion-driven, also named *plasma* thrusters, a first category can be established in terms of the dominant term in the plasma momentum equation

$$m_i n_i \left(\mathbf{u}_i \cdot \nabla\right) \mathbf{u}_i = -\nabla \cdot \overline{\overline{p}} - e\left(n_i - n_e\right) \nabla\phi + \mathbf{j} \times \mathbf{B}. \tag{1.4}$$

In (1.4), electron inertia has been neglected, m_i is the ion mass, n_i and n_e the ion and electron densities respectively, $\mathbf{u}_i$ the ion fluid velocity, $\overline{\overline{p}}$ the pressure tensor, ϕ the electric potential, $\mathbf{j}$ the electric current density and $\mathbf{B}$ the magnetic field.

The electric propulsion devices (ion-driven) can be classified into:

- *Electrothermal*: The propellant is first heated electrically and then accelerated gas-dynamically. The first term in the right hand side of (1.4) dominates.
- *Electrostatic*: A non-neutral plasma is electrically accelerated. The expansion is dominated by the second term in the right hand side of (1.4).
- *Electromagnetic*: Governed by the Lorentz force, last term of (1.4), as a result of the interaction between magnetic fields (external and internal) and electric currents in the plasma.

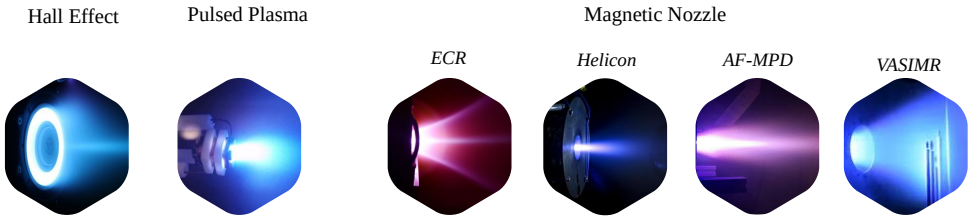

Figure 1.2: Classification of electromagnetic thrusters

Among the electromagnetic thrusters, the most extended are the Hall Effect Thruster (HET) [46, 3] the Pulsed Plasma Thruster (PPT) [29] and those which include a magnetic nozzle to accelerate and confine the plasma beam. The research performed in this Thesis, although is not restricted to, applies mainly to the last subgroup, which include the Electron Cyclotron Resonance Thruster (ECRT) [112, 68], the Helicon Plasma Thruster (HPT) [102, 20, 33, 97], the the applied-field magnetoplasmadynamic thruster (AF-MPD) [15, 72], and the Variable Specific Impulse Magnetoplasma Rocket (VASIMR)[48]. The main performance parameters of these devices are summarized in Tab. 1.1, where **Isp** represents the Specific Impulse, η the thruster efficiency, **T/W** the thrust to power ratio, and **TRL** the maturity of the technology (Technology Readiness Level defined in [4]). Magnetic

nozzle thrusters have not flown yet in Space, since their level of development, both theoretical and experimental, is still low (TRL ≤ 5). Next Section describes the main principles of operation of these devices, as well as the main challenges that must be addressed before they become a competitive technology for the future of electric propulsion.

	HET	**PPT**	**ECRT**	**HPT**	**AF-MPD**	**VASIMR**
Isp (s)	1500-3000	300-3000	1000	500-1500	400-9000	3000-5000
η (%)	≤ 60	≤ 20	≤ 20	≤ 15	≤ 40	≤ 60
T/W (mN/kW)	10-50	≈ 20	≈ 30	≈ 20	5-40	25
TRL	9	8	4-5	4-5	4	5

Table 1.1: Main performance of the different electromagnetic thrusters available in the Literature [103, 86, 19, 108, 71, 66, 7]

1.2 Physics of Magnetic Nozzles

A magnetic nozzle (MN) is, in essence, a convergent-divergent magnetic field created by a set of solenoids or permanent magnets, whose main goal is to accelerate and confine the plasma beam, and to eventually give rise to magnetic thrust. The underlying principles behind the operation of a MN are schematized in Figure 1.3 and summarized as follows, with particular emphasis on those studied in this Thesis.

1.2.1 Main working principles and involved phenomena

Ambipolar plasma potential

In the vicinity of the magnetic throat (location of maximum magnetic field strength), a hot current-free plasma is generated. In the applied magnetic field, electrons follow a spiral motion around the magnetic field lines, and remain confined and attached to them, in the absence of collisions. Conversely, a much larger magnetic field strength is needed to magnetize ions and in most cases, except for the VASIMR, ions remain only partially magnetized. As electrons expand following the magnetic field lines, since the plasma tends to remain quasi-neutral (macroscopically neutral), an ambipolar electric field develops in the expansion, which

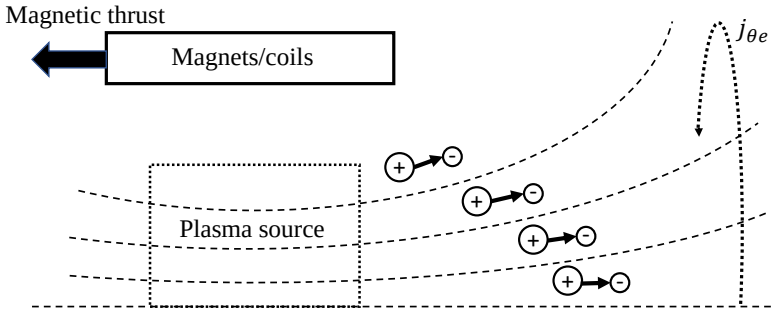

Figure 1.3: Schematic of the working principles of a magnetic nozzle

accelerates ions downstream and confines electrons upstream; only a small fraction of the most energetic electrons will be able to overcome the potential drop and neutralize the ion current beam. By means of this ambipolar plasma potential, the magnetic nozzle transfers internal energy of electrons into ion kinetic energy.

Plasma acceleration mechanisms

The ambipolar plasma potential constitutes the main acceleration mechanism of a magnetic nozzle [9, 17, 80]. However, other acceleration mechanisms can also take place in the MN expansion. For some devices with strong magnetic fields, ions can also be accelerated due to the inverse magnetic-mirror effect, which "repels" both ions and electrons downstream from the magnetic throat. In specific MN thrusters, which expand two electron species with disparate temperatures, the quasi-double-layer can also constitute an important acceleration mechanism [31, 39, 138, 120].In the AF-MPD thruster, three additional phenomena can be identified; electrothermal, swirl, and self-field accelerations [72].

Plasma detachment

After the plasma has been accelerated, it needs to separate from the magnetic field lines. Merino and Ahedo demonstrated that the ambipolar electric field far downstream, compared to ion inertia, is not sufficient to drag ions with electrons

in the magnetic stream tubes, even in the case of fully magnetized electrons [89]. Recently, Little and Choueiri experimentally investigated electron demagnetization in a magnetically expanding plasma, founding that their results fairly agree with Merino's and Ahedo's theory.

Magnetic thrust generation

Magnetic thrust F_m in a magnetic nozzle is due to the contribution of both surface and volume azimuthal currents (of both ions and electrons), and can be expressed as

$$F_m = -\int j_\theta B_r dV - \int J_\theta B_r dS, \tag{1.5}$$

where j_θ is the azimuthal current density and J_θ is the surface Hall current per unit length [87]. Notice that these two currents are of the same nature, but J_θ is concentrated on a thin layer. In a nozzle where $B_r > 0$ (i.e., a divergent nozzle with B pointing downstream or a convergent nozzle with B pointing upstream), a positive thrust implies a major contribution of the negative azimuthal currents, thus, a net diamagnetic azimuthal current. Although the major contribution of azimuthal currents in a MN is diamagnetic, paramagnetic currents can develop in high magnetized plasmas (ion swirl currents) [92]. When these diamagnetic currents interact with the radial component of the applied magnetic field, they generate an axial Lorentz force in the forward direction. The reaction to this force is felt by the magnets/coils, and is the main contribution to the magnetic thrust. As it will be seen in Chapter 2, the azimuthal internal currents are also responsible for the longitudinal induced magnetic field, which is related to the perpendicular plasma pressure. One of the main contributions of this Thesis has been to design, develop, calibrate and test a diamagnetic loop in order to estimate the perpendicular electron pressure inside an ECR thruster.

Collisionless electron cooling

The electron thermodynamics in a MN is still an open topic of research. As it is shown in Chapter 3, an effective electron cooling with a polytropic coefficient varying between 1.1 and 1.5 has been found in the MN of an ECR thruster, which

correlates well with the values found in the Literature [78, 75]. However, this experimental finding is not well justified, and therefore limits the development of exact predictive models for MN thrusters. The MN mainly converts electron thermal energy into parallel kinetic ion energy, so understanding the electron thermodynamics is crucial for the further development of these devices. The physical problem is far from obvious; some of the controversial points are listed below.

- Most electrons are confined by the ambipolar electric potential, but an isothermal assumption leads to an unbounded plasma acceleration and an infinite source of energy.
- The development of *anomalous* collisionless heat fluxes has been demonstrated, but a closure law for the fluid equation hierarchy is not evident.
- The magnetic mirror effect "repels" particles from the magnetic throat, which together with the ambipolar electric field, leads to a spatial region in the divergent nozzle where electrons could be "doubly-trapped". The formulation of the energy distribution function of this (sub)population is unknown since it is disconnected from the upstream source.
- Plasma conditions at the upstream source can differ from Maxwellian, and the implications in the expansion dynamics are still unclear.

All these phenomena challenge the understanding of the electron thermodynamics in the MN, and are the basis for the theoretical research of Chapters 4, 5 and 6.

1.2.2 Magnetic Nozzle Thrusters

Despite their early stage of development, the reason why MN thrusters have generated interest in the industry is because they hold potential advantages with respect to other propulsion systems. The plume is quasi-neutral without the need for a cathode or neutralizer, which reduces costs and complexity of the overall system. The neutralizer is commonly the life-limiting factor of other propulsion systems such as ion or Hall thrusters; removing this component also allows to operate within a wide variety of low-purity propellants. Furthermore, MN could potentially do thrust vectoring by operating with various sets of coils [94].

Although the mechanisms listed in the previous subsection constitute some of the main working principles of all-type MN thrusters, different phenomena can acquire special relevance depending on the type of engine, due to specific plasma generation mechanisms and/or different magnetic nozzle topologies and/or strengths.

The ECR thruster

In general terms, the Electron Cyclotron Resonance (ECR) thruster consists of an ECR source followed by a MN, which is commonly generated by the same set of coils/magnets that generate the magnetic field inside the source. The ECR is a well known phenomenon in plasma physics. Its main principle relies on the circular motion that a charged particle acquires when entering a uniform magnetic field, due to the Lorentz force. The angular frequency of this motion ω is given by

$$\omega = \frac{eB}{m} \tag{1.6}$$

where m, e and B are the particle mass, the elementary charge and the magnetic field strength, respectively. In this scenario, if an electromagnetic wave is propagated at the same frequency as the natural frequency of electrons given by (1.6) and with at least one component of Right Hand polarization, electrons enter in resonance with the wave, and efficiently absorb almost the entirety of the wave power. Most of the existing ECR thrusters work in the GHz frequency range, and therefore they need magnetic field strengths in the order of 10^{-1} T. At lower frequencies, the magnetic fields will be lower, but also the electron magnetization. The scaling laws for an ECR thruster are not obvious, and they constitute a current research topic on their own.

In most of the existing ECR thrusters, the magnetic field inside the source is not uniform, and the resonance condition is only located in a narrow region of the plasma source. In this region, electrons reach very high temperatures in the perpendicular direction to the magnetic field lines. However, collisional phenomena inside the source, which mainly involve electrons with heavy species, tend to decrease this temperature and homogenize the electron distribution function.

Due to the heating mechanism of an ECR source, the electron distribution function can be different from Maxwellian when entering the MN. In particular, the perpendicular electron temperature could be larger than the parallel one. This

phenomenon is highly conditioned by the propellant mass flow rate. In principle, it is expected that at lower mass flow rates, the perpendicular electron temperature increases, as well as the degree of temperature anisotropy. To better understand this phenomenon and its implications in the performance of the ECR thruster, it is crucial to characterize experimentally the plasma properties of the MN at different operational conditions. With this motivation, Chapter 3 presents a detailed experimental characterization of the main plasma properties along the MN of the ECR thruster developed by ONERA.

The Helicon thruster

The basic design of an HPT consists of a plasma source where the propellant is injected, wounded by a RF antenna, and surrounded by a set of coils/magnets. Inside the source, the role of the magnetic field is to allow the propagation of different kinds of electromagnetic waves. The main apparent advantage of the plasma source of a HPT is that it produces a higher plasma density than other devices, which makes it very attractive for the space propulsion community. However, the reported efficiencies are considerably low, and the understanding of the wave propagation is still limited.

A special variant of the HPT deserves special attention: the Double-Layer HPT. The main principle relies on an additional plasma acceleration due to a steepened potential drop located in a thin region of the MN. The main reason for this potential jump seems to be related to the existence of a small population of very "hot" electrons already at the upstream source. Although it does not constitute a thrust generation mechanism, it poses questions related to the plasma thermodynamics. For instance, what should be the fraction of "hot" electrons in order to obtain the maximum plasma acceleration for the same mean plasma temperature? What are the roles of the trapped and free electrons in the macroscopic fluid moments? This topic has been addressed theoretically in Chapter 5.

The VASIMR thruster

The VASIMR thruster has been developed by Ad Astra Rocket Company, leaded by the astronaut Dr. Franklin Chang-Díaz. The plasma source consists of two consecutive stages: an HPT source followed by an Ion Cyclotron Resonance (ICR)

source. This thruster is designed to be a very high power electric propulsion system (≈ 200 kW), and needs magnetic fields in the order of 2 T. What makes the VASIMR unique with respect to other propulsion systems is the intermediate ICR plasma heating source. A large amount of energy is deposited into the perpendicular ion velocity component, leading to a potential large anisotropy of the ion distribution function, and to an ion-driven plasma expansion.

The generated plasma is expected to differ significantly from other plasma propulsion sources, with ion temperatures in the order or higher than electron temperatures, which could potentially modify the expansion dynamics. A preliminary study of the MN expansion with "hot" ions is presented in Chapter 4.

AF-MPD thruster

The Applied Field MPD thruster is a variation/improvement of the Self-Field (SF) MPD thruster. Both of them consist of a central cathode placed coaxially with an external annular anode. Strong radial currents j_r flow from the anode to the cathode, generating an azimuthal magnetic field B_θ. The Lorentz force given by $j_r B_\theta$ accelerates the plasma downstream. Due to the strong radial currents, the SF-MPD has significant plasma losses to the walls, and the life of the cathode is a life-limiting factor. In order to solve this issue, the AF-MPD includes a set of solenoids/magnets which induce a magnetic field parallel to the cathode and anode walls, reducing the total losses. This applied field generates a MN which is then used to accelerate more the plasma beam.

The strong longitudinal currents and the 3D topology of the plasma expansion due to a high rotation of the plasma beam makes the MN of the AF-MPD rather unique. The study of these particular phenomena has not been addressed in this Thesis.

1.3 Thesis scope and objectives

The ultimate goal of the present Thesis is to contribute to the understanding of the physical phenomena behind MN expansions. An experimental and theoretical research has been carried out in two different institutions under a bilateral collaboration agreement, and therefore it is divided in two main parts.

- 18 months at the *Office National d'Etudes et de Recherches Aérospatiales* (ONERA), Palaiseau, Paris, France. The main objective has been to investigate and characterize the plasma properties along the MN of the Electron Cyclotron Resonance Thruster developed by ONERA. Two versions of this thruster have been tested, with the magnetic field created by a permanent magnet and by a set of solenoids. Photographs of the two versions are shown in Figure 1.4.

  During the course of this Thesis, different diagnostics have been used in order to characterize the MN of the ECR thruster. Particularly, electrostatic probes (Faraday, emissive and Langmuir) and Laser Induced Fluorescence (LIF). These diagnostics have been combined in order to obtain complete longitudinal profiles of the main plasma properties at different operating conditions. As well, one of the main contributions has been to develop a diamagnetic loop to estimate the mean perpendicular plasma pressure inside the thruster and along the MN.

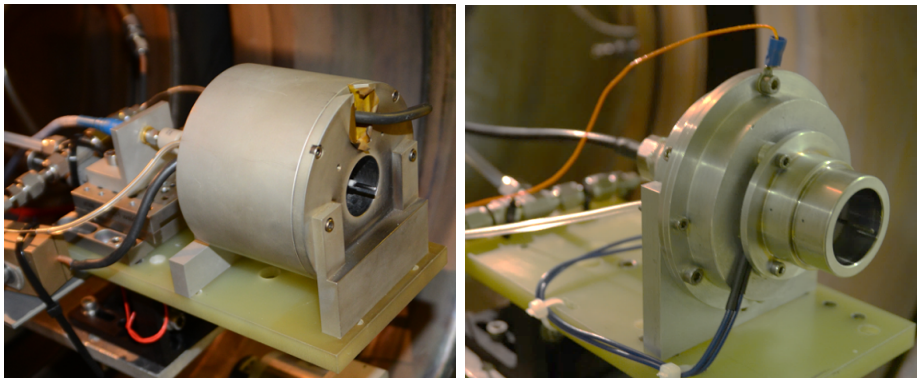

Figure 1.4: Photographs of the two versions of ONERA's ECR thruster investigated in this Thesis. The left photograph corresponds to the solenoids version and the right one to the permanent magnets.

- 36 months at *Universidad Carlos III* (UC3M), Leganés, Madrid, Spain. Starting from the model formulated by Martínez Sánchez *et al.* in Ref. [83], this Thesis has extended their contribution in several directions: a detailed analysis of the kinetic features involved in a MN expansion has been addressed, as well as the effect of expanding distribution functions far from Maxwellian. The main motivation of this research relies in the fact that in MN thrusters,

the plasma properties at the plasma source can vary significantly from one thruster to another, and understanding how this "boundary condition" influences the expansion dynamics is becoming crucial to develop accurate predictable models. All the results of the experimental investigations at ONERA have been compared with the developed theory.

Considering the above, the goals of this Thesis can be broken down into the following:

1. Characterize the main plasma properties (density, electron temperature, plasma potential, ion velocity) along the MN of ONERA's ECR thruster at different operating conditions (mass flow rate and power).

2. Develop new diagnostics capable of measuring separately the perpendicular component to the magnetic field lines of the plasma pressure inside the thruster and along the MN.

3. Evaluate the fluid macroscopic equations of a paraxial MN with the solution from the kinetic model. The objective is to analyze the collective effect of the kinetic features (magnetic mirroring and plasma potential) in the MN expansion, and assess the relevance of collisionless heat fluxes.

4. Obtain parametric scaling laws of relevant plasma properties downstream, which are important to perform a quick estimate of the MN performance without solving the entire model.

5. Address the main differences in the plasma response when expanding "cold" or "hot" ions with respect to electrons in a MN, as well as formulating the distribution function as Maxwellian or mono-energetic.

6. Analyse the kinetic effects of expanding a three species plasma with fast and thermal electrons in terms of the total plasma acceleration, collisionless electron cooling and contribution of the different electron (sub)populations to the total momentum and energy.

7. Study the expansion dynamics of a cold plasma with an anisotropic electron distribution function at the upstream source.

8. Formulate a quasi-1D model based on the research carried out at UC3M adapted to the ECR thruster MN, and compare it with the experimental results obtained at ONERA.

1.4 Thesis structure

The rest of the Chapters of this Thesis are organized as follows.

- Chapter 2 details the development, calibration and testing of a diamagnetic loop to measure the plasma-induced field of the ECR thruster. The measurements are then related to the perpendicular plasma pressure by means of two plasma beam models (1D and 2D). This Chapter constitutes a transcription of the contents published in the peer-reviewed journal *Physics of Plasmas*, entitled "Characterization of diamagnetism inside an ECR thruster with a diamagnetic loop", by S. Correyero, M. Merino, Paul-Quentin Elias, J. Jarrige, D.Packan and E. Ahedo [43].

- Chapter 3 contains the experimental characterization of the main plasma properties along the MN of ONERA's ECR thruster, for different mass flow rates. For this purpose, electrostatic probes and a LIF set-up have been installed for the two versions of the ECR thruster. Results are compared with a supersonic collisionless fluid-kinetic 1D model. This Chapter constitutes a transcription of the contents published in the peer-reviewed journal *Plasma Sources Science and Technology*, entitled "Plasma beam characterization along the magnetic nozzle of an ECR thruster", by S. Correyero, J. Jarrige, D.Packan and E. Ahedo [42]

- Chapter 4 presents a kinetic study of the plasma expansion in a MN, which aims to complete the work of Ref. [83] in several directions. It analyzes the equivalent fluid model, derives parametric scaling laws for downstream plasma properties and analyzes the collective magnetic mirror effect and its relation with temperature anisotropy. This Chapter constitutes a transcription of the contents published in the peer-reviewed journal *Plasma Sources Science and Technology*, under the title "Macroscopic and parametric study of a kinetic plasma expansion in a paraxial magnetic nozzle" by E. Ahedo, S. Correyero, J. Navarro-Cavallé and M. Merino [6].

- Chapter 5 extends the kinetic model to consider a three species plasma expansion (hot and cold electrons). The formation of a quasi-neutral steepened layer is shown, and a parametric study of the total potential drop is presented. The thermodynamics of the two electron species are studied separately, showing the different contribution to the macroscopic fluid moments.

- Chapter 6 studies the plasma response in a MN when the upstream electron distribution function is anisotropic. Two models are implemented; a fully kinetic convergent-divergent model and a hybrid divergent model with fluid ions and kinetic electrons. Results are discussed in terms of the main plasma properties, the evolution of the distribution functions and the contribution to the momentum equation.

- Chapter 7 gathers the main conclusions and contributions of this Thesis, and suggests future lines of research.

CHAPTER

TWO

Characterization of diamagnetism inside an ECR thruster with a diamagnetic loop

This Chapter is a transcription of the paper published in the peer-reviewed journal Physics of Plasmas, by S. Correyero, M. Merino, Paul-Quentin Elias, J. Jarrige, D.Packan and E. Ahedo [43]. The style has been adapted to the layout of this Thesis.

Abstract

The plasma-induced magnetic field in an electron cyclotron resonance plasma thruster is measured non-intrusively by means of a diamagnetic loop that encloses the plasma flow. The calibration process is described, and parasitic currents in the thruster walls and plasma oscillations are identified as the dominant sources of uncertainty. The integrated magnetic flux is seen to depend on the applied power, and less significantly on the mass flow rate. The effect of the diamagnetic loop radius is also studied, by testing two loops of different diameter. To estimate the perpendicular electron pressure in the plasma from the loop measurements, two plasma beam models, 1D and 2D, are used. While both models give similar results for the small loop, they differ significantly for the large loop, showing the relevance of 2D effects when a large diamagnetic loop is used.

2.1 Introduction

Electrodeless plasma thrusters, such as the electron cyclotron resonance thruster (ECRT) [56, 96, 114, 21, 68] and the helicon plasma thruster (HPT) [32, 102, 97], produce a cold-ion, hot-electron plasma by applying electromagnetic radiation to ionize and heat the propellant. An externally-applied magnetic field $\boldsymbol{B}_a$ confines the plasma away from the lateral walls of the thruster chamber, and enables the propagation of the electromagnetic radiation into the plasma, where it is absorbed. Outside of the thruster, $\boldsymbol{B}_a$ diverges to form a magnetic nozzle (MN), where the plasma is expanded and accelerated quasineutrally by Lorentz forces [9, 93]. In the typical operation regime, electrons are well magnetized in the MN and follow the magnetic lines, whereas ions are in general, weakly magnetized. As the electrons expand downstream, an ambipolar electric field $\boldsymbol{E}$ arises in the plasma that confines most electrons and accelerates ions, converting the electron thermal energy into directed kinetic ion energy, and thus creating a supersonic plasma jet channeled by the nozzle. Only the most energetic electrons overcome the potential barrier to create a globally-current-free plasma plume. Finally, the plasma detaches from the closed lines of the applied field to form a free plasma plume [89].

Thrust can be decomposed into pressure thrust and magnetic thrust. The former is due to the plasma pressure on the chamber walls, and is considered an inefficient thrusting mechanism due to the recombination losses it entails. The latter is the reaction to the magnetic acceleration of the expanding plasma, which takes place mainly in the MN region. Positive magnetic thrust requires the plasma to be diamagnetic, so that the magnetic force between the plasma and the magnets or coils of the thruster is repulsive: microscopically, the cyclotron motion of each individual magnetized electron creates a diamagnetic field that opposes the applied one, and experiences a force that pushes it in the downstream direction due to the magnetic mirror effect. Macroscopically, the sum of all electron gyrations and drifts, gives rise to an azimuthal diamagnetic electron current density $j_{\theta e}$ that interacts with $\boldsymbol{B}_a$ to create an inward-confining Lorentz force that balances the outward-expanding perpendicular electron pressure $p_{\perp e}$. In the divergent MN, part of this Lorentz force density ($j_{\theta e} B_r$) acts in the axial direction. The reaction to this force is the largest contribution to magnetic thrust, since the ion azimuthal current $j_{\theta i}$ (which can incidentally be paramagnetic and hence generate magnetic drag) is small in the

cases of interest [9]. The azimuthal electron current $j_{\theta e}$ is also the main contributor to the plasma-induced magnetic field $\boldsymbol{B}_p$, that opposes $\boldsymbol{B}_a$, tends to demagnetize the plasma in the MN, and increases the divergence of the MN [91].

Magnetic thrust scales with the perpendicular electron pressure $p_{\perp e}$ at the source, and it is thus desirable to maximize its value during plasma production. In particular, ECRTs use microwaves that resonate with the electron cyclotron frequency in certain regions of the device, depositing most of the electromagnetic power into the electron perpendicular motion at resonance and resulting in a partially anisotropic electron distribution function, depending on the collisionality of the plasma [55]. Hence, a larger magnetic-to-pressure thrust ratio is expected in these thrusters. Indeed, while isotropic electron populations give rise to about 50% of the total thrust being generated at the MN [9], preliminary measurements with an ECRT prototype show that this fraction can be as large as 80% [130]. This makes the MN of the ECRT an even more essential component for the operation of the thruster.

As $\boldsymbol{B}_p$ is generated by $j_{\theta e}$, measuring $\boldsymbol{B}_p$ allows estimating $p_{\perp e}$, which can provide important information about the operation and performance of these thrusters, and eventually on the magnetic contribution to the thrust. A well-established diagnostic technique to measure $\boldsymbol{B}_p$ is the diamagnetic loop, which consists of a coil of several turns wound around the plasma jet. Its working principle is simple, and relies on the measurement of the induced voltage caused by a change of the magnetic flux enclosed by the loop [63]: obeying Faraday's law, the voltage at the loop ends can be time-integrated during the thruster shutdown transient to obtain the total plasma-induced magnetic flux $\boldsymbol{B}_p$ across the loop that exists just before plasma extinction. The integrated voltage signal is proportional to the number of turns of the loop, which must be chosen according to the sensitivity of the acquisition system.

In the 1960's, the diamagnetic loop was used in magnetic-confinement fusion community to quantify the perpendicular plasma pressure in a reactor [61, 129, 134]. In the field of electric propulsion, Sercel's first attempted to use a diamagnetic loop in the 1990's to estimate the plasma pressure inside an ECRT, but his efforts at that time led to inconclusive results [113], allegedly due to significant systematic errors in the measurements. More recently, Ando *et al.* measured the change in $\boldsymbol{B}_p$ and the plasma thermal energy in a magneto-plasma-dynamic thruster when switching

on an additional ion cyclotron heating stage [14]. Regarding Hall Effect Thrusters, diamagnetic loops have been used to measure the azimuthal drift current in the channel discharge by fast current interruption techniques [128, 105]. Besides these noteworthy works and to the best knowledge of the authors, large diamagnetic loops that embrace the plasma flow have barely been applied in electric propulsion research. More commonly, the plasma-induced magnetic field $\boldsymbol{B}_p$ in plasma thrusters has been measured locally using intrusive Hall probes and B-dot probes into the plasma plume [127, 109].

In other fields of plasma physics, diamagnetic loops have been used to investigate the plasma-induced magnetic field in various plasma devices. Stenzel and Urrutia studied MHD turbulence in a high-β, dense plasma discharge and the expulsion of the magnetic field using a diamagnetic loop and a 3D magnetic probe [117]. Corr and Boswell investigated diamagnetism in a helicon source discharge by placing diamagnetic loops around the channel and the plasma core [41]. As a last example, Noland *et al.* employ a diamagnetic loop on an electron-cyclotron resonance ion source to measure $\boldsymbol{B}_p$, and then use a 1D MHD model to estimate the mean plasma pressure [99].

The present work presents a parametric investigation of the operation of an ECRT prototype developed at ONERA, France, using diamagnetic loop measurements with two loops of different diameter placed around the plasma jet. The integrated induced magnetic flux is then used to evaluate the perpendicular electron pressure inside the plasma jet, and, finally, the influence of 2D effects, specially on the measurements of the loop with larger diameter, is pointed out.

The rest of this article is structured as follows. The experimental set-up is explained in Section 2.2. The calibration of the diamagnetic loops is detailed in Section 2.3. Section 2.4 presents the experimental results of the induced magnetic flux at various thruster power levels and mass flow rates. Section 2.5 estimates the perpendicular electron pressure from the induced magnetic flux measurements with two models: a simple analytic 1D model which considers an infinite uniform magnetized plasma column in equilibrium and a 2D MN model developed by Ahedo and Merino [9]. The 2D effects on the measurements are also discussed there. The main conclusions of this work are gathered in Section 2.6.

2.2 Experimental set-up

2.2.1 ECRT prototype

The thruster prototype consists of a coaxial structure composed of an inner stainless-steel rod (0.9 mm radius) surrounded by a 15 mm long and 13.5 mm radius cylinder, into which 2.45 GHz electromagnetic waves propagate. The back plate of the thruster is a cylindrical piece of 3 mm length made of boron nitride while the lateral thruster walls are made of graphite. A Neodymium permanent magnet creates a static magnetic field in such a way that electrons reach the cyclotron resonance condition (at 875 Gauss for 2.45 GHz) inside the source. The magnetic field generated by the magnet is also responsible for the fully-divergent magnetic nozzle topology (see Figure 2.1), simplifying its design and construction. Finally, the propellant (xenon in the present case) is injected through two symmetrical holes of 1 mm diameter at the back plate.

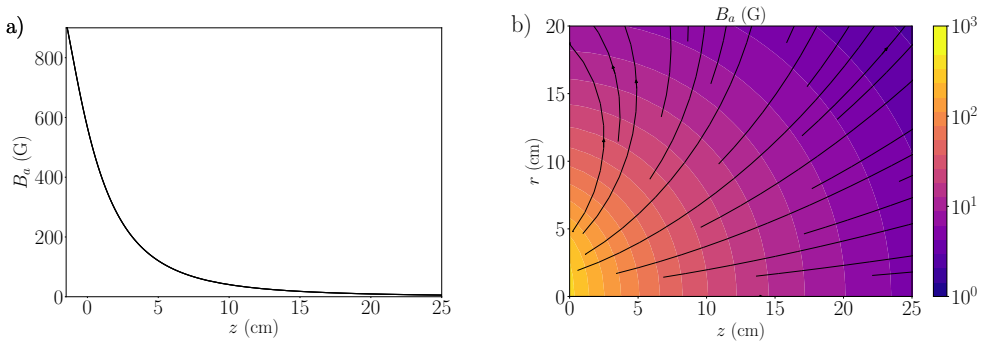

Figure 2.1: (*a*) Magnitude of the applied magnetic field $\boldsymbol{B}_a$ at thruster axis ($z = 0$ corresponds to exit plane); (*b*) 2D magnetic field topology.

2.2.2 Electronics and vacuum facility

Microwave power at 2.45 GHz is transmitted to the thruster from a solid-state amplifier from Kuhne Electronics (100 W maximum power) through a 50 Ω coaxial line, whose losses have been characterized using a vector network analyzer. The output of the generator is connected to a circulator, which allows to dissipate the reflected power in a 50 Ω load. Before entering the vacuum chamber, a bi-directional coupler measures the forward and reflected power through two calibrated diodes,

whose values are registered through a 1 GHz Oscilloscope. The uncertainty of the power measurement is ±1 W.

The tests carried out in this work have been performed at ONERA facilities, located in Palaiseau (France). The vacuum chamber consists of a cylindrical vessel of 2 m length and 0.8 m diameter. Three turbomolecular pumps and one cryogenic pump constitute the pumping system which has a total pumping speed of 13000 l/s of Xenon and can reach a background pressure of 10^{-7} mbar. The background chamber pressure while operating at 2 sccm of xenon was $3.7 \cdot 10^{-6}$ mbar.

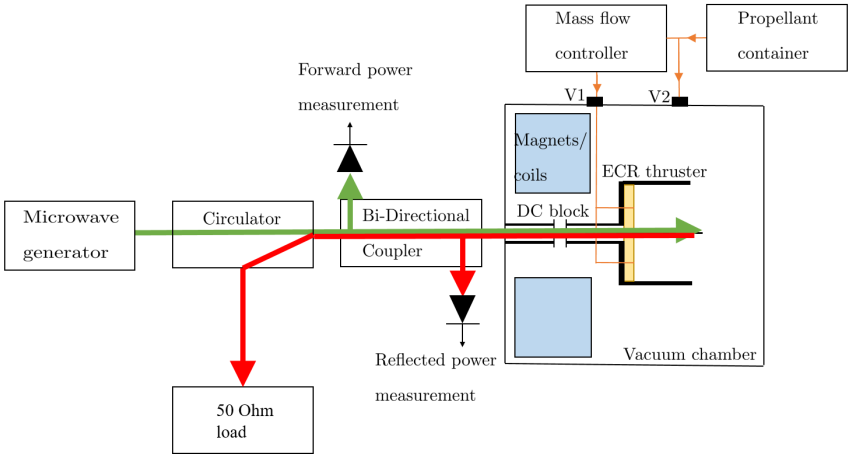

Figure 2.2: Schematic of microwave power line and subsystems in the vacuum set-up.

A direct-current blocker is installed between the power line and the thruster to ensure it is electrically isolated. The thruster floating potential while operating is monitored by means of a multimeter. Figure 2.2 shows a schematic of the vacuum set-up and power line.

2.2.3 Diamagnetic loops

To measure the diamagnetic signal inside the ECR thruster, two diamagnetic loops of different sizes were built:

1. Loop A: $D_A = 3$ cm diameter, $L_A = 1.5$ cm length, $N_A = 30$ turns.

2. Loop B: $D_B = 30$ cm diameter, $L_B = 3$ cm length, $N_B = 12$ turns.

Both loops are made of insulated copper wire. A 1 mm Teflon layer separates Loop A from the thruster walls, while Loop B is positioned with a plastic holder. The diamagnetic loops are fixed in the set-up, and installed coaxially with the thruster walls. Loop A is wrapped exactly around the thruster walls while the half length of Loop B coincides with the thruster exit plane. Figure Figure 2.3 shows an schematic of the position of the loops.

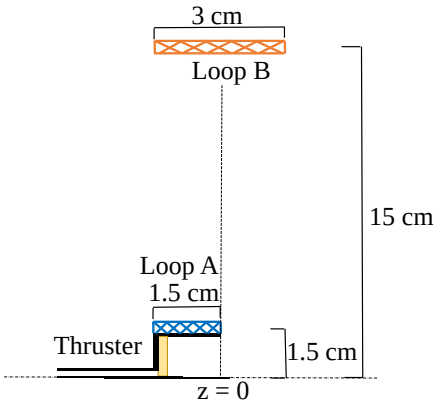

Figure 2.3: Axisymmetric schematic of the thruster and the diamagnetic loops.

The diamagnetic time signal of each loop is measured by a 1 GHz oscilloscope during the transient shut-down of the plasma, starting from a steady-state operation point. Then, the time integration of the Faraday law for the magnetic induction yields:

$$\int_0^t V dt = -N_L \cdot \Phi_p \tag{2.1}$$

where V is the potential difference between the loop terminals, N_L is the number of turns of the loop and Φ_p is the variation of magnetic flux enclosed by the loop before and after the shutdown. Since the applied magnetic field is generated by a permanent magnet, the magnetic flux measured by the loop corresponds only to the induced plasma magnetic field.

2.3 Diamagnetic signal calibration

Identifying potential sources of error in the measurement of the voltage signal at the loop terminals is essential to guarantee a valid computation of the plasma-induced magnetic flux. Particularly important are the eddy currents through the thruster

walls, since a cylindrical conductive material is enclosed by the diamagnetic loop. Other effects as the thruster potential drop during the shutdown, or possible parasite currents from all the electronic systems involved have also been characterized. This section analyzes these effects in the experiment.

2.3.1 Effect of eddy currents

During thruster shutdown, and as the total magnetic flux varies, eddy currents are induced in the conductive parts of the device. In particular, moderate eddy currents can appear in the conductive walls of the thruster. These eddy currents create a magnetic field that opposes the field variation (Lenz's law), and therefore they affect the flux variation measured by the loop. While the overall time integral of equation (2.1) is not modified once the eddy currents die away due to the resistivity of the material, this phenomenon weakens the signal to be integrated (it could even remain below the sensitivity of the acquisition system) and increases its decay time. Consequently, it could make the detection of the signal unaffordable.

To evaluate the influence of this effect, a characterization solenoid (length L_c = 200 mm, number of turns $N_c = 89$, radius $R_c = 10$ mm) was built to emulate the voltage drop that is recorded by the diamagnetic loop when the thruster is powered off. This set-up allows to study the eddy currents phenomena for a known input magnetic field and in ambient conditions [23]. The solenoid was placed coaxially with the thruster walls and the diamagnetic loop (See Figure 2.4).

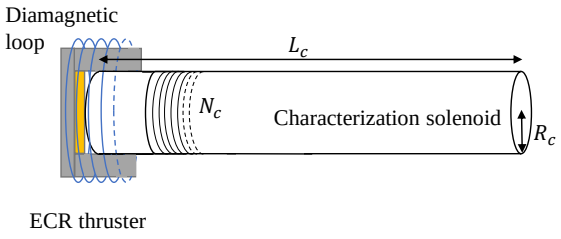

Figure 2.4: Schematic of the characterization solenoid placed coaxially with the diamagnetic Loop A and the thruster walls

By generating a pulsed current signal on the solenoid, the induced voltage in

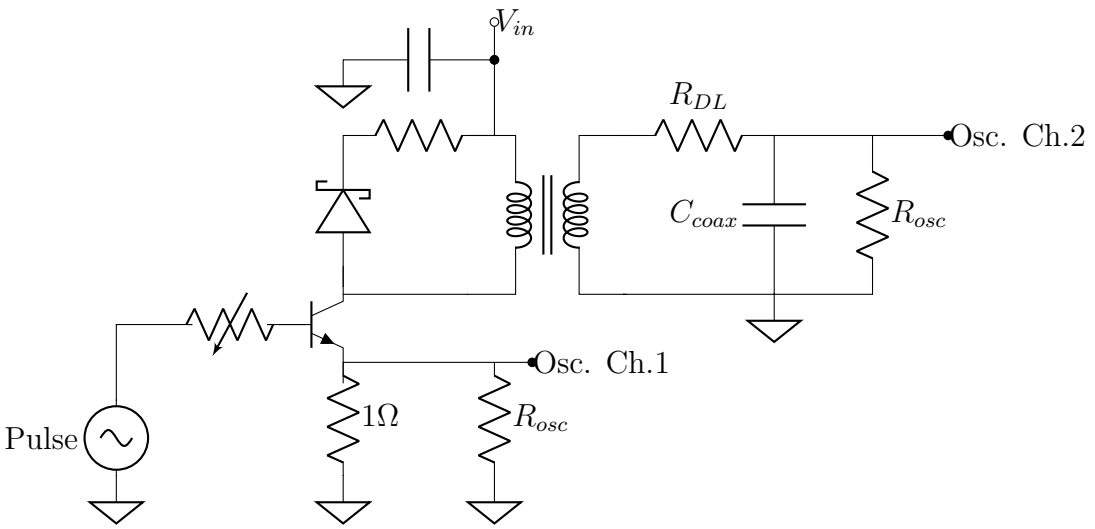

Figure 2.5: Characterization solenoid circuit coupled with the diamagnetic loop circuit. R_{osc} is the scope input impedance set on 50 Ω, C_{coax} is the parallel capacitance mainly due to the coaxial cables, R_{DL} is the diamagnetic loop series resistance. The parallel capacitance can be estimated based on the capacitance of a RG-58 (BNC 50 Ω) cable, which in this case is around 300 pF. The diamagnetic loop circuit inductance has been estimated to be 50 μH and 80 μH for loops A and B respectively.

the diamagnetic loop was recorded. The current amplitude was controlled so that the response was comparable to the expected plasma diamagnetism. Figure 2.5 represents the electric circuit that was built to pulse the coil at specific values of current together with the diamagnetic loop circuit schematic. The loop and cables resistance R_{DL} is negligible compared to the scope impedance. To illustrate the measurement characteristics of the system, the gain magnitude frequency response of loop A is plotted in Figure 2.6 together with the input current impulse from the characterization solenoid. Notice that the system behaves as a low-pass filter with a power roll-off of 20dB/dec at high frequencies, being the cut-off at 150 kHz (shown as a vertical dashed line in Figure 2.6). For verification, the circuit has been simulated with the software *LTspice* to study the system response.

Two different materials were used to evaluate the effect of eddy currents in the thruster walls: graphite (the actual material of the present ECRT prototype walls) and aluminum. As can be observed in Figure 2.7, the voltage integral could not be fully recovered in the case of aluminum walls due to the large time response of the eddy currents and the low value of the resulting diamagnetic signal. On the contrary,

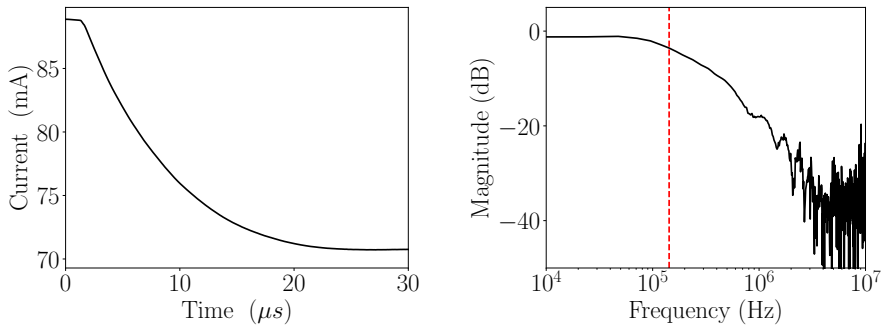

Figure 2.6: Output signal from characterization solenoid (left) and the gain magnitude frequency response of the small diamagnetic loop (right), where the red dashed vertical line represents the cut-off frequency (-3 dB).

the lower conductivity of graphite resulted in a diamagnetic signal, comparable to the absence of conducting walls. The time integral of each curve corresponds to $7.53 \cdot 10^{-8}$ V·s without thruster walls (and thus without eddy currents), $7.45 \cdot 10^{-8}$ V·s for graphite walls, and $9.48 \cdot 10^{-9}$ V · s for aluminum walls. With graphite walls, only a relative error of 1.1% on the total integral is committed, which is deemed acceptable for the present measurements. On the contrary, aluminum walls result in an error around 87%. It should be noted that integrating over a larger time in this case does not improve significantly the result, since the background noise is above the signal itself after the initial instants.

Concerning eddy currents in the vacuum chamber walls, although the same phenomenon could in principle take place, no measurable effect was found. The calibration process was performed inside and outside the vacuum chamber to check the influence in the diamagnetic loop signal. In the case of “no thruster walls", the characterization solenoid was also used to compare the estimated magnetic flux and the real measured flux by the diamagnetic loop, finding a very good agreement between the theoretical and experimental values in the desired range, avoiding the need for a correction factor.

2.3.2 Plasma oscillations

To better understand the nature of the diamagnetic signal, a specific test was carried out to relate the plasma extinction process and the decay of the diamagnetic field.

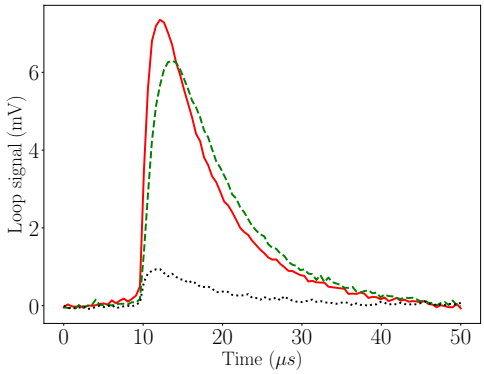

Figure 2.7: Signal of the diamagnetic Loop A with the characterization solenoid. Three different cases are represented: aluminum thruster walls (·····), graphite thruster walls (- - -) and no thruster (———).

Together with the diamagnetic signal, three different measurements were taken simultaneously: firstly, the microwave forward power entering the thruster line was read by means of a calibrated diode connected to a directional coupler; secondly, the thruster floating potential was directly measured by a voltage probe connected to the thruster walls; and lastly, the light intensity coming from the plasma source was collected into an optic fiber and recorded by photodiode.

Figure 2.8 (left) shows the normalized voltage at the diamagnetic loop and the three additional measurements, starting from operation at 30 W power and 3 sccm Xenon. The simultaneity of the four signals illustrates the magnetic flux change at diamagnetic loop during the shutdown. Visibly, the three additional measurements are stable before shutdown. In contrast, the diamagnetic loop signal displays large oscillations, which could be possibly attributed to plasma instabilities during operation. These oscillations are an important source of error in the time integration of equation (2.1), generating uncertainty in the measurement of the magnetic flux change at shutdown. These oscillations have been characterized and used to define the error bars in the plots of next sections. Their frequency and amplitude are operation point-dependent, but in most cases under study, peaks between 2 kHz and 150 kHz were identified. Incidentally, these oscillations are in the same frequency range as the ones found by Sercel in [113].

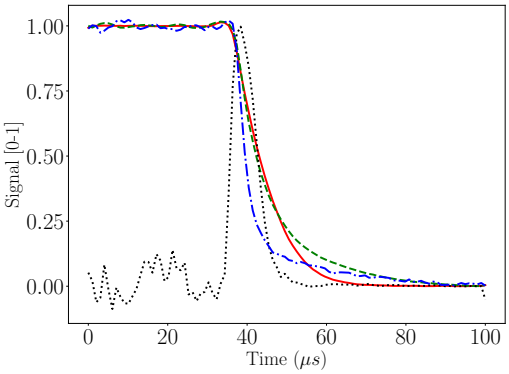

Figure 2.8: Signal of diamagnetic Loop A (·····), thruster floating potential (- - -), forward power (———) and light intensity coming from the plasma source (-·-·-) during thruster shutdown, normalized.

2.3.3 Other effects

Lastly, the effect of the thruster potential decay on the diamagnetic loop signal during the shutdown was evaluated. Microwave power is transmitted to the plasma by a 50 Ω coaxial line, and a Direct Current Blocker (DC Block) is placed between the line and the source cavity to isolate the generator and components from the plasma. Therefore, the conductive thruster walls can float and they reach high electric potentials (around 100–200 V) when the thruster is operating. This floating potential is maintained by the plasma and depends directly on the plasma properties (ion and electron fluxes, sheath between thruster and plasma, etc) and the thruster materials. At the thruster shutdown, the floating potential drops to a residual value as shown in Figure 2.8. To study any possible influence of this electrostatic effect on the diamagnetic signal, the thruster was charged externally in the absence of plasma to 50 V and discharged rapidly simulating the thruster shutdown. The signal of the loop was recorded simultaneously with the thruster potential. The observed effect was negligible when compared with the total signal from the diamagnetic loop.

2.4 Plasma-induced magnetic flux

The next subsections report on the experimental measurements with the diamagnetic loops. In a first set-up, only Loop A was installed, and a parametric analysis

on the power and xenon mass flow rate of the thruster was carried out. In a second set-up, both loops A and B were used simultaneously to assess the effect of the loop diameter on the measurements.

2.4.1 Variation with power and mass flow rate

The thruster shutdown transient lasts around 15 µs, the time span in which the main induced voltage of the loop is observed. Figure 2.9 illustrates the signal at the diamagnetic Loop A at three different powers at equal mass flow rate (left), and at three different mass flow rates at equal absorbed power (right). The plasma-induced magnetic flux Φ_p obtained by integrating the diamagnetic signal with equation (2.1) is shown in Figure 2.10, where the data represent the averaged values between two independent samples. The repeatability of the measurements is affected by the erosion of the antenna and particle depositions at the back-plate, which are not negligible within a few hours of operation. Regarding the error bars, the difference between repeated measurements is added to the uncertainty in the signal integration procedure, which is computed as the ratio between the amplitude of the loop signal oscillations before the shutdown and the maximum amplitude registered after the shutdown. Notice that this source of uncertainty is specific of each operation point.

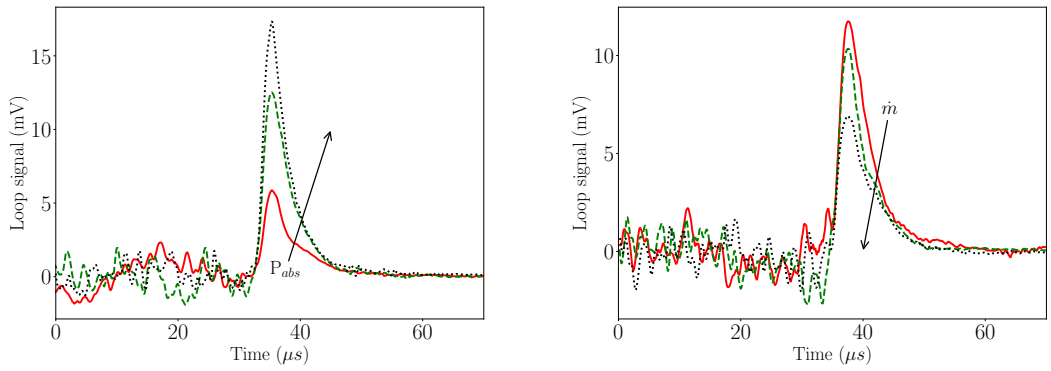

Figure 2.9: Diamagnetic signal (in mV) versus time during the thruster shutdown for: (left) 2 sccm of Xenon and different power levels: 15 W (———), 30 W (- - -), and 41 W (·····), and (right) 30 W at three different xenon mass flow rates: 1 (———), 2 (- - -), and 3 sccm (·····).

As it can be observed, the measured induced magnetic flux increases with mi-

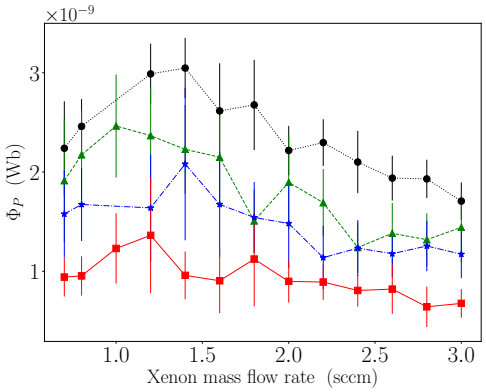

Figure 2.10: Induced magnetic flux measured in Loop A as a function of the mass flow rate, for different power levels: 15 W (——), 25 W (-·-·-), 30 W (- - -) and 41 W (·····).

crowave power. Moreover, for each tested power, a slightly higher value was found for a mass flow rate between 1 and 1.5 sccm. Beyond this value the induced flux decreases when increasing the mass flow rate. It should be noted, however, that the variation of Φ_p with $\dot{m}$ is small, and for the lower power values, it falls within the uncertainty of the measurements.

The behavior of Φ_p with power and mass flow rate is consistent with the measurements performed by Vialis *et al.* of the magnetic thrust in the same ECRT prototype (figure 6 top of [130], the measurements of direct thrust on the magnet) . This correlation supports a direct relation between the magnitude of the induced magnetic flux, as measured by the diamagnetic loop, and the magnetic thrust.

2.4.2 Influence of the diamagnetic loop size

To assess the influence of the diamagnetic loop radius, the signals at the two loops A and B were measured simultaneously. Any differences between the measurements can be attributed to each loop capturing a different plasma-induced magnetic flux Φ_p, which in turn means the existence of $\boldsymbol{B}_p$ outside of the plasma beam. Contrary to the case of an infinite plasma column, where $\boldsymbol{B}_p$ is restricted to the inside of the plasma itself, the 2D plasma expansion in the MN is expected to generate fields that leak outside of the plasma jet [91]. As such, operating two loops of different radii enables the characterization of this phenomenon.

The first column of Tab. 2.1 displays the measured Φ_p for two different mass flow

rates (1 and 2 sccm Xe) and 30 W power. In each case, the plasma-induced magnetic flux measured by Loop B is roughly one order of magnitude larger than that of Loop A. This difference indicates that $\boldsymbol{B}_p$ extends indeed outside of the plasma jet and that the 2D character of the expansion and the azimuthal electron currents must be taken into account to fully characterize the plasma-induced magnetic field, the operation of the device, and the generation of magnetic thrust. To explain the differences encountered by the two loops, and to relate the measurements of Φ_p to the perpendicular electron pressure, two models are proposed in the next section; a 1D plasma column model, and a 2D fluid model available in the research group [9].

Finally, it is noted that the differences in Φ_p in Tab. 2.1 between the two mass flow rates are within the uncertainty of the measurement (see also Figure 2.10), and thus no conclusions can be drawn from these results in what regards the variation of these effects with the mass flow rate.

2.5 Mean perpendicular electron pressure

To relate the loop magnetic flux measurements to the plasma properties it is necessary to consider a plasma model and the magnetic field it induces during thruster steady-state operation. To identify the dominant mechanisms that drive the plasma-induced magnetic flux through the loop and estimate the perpendicular electron pressure in the plasma, a simple analytic 1D model, similar to the one used in [99], is presented first. Then, a 2D model of the plasma expansion in the magnetic nozzle is used to discuss the influence of the 2D plasma distribution on the measurements by the two loops.

2.5.1 Infinite plasma column model

Consider an axially-uniform ($\partial/\partial z = 0$), infinite, collisionless plasma column of radius R_p. The plasma is confined by a uniform, axially applied magnetic field B_{za}, and the radial electric field in the plasma is assumed negligible. Electron mass is neglected with respect to ion mass, ions are assumed cold, and electrons can have different perpendicular and parallel pressures, $p_{\perp e}$ and $p_{\parallel e}$. Under these assumptions the radial electron momentum balance reduces to:

$$0 = -\frac{\partial p_{\perp e}}{\partial r} + j_{\theta e} B_{za} \tag{2.2}$$

where $j_{\theta e} = -enu_{\theta e}$ is the azimuthal electron current density, which is the dominant contribution to the total plasma currents [9, 91]. Accordingly, the azimuthal component of Ampère's equation $\nabla \times \boldsymbol{B}_p = \mu_0 \boldsymbol{j}$ for the axial plasma-induced magnetic field B_{zp} reads

$$-\frac{\partial B_{zp}}{\partial r} = \mu_0 j_\theta \simeq \mu_0 j_{\theta e} \tag{2.3}$$

Note that the radial component of the plasma-induced magnetic field, B_{rp}, is identically zero in this infinite plasma column configuration. Combining equation (2.2) and equation (2.3) and integrating, noting that both $p_{\perp e}$ and B_{zp} are zero outside of the plasma, yields an expression for B_{zp},

$$B_{zp}(r) = -\frac{\mu_0}{B_{za}} \int_r^{R_P} \frac{\partial p_{\perp e}}{\partial r} dr = -\frac{\mu_0}{B_{za}} p_{\perp e}(r) \tag{2.4}$$

The induced field is diamagnetic and opposes the applied one. The ratio of induced-to-applied magnetic field at the origin coincides with the plasma beta there:

$$\left| \frac{B_{zp}(0)}{B_{za}(0)} \right| = \frac{\mu_0 p_{\perp e}(0)}{B_{za}^2(0)} = \beta_0 \tag{2.5}$$

Integrating again equation (2.4) yields the induced magnetic flux measured by a loop with radius R_L located around the plasma column upon plasma shutdown,

$$\Phi_p = -\frac{\mu_0}{B_{za}} \int_0^{R_L} 2\pi p_{\perp e} r dr = -\frac{\mu_0}{B_{za}} \pi R_P^2 \bar{p}_{\perp e} \tag{2.6}$$

where $\bar{p}_{\perp e}$ is the cross-section mean of the perpendicular electron pressure in the plasma column. Two observations can be made. First, the induced magnetic flux scales with $\bar{p}_{\perp e}$, and it is weaker the larger the applied magnetic field is. Second, the radius R_L of the measuring loop is irrelevant as long as $R_L > R_P$, which indeed means that any induced field in the region between R_P and R_L is ignored.

Equation (2.6) has been used to compute the mean perpendicular electron pressure $\bar{p}_{\perp e}$ at the exit section of the thruster shown in the second column of Tab. 2.1. It is evident that the estimates of $\bar{p}_{\perp e}$ from the smaller Loop A and the larger Loop B are very different. This difference arises from the inadequacy of the 1D model to describe the present situation, where the plasma expands radially at a large angle in the MN region. Expectedly, the error of the 1D model increases with the radius of the diamagnetic loop used, as the contribution of the induced magnetic field lying between the loop and the plasma beam is more important.

As a cross-comparison with the data available in the literature, notice that the estimated perpendicular electron pressure presented in Tab. 2.1 is within the expected range. The direct measured thrust in this device has been reported to be hundreds of μN (both on the plasma source and on the permanent magnet) [131]. It is expected that the magnetic thrust is proportional to the perpendicular plasma pressure times an "effective" area. By taking the backplate of the thruster as a reference area, 5.73 $\cdot 10^{-4}$ m^2, a plasma pressure of hundreds of mPa is obtained, which is in line with the results reported here. In parallel, the electron temperature is expected to be various tens of eV (20 eV have been measured in the near plume region [74]) and the mean plasma density inside the thruster has been estimated to be between [1-3]$\cdot 10^{17}$ m^{-3} at 1 and 2.5 xenon sccm, respectively. These values were estimated by performing angular scans of current with a Faraday gridded probe and identifying the mean ion velocity at the exit plane with a simple 1D laser induced fluorescence set-up [45]. With these data, the mean plasma pressure should also be hundreds of mPa.

$\dot{m}$ (sccm)		Measured Φ_P at shutdown (10^{-9} Wb)	Estimated $\bar{p}_{\perp e}$ 1D model (mPa)	Estimated $\bar{p}_{\perp e}$ 2D $n_G(0,r)$ (mPa)	Estimated $\bar{p}_{\perp e}$ 2D $n_P(0,r)$ (mPa)
1 sccm	Loop A	2,46 ± 0,5	182 ± 37	218 ± 44	209 ± 42
	Loop B	10,0 ± 2,2	737 ± 162	99 ± 22	151 ± 33
2 sccm	Loop A	1,89 ± 0,4	140 ± 30	168 ± 36	157 ± 36
	Loop B	13,3 ± 3,4	979 ± 250	229 ± 131	193 ± 48

Table 2.1: Experimental magnetic flux Φ_p from the two loops at 30 W of absorbed power and estimated values of mean perpendicular electron pressure inside the thruster source from the 1D and 2D models (Gaussian and polynomial initial density profiles)

2.5.2 2D plasma model

The simple 1D model from previous section fails to explain the differences in measured flux between the two loops of different radii, and it can only be regarded as a rough estimate of the induced field generated by the plasma of the ECRT. The 2D features of the plasma, such as the finite size of the thruster and the expansion

in the magnetic nozzle need to be taken into account in the model to improve the computation of the radial mean of the perpendicular electron pressure, $\bar{p}_{\perp e}$.

The thruster itself is modeled as an axially-uniform finite column of plasma in equilibrium with an assumed radial profile, from where the azimuthal current density can be readily obtained. The computation of the azimuthal current in the divergent MN is afforded by the 2D model of Ahedo and Merino (DIMAGNO) [9]. The model consists of the fluid equations for hot electrons and single-charged ions, which are integrated with the method of characteristics downstream from the thruster exit plane, where the plasma radial profile coincides with that in the thruster. This model has been used in the past to identify the plasma acceleration and thrust generation mechanisms in the magnetic nozzle, and to explain the plasma-induced magnetic field and the plasma detachment downstream [91, 92, 89]. In addition to the assumptions of the simple model of Section 2.5.1, electrons are treated as a fully-magnetized, isothermal species ($T_e = T_{e0} = \text{const}$), which, while ignoring electron anisotropy, is a reasonable approximation in the near-region of the magnetic nozzle [90]. Ions, on the other hand, are only partially magnetized.

Once $j_{\theta e}$ has been computed in the whole plasma domain, it is interpolated into a regular Cartesian grid and the analytic solution of a thin current loop at each node n of the grid is used to calculate the resulting plasma-induced magnetic field $\boldsymbol{B}_p$:

$$B_{zp} = \sum_n \frac{\mu_0 I_n}{2\pi} \frac{1}{\sqrt{(r+r_n)^2 + (z-z_n)^2}} \left[\mathrm{K}(m_n) - \frac{r^2 - r_n^2 + (z-z_n)^2}{(r-r_n)^2 + (z-z_n)^2} \mathrm{E}(m_n) \right] \tag{2.7}$$

$$B_{rp} = -\sum_n \frac{\mu_0 I_n}{2\pi r} \frac{(z-z_n)}{\sqrt{(r+r_n)^2 + (z-z_n)^2}} \left[\mathrm{K}(m_n) - \frac{r^2 + r_n^2 + (z-z_n)^2}{(r-r_n)^2 + (z-z_n)^2} \mathrm{E}(m_n) \right] \tag{2.8}$$

where $\mathrm{K}(m)$, $\mathrm{E}(m)$ are the complete elliptic integrals of the first and second kind [2], z_n,r_n, and I_n are the axial, radial position, and associated azimuthal current of node n, and

$$m_n = \frac{4 r_n r}{(r+r_n)^2 + (z-z_n)^2}. \tag{2.9}$$

The resulting 2D model of the plasma expansion depends on two dimensionless parameters. First, there is the normalized ion gyrofrequency computed with the applied magnetic field at the origin B_{a0}, $\hat{\Omega}_{i0} = eB_{a0}R_p/\sqrt{m_i T_{e0}}$, which controls the ion magnetization strength and only plays a minor role in the near-field expansion [91]. In the present thruster, with $B_{a0} = 0.0558$ T, xenon as propellant, and an electron temperature in the range 20–30 eV, one has $\hat{\Omega}_{i0} \simeq 0.13$ [74]. Second, there is the plasma beta parameter at the origin, β_0, which is calculated so that the magnetic flux through the diamagnetic loop area matches the experimental measured value. Finally, the model depends on the initial plasma profile at the thruster, which is currently not known. To evaluate the influence of the initial plasma profile on the computation of $\bar{p}_{\perp e}$ from the measurement of Φ_p at the loop, two different profiles (a Gaussian one and a polynomial one) have been simulated to assess the influence of this aspect on the measured magnetic flux. Figure 2.11 shows the plasma pressure p and azimuthal electron current density $j_{\theta e}$ of the two considered initial profiles, normalized with their mean perpendicular electron pressure $\bar{p}_{\perp e}$). The azimuthal current is larger where pressure gradients are larger, and thus varies between the two profiles. The Gaussian profile has larger currents near the axis, whereas in the more radially-uniform polynomial case, $j_{\theta e}$ is negligible except near the plasma edge.

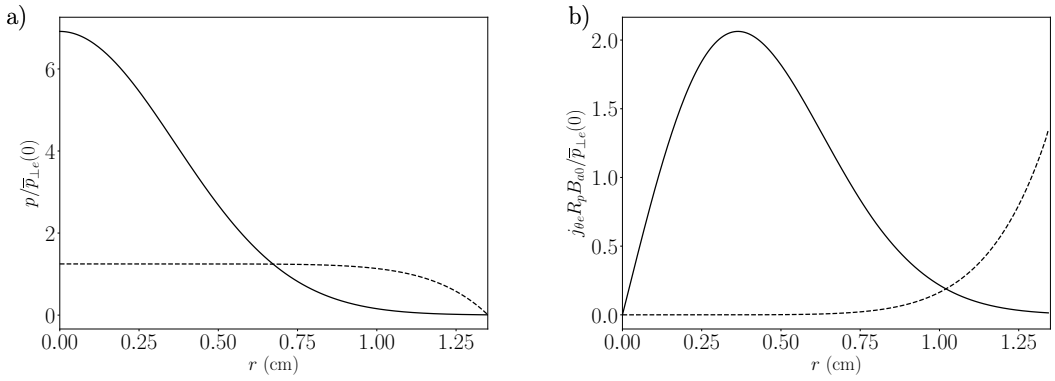

Figure 2.11: (a) Normalized plasma pressure $p/\bar{p}_{\perp e}(0)$ and (b) normalized azimuthal current density $j_{\theta e}R_pB_{a0}/\bar{p}_{\perp e}(0)$ of the two considered initial plasma profiles in the thruster for the Gaussian distribution $n_G\,(0,r) = \exp\left(-3 \cdot \ln\left(10\right) \cdot r^2\right)$ (——) and the polynomial distribution $n_P\,(0,r) = 1 - r^8$ (- - -).

Figure 2.12 shows the 2D maps of the resulting plasma-induced magnetic field

B_p and the developed azimuthal electron currents along the expansion $j_{\theta e}$ that result from the Gaussian and polynomial initial profiles. As the plasma currents downstream from the simulation box have an impact in the domain, the DIMAGNO simulations have been extended down to $z = 60$ cm but results are retained only down to $z = 25$ cm.

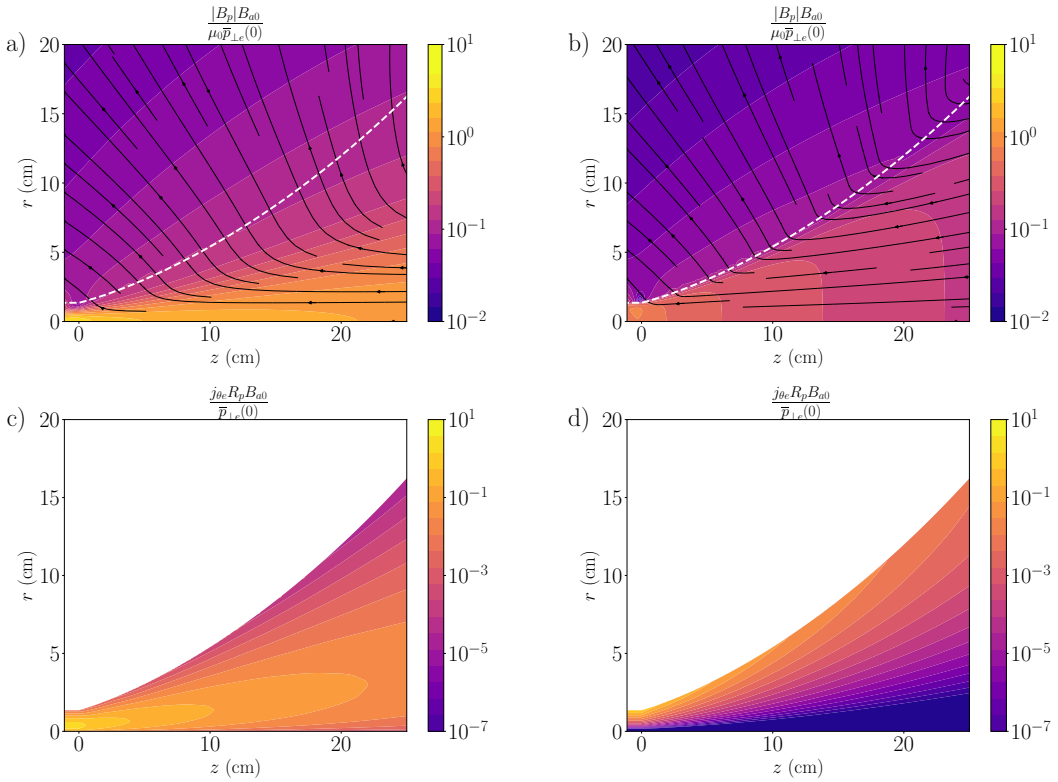

Figure 2.12: Plasma-induced magnetic field and azimuthal electron current density in the near-region plume for the Gaussian (a, c) and polynomial (b, d) initial plasma profiles. The white dashed line represents the plasma boundary.

The computed plasma-induced magnetic field from equation (2.7) and equation (2.8) is integrated and averaged along the measuring loop section and equated to the measured magnetic flux. The resulting expressions allow computing $\bar{p}_{\perp e}$ at the thruster exit plane, which is shown in the last two columns of Tab. 2.1. Comparing these values with those of the 1D model of Section 2.5.1, several remarks can be made. Firstly, the difference in the estimated value of $\bar{p}_{\perp e}$ computed with the two models (irrespective of the initial profile used) is small for the smaller Loop A. This suggests that 2D effects are not essential near the thruster axis, but become

important away from it, and that the 1D model can be used to estimate $\bar{p}_{\perp e}$ when the loop radius is close to the plasma radius. Secondly, it is noted that the 2D model provides a far better agreement between the $\bar{p}_{\perp e}$ estimated with the two loops than the 1D model: while there is a discrepancy larger than the uncertainty in the measurements, it is evident that the 2D model produces values in the same range with each loop, whereas the 1D model fails by one order of magnitude. This indicates that 2D effects are important in the estimation of $\bar{p}_{\perp e}$ when the loop radius is large. Concerning the sensitivity to the initial plasma density profile in the 2D model, data show that it only causes a difference for the larger Loop B, while its effect is negligible for Loop A. While it is not possible to assert with certainty which profile fits better with the real plasma beam, the polynomial profile seems to provide a slightly better agreement between the estimate of $\bar{p}_{\perp e}$ from Loop A and B data than the Gaussian profile. Additional investigation of the radial plasma profile (possibly with other plasma diagnostics) is necessary to confirm this observation.

Finally, the 2D plasma model used here allows to compute the total magnetic thrust by integrating the $j_{e\theta}B_r$ component along the simulation domain. For instance, for the first row of Tab. 2.1 (1 sccm), the computed thrust with Loop A is 251 μN and 207 μN for the Gaussian and polynomial profiles, respectively, while for Loop B is 128 μN and 170 μN. As a reference, the maximum azimuthal current density for the Gaussian profile at 1 sccm is around 4000 A/m^2. The radial magnetic field at this point is 31.4 Gauss. With these values, a magnetic thrust of a few hundreds of μN is estimated. These values of thrust are in the order of the values given in the literature [131] even though the experimental set-up of [131] was different from the one presented here, including different vacuum facilities and losses through the power line.

2.6 Conclusion

Two diamagnetic loops of different radii have been employed to measure non-intrusively the plasma-induced magnetic flux Φ_p at the exit plane of an Electron Cyclotron Plasma Thruster prototype at different power levels and propellant mass flow rates. The proposed set-up has demonstrated to be capable of detecting the plasma-induced magnetic flux by integrating the diamagnetic signal in the loop during thruster shutdown.

The calibration of the diamagnetic loops assessed possible sources of error when applying this technique to an ECRT. In particular, it identified the influence of eddy currents in the thruster walls as a major source of error depending on their material, and it was found that graphite results in a cleaner diamagnetic signal than aluminum, remaining the thruster operation conditions unchanged. Plasma oscillations of the loop signal during steady state operation were seen to be large, and they induce uncertainty in the measurements. Characterizing and understanding the source of these oscillations is interesting by itself and will be the subject of future work.

The diamagnetic flux Φ_p generated by the plasma increases with applied power, and has a weak non-monotonic behavior with the mass flow rate. These trends agree well with those of the recent direct measurements of magnetic thrust by Vialis *et al.* in the same thruster (in a different facility and with different diagnostics). Both the diamagnetic flux Φ_p and the magnetic thrust are directly related to the perpendicular electron pressure in the plasma, which in a thruster with anisotropic heating like the ECRT may differ from the parallel electron pressure.

The magnetic flux measured by the larger loop has been found to be significantly greater than the magnetic flux measured by the smaller one. This attests to the importance of the 2D geometry of the plasma-induced magnetic field, as the magnetic flux created by the plasma spills outside of the plume volume, meaning that a larger loop will capture more flux. Two plasma models, 1D and 2D, have been used to simulate Φ_p and relate its value to the radial mean of the perpendicular electron pressure at the thruster exit plane, $\bar{p}_{\perp e}$, showing that it is within the expected range. Electron pressures up to 200 mPa have been inferred from the diamagnetic loop measurements, which are in line with previous measurements of electron temperature, plasma density and thrust reported in the literature for this thruster [74, 45, 131]. The 1D model only provides valid estimates of $\bar{p}_{\perp e}$ for the loop of smaller radii, and the necessity of a 2D model of the plasma becomes apparent when the larger diamagnetic loop is used. These results point out the limitations of the simple formulas emanating from the 1D model to compute the electron pressure in the plasma.

In order to assess the effect of the radial plasma profile in the thruster in the 2D model, two different ones where tested. The differences observed between the two are small, especially when using the smaller loop, but it does have an impact with

the larger one. Therefore, the smaller loop is a better option for an estimation of the plasma pressure at the source.

Finally, neither model accounts explicitly for the anisotropy of the electron population; future research must advance in this direction, and in general, improve the electron model used, in order to refine the estimates of this work. This may be especially relevant for the ECRT for the reasons stated above.

CHAPTER

THREE

Plasma beam characterization along the magnetic nozzle of an ECR thruster

This Chapter is a transcription of the paper published in the peer-reviewed journal Plasma Sources Science and Technology, by S. Correyero, J. Jarrige, D.Packan and E. Ahedo [42]. The style has been adapted to the layout of this Thesis.

Abstract

Experimental characterization of plasma properties along the magnetic nozzle of an Electron Cyclotron Resonance thruster is presented here. A permanent magnet prototype and a solenoid prototype are tested, whose main difference relies on the magnetic field strength and topology. A cylindrical Langmuir probe is used to measure plasma potential, plasma density and electron temperature. In the permanent magnet thruster set-up, a Laser Induced Fluorescence diagnostics is performed simultaneously with the Langmuir probe to measure the mean ion kinetic energy, and a Faraday gridded probe to characterize the angular plasma beam. An effective electron cooling rate has been identified, as well as the dependence of the total plasma potential drop with the mass flow rate. Results are compared with a supersonic collisionless fluid-kinetic 1D model where electron dynamics account for magnetic mirror effects and potential barriers, while ions are treated as a fluid cold species. The comparison allows to estimate the sonic transition of the plasma flow.

3.1 Introduction

In simple terms, a magnetic nozzle (MN) consists of a divergent magnetic field generated by a a set of solenoids or permanent magnets, whose main function is to confine and accelerate the plasma beam. Interest in MNs has increased significantly during the past years, [132, 33, 124], accelerating the development of the so-called MN plasma thrusters, such as the helicon thruster [102, 20, 33], the Variable Specific Impulse Magnetoplasma Rocket (VASIMR) [48], the applied-field magnetoplasmadynamic thruster [15, 72] or the electron cyclotron resonance (ECR) thruster [112, 68]. Among its numerous advantages over other acceleration systems, noteworthy are its contactless character, which reduces erosion and can extend the thruster lifetime, its versatility which allows to adapt the magnetic field topology in flight or its easy scalability. However, plasma dynamics in a MN involve complex physical mechanisms that are yet not fully understood, and are crucial to determine the thruster performance. Several authors have contributed significantly to the development of this device, providing insightful theoretical and experimental research involving MN expansions, such as plasma detachment [122, 16, 47, 101, 10], formation of ambipolar electric field [9, 80, 17] and magnetic thrust generation [121, 104, 131]. Ideally, modelling and testing must make progress together, since one without the other may fall short under scientific scrutiny.

Experimental characterization of the plasma beam properties along a MN can reveal not only the thruster performance, but also important physical aspects concerning plasma expansion dynamics that are still unclear. For instance, the evolution of the electrons along the divergent magnetic field is still a subject of discussion. Takahashi *et al.* in [125] studied the thermodynamics of a magnetized electron gas expansion, showing the correlation between an external electric field and the polytropic index. Little and Choueiri in [78] characterized the axial variation of macroscopic quantities in a RF plasma beam and investigated the electron cooling phenomena, comparing its results with a fluid 1D model that included electron heat conduction and revealing the critical need for improved 1D models to describe the MN expansion. More recently, experimental studies performed by Kim *et al.* in [69, 70] showed the coexistence of adiabatic expanding electrons and isothermal confined electrons along the MN of an ECR thruster. In this sense, the requirement

for accurate experimental data and validation of advanced theoretical models for MNs is clear.

On the experimental side, ONERA has been developing an ECR thruster during the past years consisting of an ECR coaxial cavity followed by a divergent MN [68]. Multiple research has been done concerning this technology: Vialis *et al.* performed the first direct thrust measurements in [131], an analytical model of the ECR source was developed to identify the most important physical features in the ECR discharge [30], Lafleur *et al.* performed a theoretical and experimental investigation in [74] to determine the relationship between the maximum ion energy and the upstream electron temperature in this device, finding a value of 4-5. In order to contribute to the previous research, and characterize longitudinally the plasma expansion along the center line of the ECR thruster, this work presents the first complete measurements of plasma potential, electron density, electron temperature, and ion velocity along the expansion. Two ECR prototypes are tested, with two different MN topologies. A parametric study of variation of the mass flow rate $\dot{m}$ is presented, which is crucial to understand the expansion dynamics, since the electron temperature and the isotropization of the electron energy distribution function are highly dependent on this parameter. Langmuir probes have been used to characterize the evolution of plasma properties along the axis of the MN, and a Laser Induced Fluorescence (LIF) diagnostics has been employed to determine the mean ion velocity in the thruster exit plane and along the center line of the expansion [67]. Angular scans of the ion current have been performed at different xenon mass flow rates to estimate thruster performances partially.

The fluid-kinetic quasi-1D steady-state model by Martínez-Sánchez, Ahedo and Navarro [83] is here adapted to analyze the experimental data along the MN of the thruster. The model determines self-consistently the axial profile of the ambipolar electric potential and the electron distribution function of a magnetized fully-divergent plasma expansion. Contrary to the commonly used fitted polytropic laws, the model in [83] determines directly the exact solution of the electron velocity distribution function and the total potential drop in the magnetized expansion, which for near-cold ions, only depends on the ion to electron mass ratio.

This paper is organized as follows: Section 3.2 explains the set-up developed at ONERA, Section 3.3 presents the main experimental results, Section 3.4 describes the model used to predict the plasma properties along the expansion and compares

the experimental data with the theoretical model. Finally, Section 3.5 concludes the main results of the research.

3.2 Experimental set-up

3.2.1 The ECR thruster of ONERA

The experiments carried out in this work were performed along the MN of the ECR thruster developed by ONERA [68]. It has an axisymmetric geometry and it is composed of a coaxial plasma source cavity of dimensions $L_s = 15$ mm and $R_s = 13.5$ mm followed by a divergent MN. 2.45 GHz electromagnetic waves are emitted by a stainless steel antenna of 0.9 mm radius placed at the thruster axis and the electron resonance condition is achieved at 875 G. Two different prototypes are tested, were the magnetic field is either generated by a solenoid (SO) or by a permanent magnet (PM) named ECR-PM-V1 in [131]. The back of the source is limited by a dielectric back plate made of boron nitride. The thrusters are electrically isolated by an in-line microwave component called Direct Current Blocker (DC block), which allows them to be electrically floating. The propellant is injected at the back plate of the source through two holes of 2 mm diameter located symmetrically at two mid-points of the source radius. The external magnetic field strength at the thruster back plate is fixed at 900 G for both prototypes, but the PM thruster has a smaller axial gradient, which shifts downwards the plasma detachment and results in a less divergent plasma beam. Figure 3.1 compares the magnetic field strength at the thruster's axis as a function of the distance to the thruster exit plane (corresponding to $z = 0$).

3.2.2 Subsystems and operating conditions

The microwave power is injected by means of a solid state amplifier. It is constituted by a signal generator (between 2.3 and 2.6 GHz) and a linear amplifier, and the maximum power it can deliver is around 100 W. The power is transmitted by a 50 Ohm coaxial cable, whose losses have been measured using a vector network analyzer. The output of the generator is connected directly to a circulator with a 50 Ohm load, which allows the reflected power to be absorbed and dissipated in the load. Subsequently and before entering the feedthrough, the power line contains

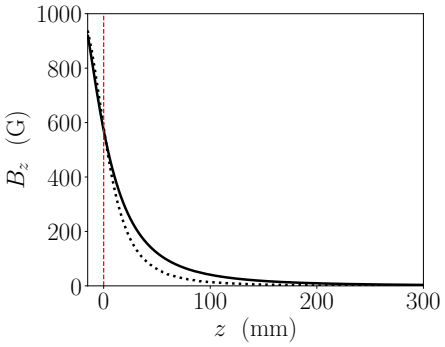

Figure 3.1: Applied magnetic field strength at thruster axis in the PM (——) and SO (·····) ECR prototypes. $z = 0$ corresponds to the thruster exit plane.

a bi-directional coupler connected to two different diodes that are in charge of measuring the forward and reflected power at this point of the line. Figure 2.2 shows a schematic of the the microwave power line set-up.

In this study, the power absorbed by the plasma was set at 30 ± 2 W (determined by recording the input and reflected power measured by the bi-directional coupler). The measured reflected power was less than 3 % in all the cases presented here. The level of radiated power was evaluated when the thruster was ignited and was found to be negligible and the attenuation level in the coaxial cable inside the chamber was characterized with a Vector Network Analyzer. With this procedure, the absorbed power was estimated to be very close to the input power in this set-up ($\approx 95\%$). Finally, the xenon mass flow rate varied within the range $\dot{m} = (0.08 - 0.2)$ mg/s. The tests have been done at ONERA-Palaiseau facilities. The vacuum chamber, known as B09, consists of a cylindrical vessel with dimensions of 0.8 m diameter and 2 m long. The pumping is done by one primary pump, three Pfeiffer Hipace (2000 l/s N_2) turbomolecular pumps, and one cryogenic pump, allowing to achieve a background pressure of 10^{-7} mbar and a xenon pumping speed of 13000 l/s.

3.2.3 Diagnostics

In order to characterize longitudinal profiles of the plasma properties along the MN expansion, two different diagnostics were installed: Laser Induced Fluorescence (LIF) optical set-up to measure the ion velocity distribution function (IVDF) and cylindrical Langmuir probes to obtain information about the electron energy

probability function (EEPF). Additionally, a Faraday gridded probe was installed in a rotation stage placed at 28 cm from the thruster exit plane to perform angular scans of the total ion current. The different diagnostics are detailed below.

Cylindrical Langmuir probe

A cylindrical Langmuir probe of 0.1 mm diameter and 6 mm length was placed in a 2D translation stage, so it could operate at different longitudinal positions. The tip probe was made of tungsten wire and it was held in a ceramic tube. The I-V characteristic curve was successfully obtained at different locations without perturbing significantly the thruster performance (from 75 to 250 mm from the thruster exit plane for the PM prototype, and from 40 to 280 mm for the SO prototype) and local values of plasma potential, electron density and electron temperature were computed. It was not possible to place the probe closer to the thruster, because significant variations on the floating thruster potential were detected, an indication that the diagnostic was interfering with the thruster performance. The floating thruster potential was measured using a commercial multimeter external to the vacuum chamber.

One of the main concerns when placing a Langmuir probe in the presence of a magnetic field is the tip orientation with respect to the magnetic field lines. The Larmor or gyro radius was expected to be greater than the probe radius in all the range studied here, so no magnetic field effect should in principle be captured [63]. To ensure this fact, and since the gyro radius was not well known due to the uncertainty on the electron temperature, a previous test was performed with the Langmuir probe placed in a rotation stage. Acquisitions were taken with the probe placed parallel and perpendicular to the magnetic field lines and no significant difference in the I-V curve was found. For this reason, the effect of the probe orientation was neglected in the present work, and the electron temperature shown here should be understood as a total value of the electron energy (including parallel and perpendicular orientations).

LIF

A 1D Laser Induced Fluorescence diagnostic was mounted together with the electrostatic probes (Langmuir and Faraday gridded) to measure the projection of the ion velocity distribution function along the thruster axis direction. All optics were fixed to the vacuum chamber, and the thruster was moved using a 3D translation stage. With this setup, any point in the thruster source and along the plume could be measured. It must be noticed that this diagnostic was only installed when operating the PM thruster, since the SO prototype includes water cooling tubes and high current cables (130 A) that were not compatible with the 3D translation stage.

The LIF calibration and specific details of the optical setup are explained in [67], as well as the main results from the LIF measurements presented in this work. The laser consists of a SDL-TC10 tunable laser diode with 20 mW of maximum output power and the frequency span for these measurements was 25 GHz, which allowed measuring axial ion velocities up to 20 km/s.

The laser was aligned with the thruster axis and injected through a lens of 25 mm diameter. The detection was composed of a 50 mm lens and a 200 μm optic fiber. The probed volume was around 1 mm diameter. The optics were installed 450 mm from the measurement point, to avoid perturbation and intrusion in the plasma beam. The detection was installed with an angle of 35^o and a camera was fixed to the thruster to verify alignment between the laser and the detection. Figure 3.2 schematizes the set-up.

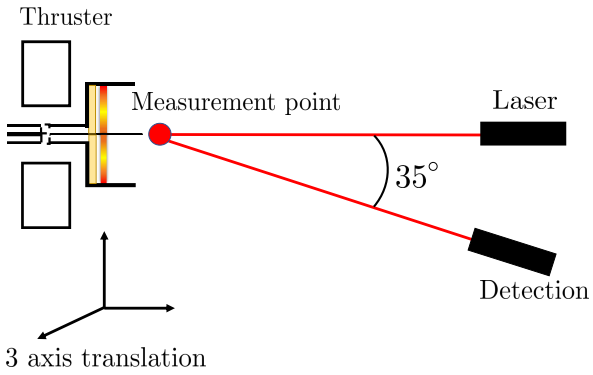

Figure 3.2: Schematic of optical LIF setup inside the vacuum chamber

Faraday gridded probe

To estimate the mass utilization efficiency at different mass flow rates, the total ion current was measured with a one-grid Faraday probe. Angular profiles of the ion current density were obtained by performing angular scans of current with the probe mounted in a rotation stage at 28 cm from the thruster exit plane. The beam is assumed to be axisymmetric and composed by only single ionized ions. The probe used here is described in [74], and consists of a 6 mm diameter collector with a front grid of 60% transparency. The voltage was biased at a sufficiently negative value to ensure the probe was working in the ion saturation region of the I-V curve. The procedure was the following: The probe was placed facing the plume at the thruster axis, and the collector was biased more negatively until there was no variation in the collected current ($\approx$ -300 V). Then, the ion current was estimated by means of an external resistor. The Faraday probe was only mounted in the PM prototype setup.

3.3 Results

This Section presents the results of the two magnetic systems setups used for the ECR thruster. All the tests presented here were carried out at 30 ± 2W of absorbed power and xenon mass flow rates of $1, 1.5, 2.0$ sccm for the PM thruster and $0.8, 1$

sccm for the SO thruster. In both setups, the Langmuir probe described in Section 3.2 was installed in a translation stage which allowed the probe tip to be aligned with the thruster axis at different axial positions. Additionally, in the PM thruster setup, the LIF optical assembly and the Faraday probe described in Section 3.2 were also installed. In this Section results are organized by diagnostic.

3.3.1 Langmuir probe: Plasma properties ϕ, n_e, T_e

The plasma potential at each axial position was obtained from the inflection point of the I-V characteristic curve, and the electron energy distribution function (EEDF) was computed with the Druveysteyn formula [51], shown in equation (3.1), where $F(\epsilon)$ represents the EEDF, $g(\epsilon)$ the electron energy probability function (EEPF), m_e and q the electron mass and charge respectively and A the probe surface area. Figure 3.3 shows an example of the I-V curve and the calculated EEPF at 1 sccm, at 105 mm from the PM thruster exit plane. The electron density and temperature can be computed by taking the corresponding integrals of the EEDF, as it is shown in equation (3.2) and equation (3.3). Notice that since the EEPF is not Maxwellian, T_e stands for an effective electron temperature. These formulas give reliable results when a magnetic field is present if the condition $r_L >> r_s$ is satisfied, where r_L represents the electron Larmor radius or gyroradius and r_s the effective collecting area of the probe. This assumption can be problematic at the closest locations to the thruster exit plane, since the electron Larmor radius could remain of the same order as the probe sheath length. For instance, for the SO thruster, at z=80 mm the r_L expected should be around 4 mm, while the estimated r_s is 2.61 mm. However, in most of the analyzed region, the condition $r_L >> r_s$ is well satisfied.

$$F(\epsilon) = g(\epsilon)\sqrt{\epsilon} = \frac{2\sqrt{2m_e\epsilon}}{q^3 A}\frac{d^2 I}{dV^2} \tag{3.1}$$

$$n_e = \frac{2\sqrt{2m_e}}{|q|A}\int_0^{-\infty}\frac{d^2 I}{dV^2}\sqrt{\frac{V}{|q|}}\,dV \tag{3.2}$$

$$T_e = \frac{4\sqrt{2m_e}}{3n_e A}\int_0^{-\infty}\frac{d^2 I}{dV^2}\left(\frac{V}{|q|}\right)^{3/2}\,dV \tag{3.3}$$

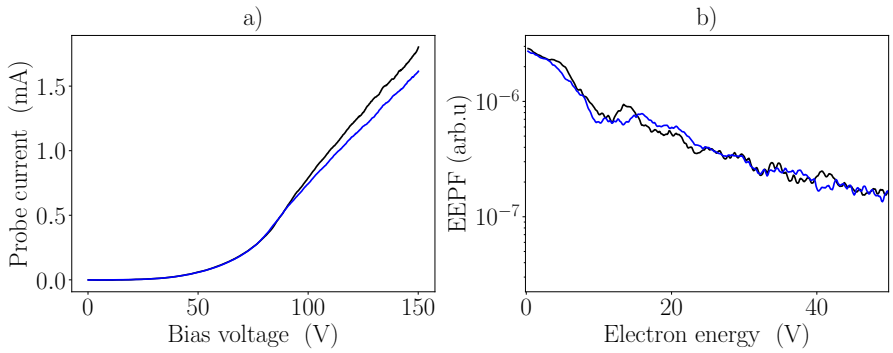

Figure 3.3: a) I-V curves at 2 sccm of xenon, at different axial locations from the PM thruster exit plane and b) the computed EEPF.

Figure 3.4 shows the plasma properties measured with the Langmuir probe along the center line of the PM thruster plume. Plasma potential ϕ, electron density n_e and electron temperature T_e have been estimated from 75 mm to 250 mm downstream, at three different xenon mass flow rates 1, 1.5 and 2 sccm, where $z = 0$ corresponds to the thruster exit plane. The plasma potential ϕ has been plotted referred to its value at $z = 75$ mm. Figure 3.4 (a) shows there is a direct relation between the mass flow rate and the plasma potential profile in the studied region: at higher mass flow rates, lower is the plasma potential drop. This behaviour is directly related to the electron temperature at the plasma source [74], which is highly dependent on the mass flow rate.

The spatial range of the Langmuir probe measurements was limited to 250 mm from the thruster exit plane due to the translation stage length. Moreover, positioning the probe closer than 75 mm from the exit plane disturbed significantly the thruster performance. For this reason, within 0-75 mm, the experiment was considered highly intrusive. Although the plasma potential profiles have been found to be almost flat beyond 200 mm, upstream of 75 mm a high ambipolar potential gradient is expected, and therefore the near region can not be neglected to estimate the entire plasma potential profile curve. In the ECR thruster tested here, with its particular magnetic field topology, the first 10 cm down from the thruster exit plane are crucial to the ions acceleration (and therefore to the plasma potential), as it is confirmed in Section 3.3.2. In order to complete the near region of the plasma potential profile, the LIF optical setup was installed, total ion energy was assumed to

be conserved, and the plasma potential in the near region was estimated by means of the LIF diagnostics.

Figure 3.4 (b) shows the estimated electron density n_e measured with the Langmuir probe. As it is expected, it shows an increase with the mass flow rate. At 75 mm, densities in the order of 10^{15} m^{-3} have been found. Finally, the electron temperature T_e shows the opposite behaviour; it decreases with the mass flow rate (see Figure 3.4 (c)). The total absorbed power measured for all cases is 30 W, so for lower mass flow rates, more energy is spent in heating the electrons, instead of ionizing the plasma. An effective electron cooling has been measured along the expansion at different operating conditions. To identify the electron cooling rate, the electron temperature has been plotted against the electron density in a logarithm scale in Figure 3.4 (d). Polytropic coefficients of 1.23 ± 0.02, have been found, all of them below the adiabatic expansion coefficient 5/3 and similar to the values found by other authors in magnetically expanding plasmas [78, 136]. However, this value only corresponds to a delimited region of the expansion.

Experimentally, covering the whole region of the expansion can add insight on the electron cooling mechanism, and in this sense, the Langmuir probe measurements in the SO thruster plume represent a farther zone of the MN, where there is a higher drop of the magnetic field strength. Figure 3.5 shows the plasma properties measured with the Langmuir probe along the magnetic field expansion of the SO thruster. The Langmuir probe was operated from $z = 40$ to $z = 290$ mm. In this experiment, the thruster performance was found stable from 40 mm downwards. As it can be observed in Figure 3.5 (a), in the range from $z = 75$ mm to $z = 250$ mm, at 1 sccm, the plasma potential has decreased around 35 V, while in the same spatial region for the PM thruster, the total drop was around 80 V. This is due to the fact that the acceleration region for the PM thruster is wider than for the SO thruster, which is a direct consequence of the MN topology. Concerning the plasma density, a factor of two has been found between the SO thruster and the PM thruster for the same operation conditions, being higher in the SO thruster plume (see Figure 3.5 (b)).

Interestingly, the electron temperature profile measured in the SO thruster plume differs from the tendency measured along the nozzle of the PM thruster. As it is shown in Figure 3.5 (c), it is possible to identify two different regions; while the first measurements from $z = 40$ to $z = 100$ mm reveal a sharp decrease in the

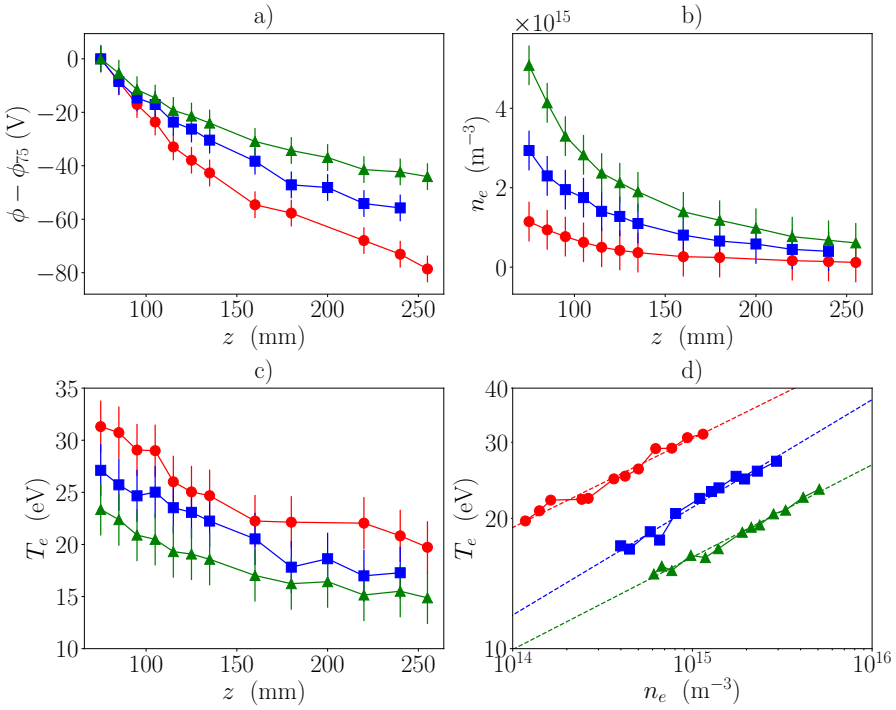

Figure 3.4: Plasma properties measured with the Langmuir probe, along the center line of the PM thruster. $z = 0$ corresponds to the thruster exit plane. Measurements were taken at 30 W of power and different mass flow rates: 1 sccm (—●—) 1.5 sccm (—■—) , 2 sccm (—▲—).

electron temperature, beyond $z = 100$ mm the curve remains almost flat, reaching an asymptotic value around 10 eV. In order to study this behaviour, the electron temperature is plotted against the electron density in a logarithm scale (Figure 3.5 (d)). In contrast to the PM thruster, two different polytropic coefficients γ have been identified here, $\gamma = 1.55$ close to the thruster exit and $\gamma = 1.17$ farther downstream. Similar trends have been found at 0.8 sccm (—◆—) and 1 sccm (—●—) of xenon in the SO thruster plume, being the total plasma potential drop at 0.8 sccm slightly higher. The experiments by Kim *et al.* in [69, 70] also found various values of the polytropic index along a MN expansion. In conclusion , these results indicate that the plasma expansion is more complex than polytropic. Indeed, the the MN model briefly presented later will confirm that there is not a simple polytropic law.

In Figure 3.6 the electron density has been plotted against the plasma potential in logarithm scale, and compared to the Boltzmann relation and the different polytropic cooling laws. In the PM thruster (Figure 3.6 (a)), a polytropic cooling

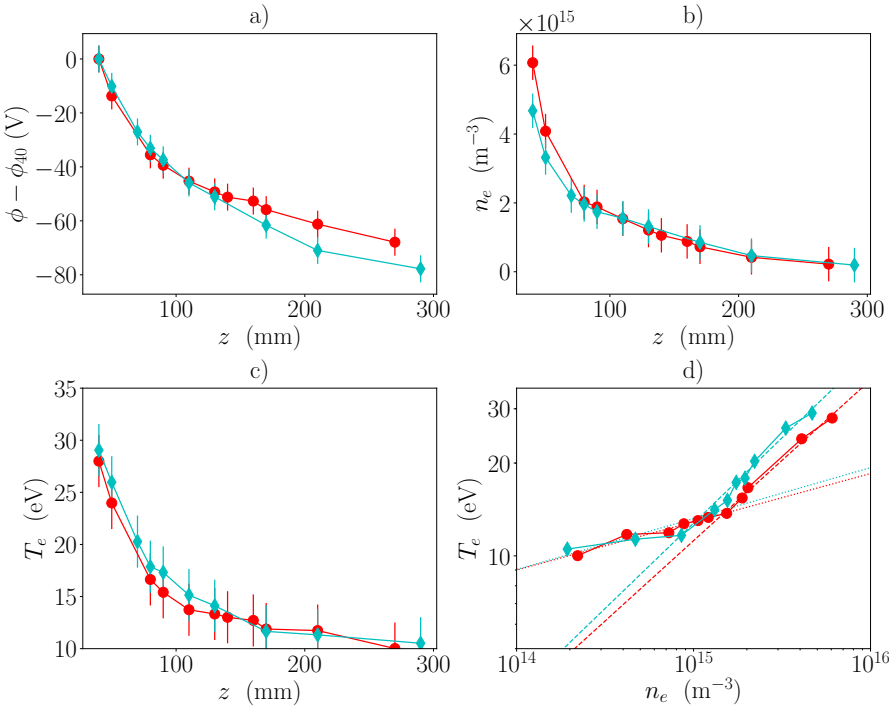

Figure 3.5: Plasma properties measured with the Langmuir probe, along the center line of the SO thruster. $z = 0$ corresponds to the thruster exit plane. Measurements were taken at 30 W of power and different mass flow rates: 0.8 sccm ( ) 1 sccm ( )

.

law represents well the near region of the expansion, but downstream it leads to a non-negligible deviation. In the SO thruster plume (Figure 3.6 (b)), the non local behaviour (i.e. change in polytropic factor) is again visible.

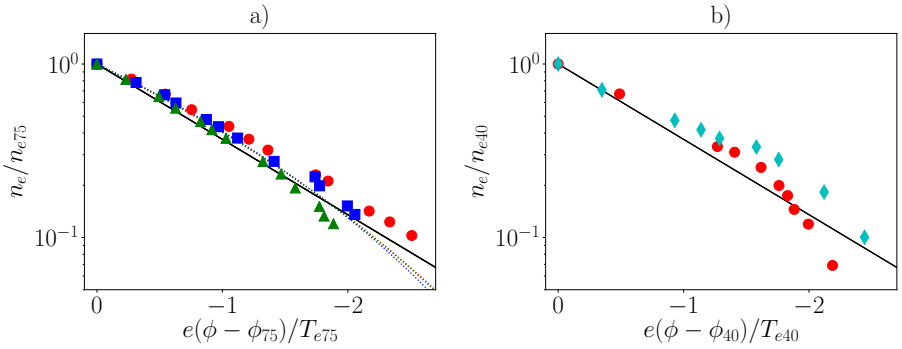

Figure 3.6: Normalized plasma density n_e/n_{e75} versus $e(\phi - \phi_{75})/T_{e75}$ estimated with the Langmuir probe for a) PM thruster and Normalized plasma density n_e/n_{e40} versus $e(\phi - \phi_{40})/T_{e40}$ b) SO thruster. 0.8, 1, 1.5, and 2 sccm are represented by (♦), (●),(■),(▲), respectively. The solid line corresponds to the Boltzmann expansion, while the dashed lines in a) represent polytropic expansions with $\gamma = 1.23 \pm 0.02$.

3.3.2 LIF: Mean axial ion velocity u_i

The optical LIF diagnostics were installed together with the Langmuir probe in the PM thruster set-up. The thruster was operated at 30 W and at three different mass flow rates. LIF measurements were performed at several axial positions along the center line of the thruster axis; inside the thruster source and in the near plume region (from $z = -5$ mm and $z = 125$ mm). Three examples of different LIF spectra obtained with the same acquisition parameters (sweep time of the laser and time constant of the lock-in amplifier) are shown in Figure 3.7 (a). It is noteworthy that there is a broadening of the peaks inside the thruster, which could be either due to Zeeman splitting of the 834.7 nm transition, or to the production of charge exchange ions. The possible effect of Zeeman splitting in this region is a current line of research. Relative density and mean axial velocity have been computed and represented in Figure 3.7 (b). Since the ECR region is located near the backplate, and the magnetic field is fully divergent, the generated ions are already slightly accelerated inside the source. The measured ion velocity at the thruster exit plane is 2250, 1950 and 1900 m/s at 1, 1.5 and 2 sccm, respectively. Currently, an uncertainty of the ECR thruster performance is the location of the sonic transition from a subsonic plasma jet to a supersonic beam, due precisely to the coupling of ionization and acceleration processes, so obtaining accurate data of the ion velocity

and density in this region can be crucial to understand this phenomenon. Figure 3.7 (b) shows a unexpected trend of the relative ion density between 5 and 10 mm from the thruster exit. These results could be due to production of secondary ions in this region, but it must be confirmed with additional measurements.

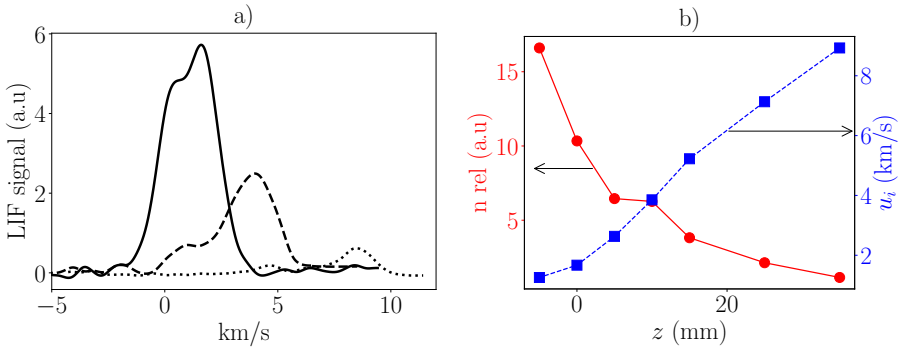

Figure 3.7: a) LIF signal already centered with the reference discharge at different axial positions: -5 mm (——), 10 mm (- - -) and 35 mm (·····). b) Computed relative density (—●—) and mean axial velocity (—■—) from the LIF signals. Operating conditions were 1.5 sccm and 30 W.

The mean axial ion velocity has been determined from the LIF signal for each axial position, at 30 W of absorbed power and three different mass flow rates 1, 1.5 and 2 sccm. The longitudinal profiles are shown in Figure 3.8 (a). Lower mass flow rates lead to higher ion velocities. The highest ion velocity measured at 100 mm from the thruster exit in this set-up was 16 km/s for 1 sccm. However, the ion current density also decreases with the distance, and LIF measurements could not be performed beyond 100 mm at 1 sccm. The ion velocity axial gradient has been also plotted in Figure 3.8 (b). It can be seen that the strongest gradient is located between 5 and 15 mm from the thruster exit plane, region where the electric field is more intense. As well, the maximum velocity gradient is shifted at the different operating conditions, being closer to the thruster exit plane at lower mass flow rates.

It can be seen that the acceleration region is not complete at the end of the LIF measurement range, henceforth LIF results in the near plume region have been completed with Langmuir probe measurements in the far plume region.

Finally, by assuming total ion energy is conserved, it is possible to calculate the plasma potential in the near plume from LIF measurements by overlapping the curves of kinetic energy and plasma potential in the region where LIF and

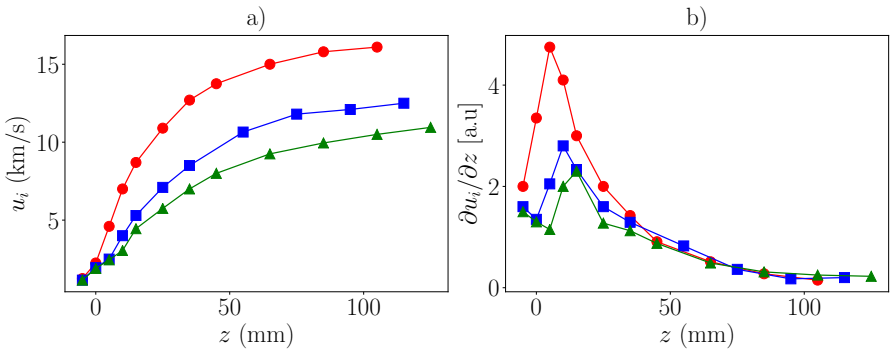

Figure 3.8: a) Mean axial ion velocity measured with the LIF set-up, along the center line of the PM thruster and b) its axial derivative normalized between 0 and 1. $z = 0$ corresponds to the thruster exit plane. Measurements were taken at 30 W of power and different mass flow rates: 1 sccm (—●—) 1.5 sccm (—■—) , 2 sccm (—▲—).

Langmuir probe operated simultaneously. The resulting plasma potential profile from the thruster exit to the farthest measurement point, referred to the plasma potential at the ECR source is shown later in Figure 3.13 (b). The total plasma potential drop from 0 to 250 mm is 236, 145 and 104 V, for 1, 1.5 and 2 sccm, respectively. It is noteworthy that this potential drop is not necessarily the total ion energy, since although the plasma potential profile is almost flat beyond 200 mm, the plasma expansion is not complete. One of the main contributions of this work is to compute the finite potential drop based on a fluid-kinetic plasma expansion model, and relate the percentage of plasma expansion with the spatial coordinates.

3.3.3 Faraday probe: Ion current

The gridded Faraday probe detailed in Section 3.2.3 was installed in the PM thruster set-up. Angular scans of ion current density were taken at 28 cm from the thruster exit plane, at 30 W of absorbed power and three different mass flow rates 1, 1.5 and 2 xenon sccm. Figure 3.9 shows the measured angular profiles of ion current density, computed taking into account the surface of the probe and the grid transparency. It is noteworthy that the angular profiles of Figure 3.9 do not reach the maximum current at 0 degrees, which is probably due to the fact that the antenna is located at the center line of the thruster, and influences the shape of the plasma beam. As well, the current design of the gas injection could also lead to non-homogeneities already in the plasma source, as it was pointed out by Vialis *et al.* in [131]. There is

also a residual current at 90 degrees, which increases with the mass flow rate, which suggests that it could be due to charge exchange collisions or additional ionization due to collisions between the ambient plasma and plume electrons.

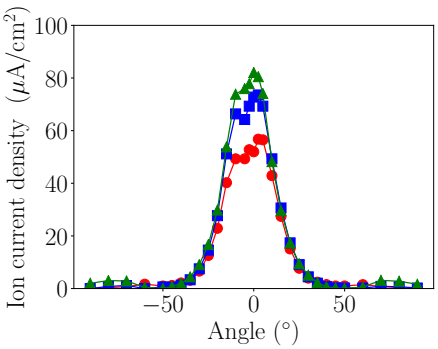

Figure 3.9: Angular scan of ion current density at 28 cm from the thruster exit: 1 sccm (—●—), 1.5 sccm (—■—) and 2 sccm (—▲—).

The total ion current I_i is computed integrating the ion current density assuming an axisymmetric plume and taking into account the distance to the thruster axis. Related to that current, a first parameter assessing the performance efficiency of the thruster is the mass efficiency, defined as

$$\eta_m = \frac{I_i m_i}{\dot{m} q} \tag{3.4}$$

where: m_i is the ion mass, q is the elementary electric charge, and $\dot{m}$ is the neutral gas mass flow rate. A second efficiency parameter is related to the plume divergence: if λ represents an effective far field divergence angle [27], a "plume efficiency" is given by $\cos^2 \lambda$. Tab. 3.1 details these two performance parameters, together with the measured chamber pressure. The low measured mass efficiency is an indication of a poor ionization, which is directly related to the mass-flow rate to power ratio, as it was reported in [131].

3.4 Comparison of plume data with theory

In order to understand and analyze the experimental data on the magnetized plasma plume emitted by the thruster, we resort to models of the MN. The most suitable one for a near-collisionless plasma is the kinetic one by Martínez-Sánchez *et al.* [83] which considers the expansion of a collisionless, quasineutral, magnetized plasma

$\dot{m}$**(sccm)**	p_{ch} **(10^{-6} mbar)**	$\eta_m(\%)$	$\cos^2\lambda$	T_{e*} **(eV)**	z_0 **(mm)**
1	2.8	23.2	0.857	44	7.4
1.5	3.5	17.6	0.892	27	11.8
2	3.7	14.2	0.887	19	12.5

Table 3.1: Chamber pressure, mass utilization efficiency η_m and plume efficiency $\cos^2\lambda$ for the PM thruster. Two last columns: estimated electron temperature at the sonic point and its location for the MN model fitting.

in a paraxial convergent-divergent MN, and solves for the ion and electron velocity distribution functions and the ambipolar electric potential. In the next Subsection, that ideal model is adapted to a divergent-only nozzle, in a way similar to the one Merino *et al.* [95] followed for an unmagnetized plasma plume. Then, Subsection 3.4.2 compares the experimental data with that model.

3.4.1 Divergent nozzle model

Let us consider a divergent nozzle created by an applied magnetic field $B(z)$ monotonically decreasing from $z = z_0$, where from a plasma beam is with near-sonic conditions, to be defined below. This plasma is collisionless, quasineutral, current-free and fully-magnetized. Therefore, ions and electrons are perfectly channeled by the magnetic streamtubes. The model, being paraxial, determines only axial flows of radially-averaged magnitudes. If the initial cross-section of the beam is A_0, the evolution of the cross section is inversely proportional to B: $A = A_0 B_0/B$.

Individual electrons conserved their total energy E_e, and magnetic moment μ_e, defined as

$$E_e = \frac{m_e w_{e\parallel}^2}{2} + \frac{m_e w_{e\perp}^2}{2} - e\Delta\phi \tag{3.5}$$

$$\mu_e = \frac{m_e w_{e\perp}^2}{2B} \tag{3.6}$$

where: $w_{e\parallel}$ and $w_{e\perp}$ are velocity components parallel (i.e. axial) and perpendicular to the magnetic field ($w_{e\parallel}$ is also the electron gyrocenter velocity) and $\Delta\phi = \phi - \phi_0 \leq 0$.

For a current-free plasma, the self-consistent electric potential ϕ is monotonically decreasing, its role being to adjust the downstream current of very mobile electrons to the ion current, in a similar way a Debye sheath does close to a dielectric wall. However, when electrons are magnetized there is an additional effect. Combining the above two equations, the electron axial velocity satisfies

$$\frac{m_e w_{e\parallel}^2}{2} = E_e - \mu_e B + e\Delta\phi. \tag{3.7}$$

Therefore, the axial forward-motion ($w_{e\parallel} > 0$) of electrons is governed by two opposing forces: the electric one, which decelerates them, and the magnetic mirror effect, which accelerates them. The opposite is naturally true for back-marching electrons. As a consequence three different populations of electrons can be found in a divergent nozzle [98]: *free electrons*, emitted by the source and lost downstream (which constitute the electron current); *reflected electrons*, emitted by the source and turned back to the source; and *doubly-trapped electrons*, bouncing between two intermediate positions of the plume.

At the source, only the forward-marching velocity distribution function $f_{e+}(z_0)$ can be postulated, while the backward-marching distribution $f_{e-}(z)$ (at any location) is part of the solution. The semi-Maxwellian distribution

$$f_{e+}(E_e)|_{z_0} = n_{e*}\left(\frac{m_e}{2\pi T_{e*}}\right)^{3/2} \exp\left(-\frac{E_e}{T_{e*}}\right), \qquad w_{e\parallel} > 0, \tag{3.8}$$

is chosen here. Parameters n_{e*} and T_{e*} would be the electron density and temperature at the source, n_{e0} and T_{e0}, only if $f_{e+} = f_{e-}$. Since most source electrons are reflected back, $n_{e*} \approx n_{e0}$ and $T_{e*} \approx T_{e0}$. While the populations of free and reflected electrons are totally determined in terms of $B(z)$ and $\phi(z)$, the determination of the population of doubly-trapped electrons is out of the capabilities of a collisionless, stationary model. The same postulates than in [83] will be used here for that population. Macroscopic electron magnitudes such as density n_e, parallel particle flow $n_e u_e$, pressure $n_e T_e$, and parallel heat flux q_e, are determined as velocity moments of the local distribution function $f_e = f_{e+} + f_{e-}$, in the way explained in [83].

Ions also conserve their total energy and magnetic moment, but in this case, both the electric force and the magnetic mirror accelerate them downstream the divergent nozzle. As a consequence all ions constitute a free population, expanding supersonically, and a simple “cold fluid model" seems a good approximation [98].

Then, ion continuity and momentum equations are

$$n_i u_i/B = \text{const} = n_{i0}u_{i0}/B_0, \qquad u_i = \sqrt{u_{i0}^2 - 2e\Delta\phi/m_i}. \tag{3.9}$$

Using B as independent variable instead of z, the self-consistent electric potential profile, $\phi(B)$, is determined by satisfying[83] plasma quasineutrality

$$n_e(\phi(B), B) = n_i(\phi(B), B) \equiv n(B), \tag{3.10}$$

and the current free condition, i.e. the (constant) ion and electron flows are identical. This, together with quasineutality states that macroscopic ion electron velocities are the same: $u_e(B) = u_i(B)$.

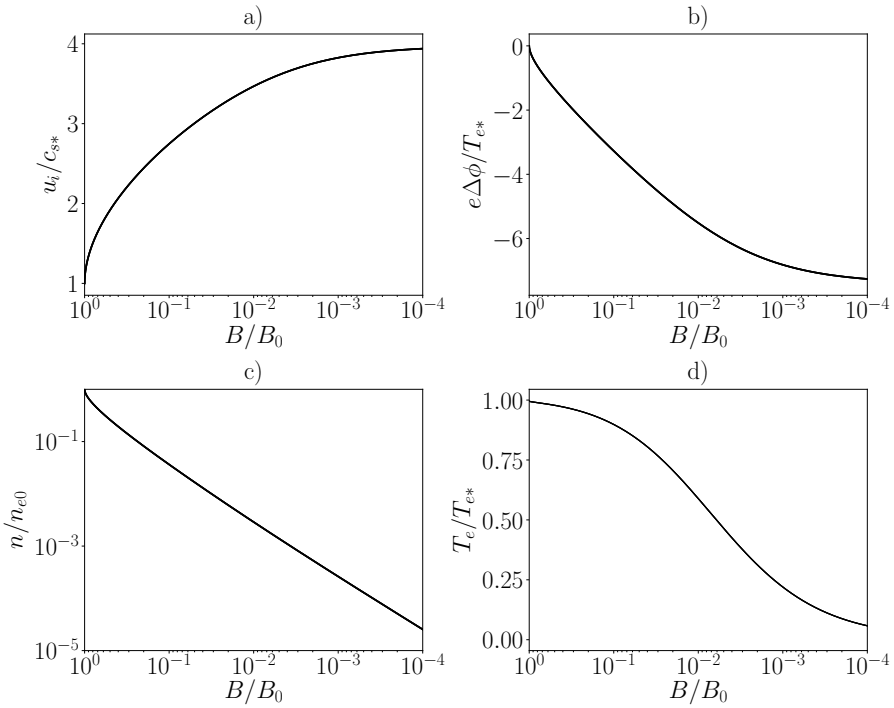

Figure 3.10: Plasma expansion according to the magnetic nozzle model.

The dimensionless solution of this problem depends on the injection location z_0 (or B_0), the initial velocity u_{i0}/c_{s*}, with $c_{s*} = \sqrt{T_{e*}/m_i}$ and the mass ratio m_i/m_e. Figure 3.10 plots plasma profiles for xenon, $u_{i0}/c_{s*} = 1$, and different z_0. Observe, first, that $T_{e0} \simeq T_{e*}$ indicating that $f_e(z_0)$ is fully Maxwellian except for the high-energy tail of free electrons. Second, electron (collisionless) cooling is high and motivated by the emptying of regions in the electron velocity space [95]. Third, the

total drop of the electric potential in the divergent nozzle for a current-free xenon plasma is about 7.4.

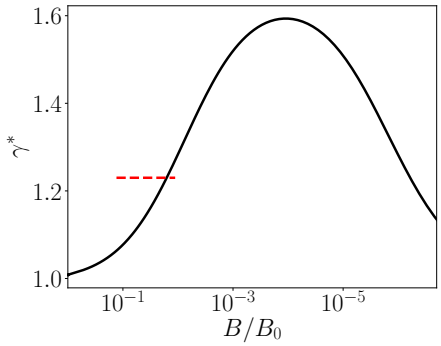

Figure 3.11: Equivalent local polytropic coefficient given by the model (——). The dashed horizontal red line (- - -) represents the average experimental value measured along the MN of the PM thruster.

Figure 3.11 plots an "equivalent" local polytropic coefficient defined as

$$\gamma = \frac{d \ln p_e}{d \ln n_e}, \tag{3.11}$$

. which presents large variations along the plume. The main message is then that there is not a polytropic behavior of the electrons. With this precaution taken, it still can be said that near the source electrons are near-isothermal, then tend to an adiabatic behavior, and finally to a (cold) isothermal behavior again. Observe that these changes occur along a range of B much larger than the experimental one.

Before experimental data are fitted to this model in the next Subsection, it is worth to highlight the main limitations of this ideal model. First, the model is paraxial and ignores partially the radial plasma expansion and totally the turning-back of magnetic lines. Second, it considers ions and electrons fully-magnetized down to z_∞, so, in practice, results are valid only in nozzle near-region. Third, the electron temperature at the source is assumed isotropic, which is not the situation expected in an ECR thruster. Theoretical work is underway to cancel or at least reduce these model restrictions [44, 110, 95, 106]

3.4.2 Fitting of experimental data along the MN of the PM thruster

The experimental results for the PM thruster presented in Section 3.3 are here fitted to the model just described. For a given mass flow, the fitting method is applied to the ion velocity profile experimental data of Figure 3.8 (a) and consists in the following. A range of values of T_e* is selected; remember that $T_{e*} \approx T_{e0}$. For each T_{e*}, the experimental point where $u_i = c_{s*}$ is taken as origin z_0 for the fitted curve and the full theoretical curve is plotted. Figure 3.12 shows the model prediction for three different values of T_{e*} overlapped with the experimental data, for 2 sccm flow. There is clearly a significant sensitivity to T_{e*}. A Least Square Error method is implemented to select the optimal T_{e*}. The ion velocity profiles were used for this fitting process because, first, LIF diagnostics allow to perform measurements from the thruster cavity to far downstream and, second, the uncertainty in the measurement of ion velocity is lower than the one regarding plasma density or electron temperature.

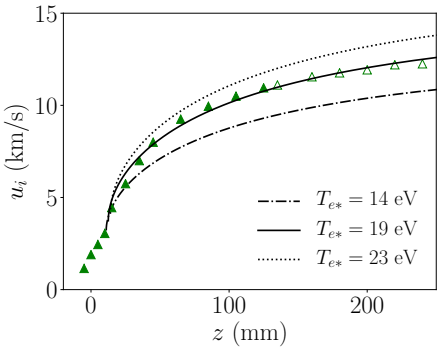

Figure 3.12: Experimental ion velocity curve $u_i(z)$ with the model predictions at different values of T_{e*} for 2 sccm.

The optimal T_{e*} for each of the experimental curves (1, 1.5 and 2 sccm) is shown with its corresponding sonic location z_0 in Tab. 3.1 (two last columns). Observe first, that the fitted sonic point is located around 1 cm from the thruster exit plane and shifts slightly downstream when increasing the mass flow rate. Second, the fitted electron temperature at the sonic point $T_{e0} \approx T_{e*}$ decreases with the mass flow rate, a trend in agreement with experimental evidence [74].

Figure 3.13 compares the experimental and best-fitted theoretical curves for the

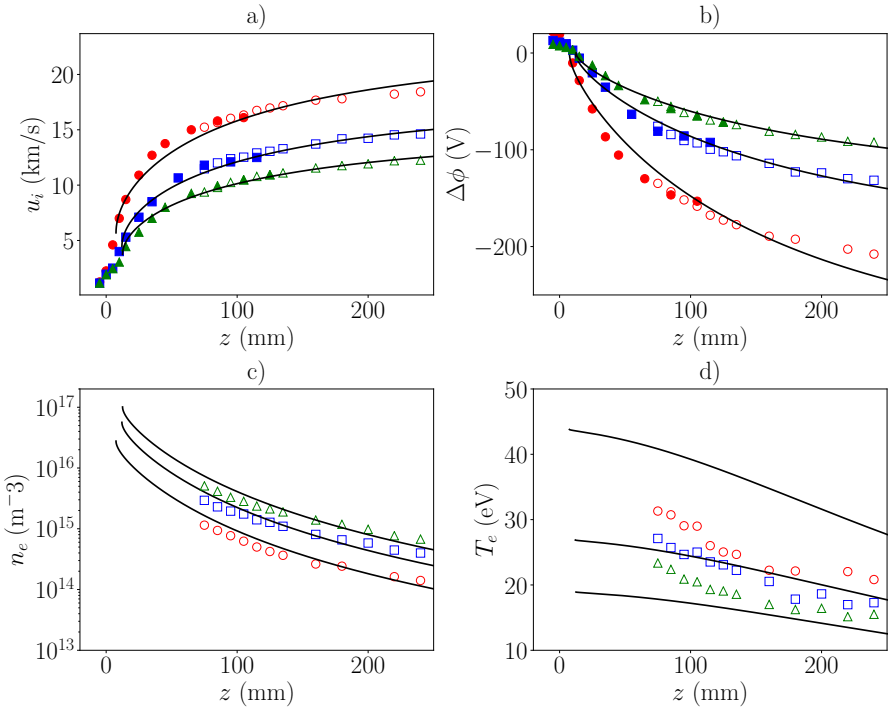

Figure 3.13: Plasma properties from LIF and Langmuir probe measurements compared to the quasi 1D model prediction (——) at 1 sccm (●, ○), 1.5 sccm (■, □) and 2 sccm (▲, △). a) Ion velocity u_i b) Plasma potential $\Delta\phi$ c) Electron density n_e d) Electron temperature T_e.

ion velocity, the plasma potential, the electron density and the electron temperature. Figure 3.13 (a) shows that the agreement is rather good for the supersonic u_i; a bit worse for 1sccm. Figure 3.13 (b) shows also a good agreement for the plasma potential. The model estimates that at the farthest measurement point ($z = 250$ mm), the expansion is almost 70 % complete, and therefore the ratio between the total potential drop and the estimated electron temperature is around 5, which correlates well with the values found by Lafleur *et al.* in [74] in the SO thruster described here.

Figure 3.13 (c) compares the plasma density measured with the Langmuir probe and the theoretical curves. The plasma density at the plasma reservoir n_0 has been estimated assuming flux is conserved along the measurement line (recall $n_0 \approx n_{e*}$), that is $nu_i/B = const.$ The estimated plasma density at the sonic point n_0 is 2.77, 5.56, and 10.0 in 10^{16} m^{-3} units, for 1, 1.5 and 2 sccm, respectively. The model fairly describes the density drop in the measurement region, although

additional data nearest the thruster exit s would be necessary to confirm the results. However, Figure 3.13 (d) highlights that the electron temperature estimated by the model only agrees reasonably with the experimental results at 1.5 sccm, disagreeing significantly at 1 and 2 sccm. Finally, Figure 12 compares the average experimental polytropic coefficient (in a limited plume region) with the local coefficient from the model.

It can be concluded that the comparison of data and model is acceptable and promising taking into consideration the idealizations of the model. Temperature anisotropy, likely present in the plasma at the source and neglected in the MN model here, is a first major source of discrepancies here, and possibly more acute in the temperature profiles and for low mass flow rates (due to less electron-electron collisions). Work is in progress to include anisotropy in the MN model [44]. A second one is the relevance of ionization and collisional process in the real plasma plume, also neglected in the model. Incidentally, collisions would also justify that the sonic point is here placed inside the divergent nozzle and not at a MN throat [28, 81]. And finally, discrepancies should not be attributed exclusively to the theory. For instance, it is acknowledged that, in the data-set at 2 sccm, the uncertainty in the Langmuir probe post-processing or the increase of the background pressure could have an impact on the results.

3.4.3 Differences between the PM and SO thrusters

Measurements of the complete plasma potential profile were only performed along the MN of the PM thruster, since it was not possible to install the SO thruster in the LIF set-up. Therefore, the experimental data from the SO thruster can not be directly related to the model results. However, interesting features can be discussed. The model enhances the large variation of the local polytropic index along the expansion, a consequence of the collisionless cooling of the different electron subpopulations. The physical mechanisms that populate the doubly-trapped electron regions are a current subject of study; two of them are collisionality and variations of the plasma potential profile during the transient set-up [110]. The 2D magnetic field topology may influence the formation of the doubly-trapped regions, and therefore have a direct impact in the local electron cooling. As commented before, Kim *et al.* [69, 70] also found different polytropic indices when varying the

strength and configuration of the magnetic nozzle.

3.5 Conclusions

Experimental measurements of ion acceleration and plasma properties along the MN of two ECR thruster prototypes have been performed. The difference between both versions relies on the MN topology, one generated by a permanent magnet (PM) and the other by a set of solenoids (SO). Langmuir probe measurements along the thruster's axis at several mass flow rates have added insight of the plasma response at different upstream conditions. The dependence of the total plasma potential drop with the mass flow rate has been identified, as well as a significant electron cooling rate along the expansion.

In the PM thruster set-up, simultaneously with the Langmuir probe, laser induced fluorescence (LIF) diagnostics have been performed to obtain the mean ion velocity from the thruster cavity to 125 mm downstream. By assuming total ion energy is conserved, it has been possible to estimate the complete profile of plasma potential from the thruster exit to far downstream overlapping Langmuir probe and LIF measurements. Close to the thruster cavity, a broadening of the ion distribution function has been observed, which could be due to the Zeeman splitting effect. Further experiments are however needed to fully understand this outcome.

In parallel, a quasi-1D stationary fluid-kinetic model has been adapted to a fully divergent magnetic field, assuming quasineutrality and current-free expansion. The ion population is treated as a cold fluid species, while the electron distribution function is solved self-consistently accounting for magnetic mirror effects and electric potential barriers.

The unique solution for the ambipolar potential profile depends only on the ion to electron mass ratio m_i/m_e and the initial ion Mach number. A total potential drop of 7.4 times the upstream electron temperature is found for xenon.

A least square error method has been implemented to compare the experimental results with the theoretical model. With this method, it has been found that the ion velocity, plasma potential and electron density profiles for different mass flow rates fit well with the model. The highest error between the model and the experimental data has been found at low mass flow rates and for the temperature profiles, which is probably related to the anisotropy of the electron energy distribution function

already at the plasma reservoir plus the effects in the expansion of ionization and other collisional effects. A next step in this research will be to improve the model to incorporate electron temperature anisotropy in the plasma source and collisional effects.

On the experimental side, further work should address additional non-intrusive measurements close to the thruster exit, since for this ECR thruster prototype, the main acceleration region is concentrated in the first 10 cm from the thruster exit plane. Additionally, other diagnostics capable of detecting anisotropic plasma properties would definitely add insight to this research.

CHAPTER

FOUR

Macroscopic and parametric study of a kinetic plasma expansion in a paraxial magnetic nozzle

This Chapter is a transcription of the paper accepted for publication in the peer-reviewed journal Plasma Sources Science and Technology, by E. Ahedo, S. Correyero, J. Navarro-Cavallé and M. Merino. [6]. The style has been adapted to the layout of this Thesis.

Abstract

A kinetic paraxial model of a collisionless plasma stationary expansion in a convergent-divergent magnetic nozzle is analyzed. Monoenergetic and Maxwellian velocity distribution functions of upstream ions are compared, leading to differences in the expansion only on second and higher-order velocity moments. Individual and collective magnetic mirror effects are analyzed. Collective ones are small on the electron population since only a weak temperature anisotropy develops, but they are significant on the ions all over the nozzle. Momentum and energy equations for ions and electrons are assessed based on the kinetic solution. The ion response is different in the hot and cold limits, with the anisotropic pressure tensor being relevant in the first case. Heat fluxes of parallel and perpendicular energies have a dominant role in the electron energy equations. They do not fulfill a Fourier-type law; they are large even when electrons are near isothermal. A crude electron fluid closure based on a constant diffusion-to-convective thermal energy ratio is shown equivalent to the much invoked polytropic law. Analytical dimensionless parame-

ter laws are derived for the nozzle total electric potential fall and the downstream residual electron temperature. Electron confinement and related current control by a thin Debye sheath and a semi-infinite divergent magnetic nozzle are compared.

4.1 Introduction

The understanding of the expansion of magnetically-guided plasmas into vacuum is crucial to improve the propulsive performances of a magnetic nozzle (MN)[93]. This constitutes the main acceleration stage of some electrodeless plasma thrusters, proposed for in-space electric propulsion, such as the helicon plasma thruster (HPT)[123, 132, 115, 97], the electron cyclotron resonance thruster[68], the applied-field magnetoplasma dynamic thruster [71], and the variable specific impulse magnetoplasma rocket (VASIMR) [49]. Magnetized plasma expansions are also relevant in other fields of plasma physics, for example in plasma sources for material processing and manufacturing [77] or in astrophysical jets [12].

Magnetized plasma beam expansions have been investigated extensively during the past years, both theoretically [36, 132, 17, 9, 89, 91, 83] and in the laboratory [133, 73, 64, 47, 80, 24, 101, 66, 97]. Given the inherent difficulty of measuring downstream properties reliably in low-density plasma plumes, theoretical models and simulation codes with the capability of accurately predicting the plasma response in the MN become crucial to study these devices. In the realm of plasma models, several approaches exist. On the one side, fluid models tend to be computationally fast and can provide much insight on the main properties of the plasma two-dimensional(2D) expansion[9, 89, 92]. However, for a near-collisionless plasma, the closure of the fluid model with equations for the heat fluxes is far from obvious, and requires kinetic information on the plasma state. The fluid closure is generally more critical for electrons, which constitute a confined species with modest particle and energy drifts along the MN; ions are supersonically accelerated by the MN and its internal energy matters only in particular devices [90]. Commonly-claimed isothermal or polytropic closures for collisionless electrons lack proper physical justification: the first case is just an *ad hoc* simplification while the second one must be understood as a phenomenological closure based on fitting experimental data. This data fitting shows electron cooling in a divergent MN with a polytropic coefficient in the range 1.1-1.3 [78, 42, 69, 74].

Paraxial (i.e. quasi one-dimensional) MN models, relying on the Vlasov equation, are showing to be an affordable and fruitful way to analyze the exact kinetic expansion of a collisionless plasma beam. In this context, Martínez-Sánchez *et al.* [83] developed a steady-state model computing self-consistently the velocity distri-

bution function (VDF) of ions and electrons along a slender convergent-divergent MN. It was demonstrated that the downstream electron cooling and temperature anisotropy are a direct consequence of the emptying of regions of the velocity space of the electron VDF and that cooling determines the finite ambipolar potential drop along the MN.

The present paper aims to complete the analysis of Ref. [83] in several directions, part of them suggested from other, more recent works. In order of relevance, the first goal here is to analyze the equivalent fluid model of the MN. The solution of the Vlasov model of the paraxial MN is the VDF of ions and electrons along the nozzle. The successive integral moments in the velocity space of these VDFs provide the macroscopic plasma magnitudes, and the integral moments of the Vlasov equations they fulfill. This will allow, for instance, to assess the relevance, for ions and electrons, of (a) heat fluxes in the energy equations and (b) collective magnetic mirror effects in the momentum equations. The analysis of the equivalent fluid model was carried out partially by Sánchez-Arriaga, Zhou, *et al.* [110, 137] within a paraxial, *time-dependent* kinetic model of a divergent-only MN, finding out that electron heat fluxes were of the same order of magnitude as convective fluxes of electron thermal energy.

The second goal is to obtain parametric scaling laws of relevant plasma magnitudes, such as the total potential fall along the nozzle, or the downstream temperatures and heat fluxes. These laws are important for quick estimates of a MN performance without determining the full plasma response. Ramos et al. [106] carried out an analytical study of the asymptotic downstream response except for the heat fluxes.

The third objective is a detailed comparison of the different plasma response in the convergent and divergent regions of the MN, and the determination of the plasma conditions at the MN throat. Special attention will be given to the collective magnetic mirror effect on ions and electrons in each region and its coupling with the development of temperature anisotropy. Also, it will be shown that the ion VDF at the MN throat differs largely with the upstream ion VDF. This fact must be taken in to account when comparing convergent-divergent MN models with divergence-only MN models such as those of Refs. [110, 95]. In particular, the comparison of the present model with the convergent-only MN of Ref.[82] will be addressed. The convergent-only MN model ends in a wall at a throat preceded by a thin Debye

sheath. The similarities and differences between the plasma properties across this sheath and those across the whole divergent MN will be commented.

The last goal is to compare the plasma expansion for upstream monoenergetic and Maxwellian ion VDFs. Only the first case was considered in Ref. [83]. Velocity dispersion and heat fluxes are supposed to have a different importance in the two cases, mainly if the ion population is hotter than the electron one in the upstream source.

The chapter is organized as follows. Section 4.2 summarizes the key aspects of the kinetic MN model. Section 4.3 presents spatial results, discusses the two cases of ion VDFs, compares the physics within the convergent and divergent regions, and presents parametric results at the MN throat and far downstream. Section 4.4 discusses the macroscopic plasma equations, with special attention to the collective magnetic mirror effect and the relevance and modeling of the heat fluxes.

4.2 Model formulation

The kinetic MN model described in Ref. [83] is summarized here for self-containment. A convergent-divergent externally applied magnetic field $B(z)$ with a single maximum B_M located at $z = 0$ and vanishing at $z \to \pm\infty$ (where $B \to 0$) creates a MN that channels a *fully magnetized* ion-electron plasma generated at a source located at $z \to -\infty$. Subscripts '0', 'M', and '∞' will be used for locations $z \to -\infty$, $z = 0$, and $z \to \infty$, respectively. The kinetic model attempts to determine the steady state of the paraxial, collisionless, quasineutral, current-free, low-beta, and fully-magnetized plasma plume in the MN. In this asymptotic limit, particle drifts and induced magnetic field effects are negligible. This *ideal* fully magnetized model would fail of course, at $|z|$ large enough where ion and electron magnetization fades, but this fact is marginal to the goals of the present study, centered on understanding basic plasma phenomena of the MN expansion.

Since the spatial distance z does not appear explicitly in the model, a monotonic variable related directly to the non-monotonic magnetic field provides a more universal description of the spatial behavior. A convenient, space-like dimensionless variable is

$$\zeta = \text{sign}\,(z) \log_{10} \frac{B_M}{B}, \tag{4.1}$$

which places the throat M at $\zeta = 0$ and scales logarithmically with B.

The model will determine iteratively the ambipolar electric potential $\phi(\zeta)$ and the VDFs of electrons and ions along the central magnetic line of the MN. It is assumed (and then confirmed by the solution) that $\phi(\zeta)$ decreases monotonically along the expansion from $\phi(-\infty) = 0$ to $\phi(+\infty) = \phi_\infty (< 0)$; this *finite* total potential fall along the MN is to be determined too.

As a consequence of full-magnetization and lack of collisions, electrons and ions conserve their total energy E and magnetic moment μ, that is

$$E = \frac{m}{2}(w_\parallel^2 + w_\perp^2) + eZ\phi, \qquad \mu = \frac{mw_\perp^2}{2B}, \tag{4.2}$$

where: species subscripts have been omitted, m and Z represent, respectively, the particle mass and charge number, $w_\parallel$ is the particle velocity parallel to B (i.e. axial in this model), and $w_\perp$ is the perpendicular velocity. Solving equation (4.2) for the two velocity components yields

$$w_\perp(\zeta, \mu) = \sqrt{\frac{2\mu B(\zeta)}{m}}, \tag{4.3}$$

$$w_\parallel(\zeta, E, \mu) = \pm\sqrt{\frac{2}{m}\left[E - eZ\phi(\zeta) - \mu B(\zeta)\right]}, \tag{4.4}$$

where $w_\perp$ is positive by definition, while the plus and minus signs for $w_\parallel$ indicate the forward and backward marching of particles, respectively.

Condition $w_\parallel(\zeta, E, \mu) = 0$, i.e.

$$E = Ze\phi(\zeta) + \mu B(\zeta), \tag{4.5}$$

sets the spatial turning point for particles of given (E, μ); thus $eZ\phi + \mu B$ acts as the effective potential function for the parallel motion of a particle. Alternatively, equation (4.5) defines the maximum magnetic moment μ_m allowable for a particle with energy E to reach location ζ:

$$\mu_m(\zeta, E) = \frac{E - eZ\phi(\zeta)}{B(\zeta)}. \tag{4.6}$$

Figure 4.1(a)-(b) displays three typical spatial profiles of μ_m for ions (i) and electrons (e) and three different energies E. The curves show all the possible topologies found with the model discussed here.

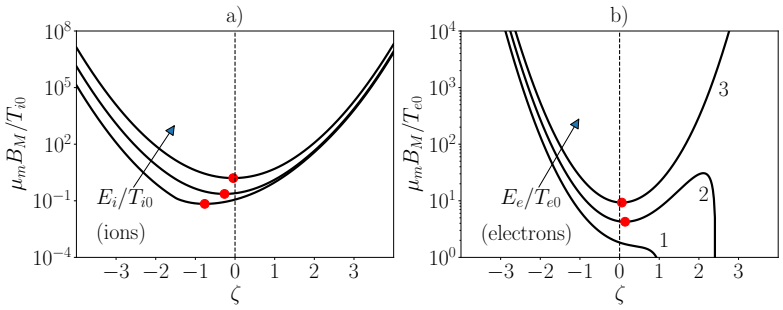

Figure 4.1: Three typical curves of μ_m for three ion and three electron energies (these ones increasing from curve 1 to 3). The red dots correspond to local minima $\mu_T(E)$. This example corresponds in fact to the solution for $m_i/m_e = 10^4$ and $T_{i0}/T_{e0} = 10$.

The axial electric field pushes ions downstream and electrons upstream in both the convergent and divergent side of the nozzle. The magnetic mirror effect, in contrast, tends to keep both types of particles away from the throat region. This leads to different behaviors (a) of ions and electrons, and (b) in the convergent and divergent sides of the MN. Taking first the case of ions, for a given energy E in Figure 4.1(a), the curve $\mu_m(\zeta)$ always has a single minimum μ_T (red dot in the figure) at $\zeta = \zeta_T$ in the convergent side. Ions from the upstream source with low enough μ can surpass that location and therefore are *free* ions reaching $\zeta = +\infty$. The rest of them are *reflected* back to the source. Therefore, for given E, there are four μ-subregions in the ion phase space: $\mu < \mu_T$, for *free* ions; $\mu_T < \mu < \mu_m$ and $\zeta < \zeta_T$, for *reflected* ions; $\mu_T < \mu < \mu_m$ and $\zeta > \zeta_T$, devoid of (upstream) ions; and $\mu > \mu_m$, forbidden energetically.

For electrons the situation is more complex. First, electrons with $E > e|\phi_\infty|$, such as those of curve 3 of Figure 4.1(b), are *free* electrons, reaching $\zeta = +\infty$, or are *reflected* back to the source, depending on their magnetic moment μ. Second, electrons with $E < e|\phi_\infty|$ lead to curves of type 1 or 2 of Figure 4.1(b), and, if originated in the upstream source, are *reflected* back to it. In addition, for curves of type 2, with two local extrema, there is region of *doubly-trapped* electrons, bouncing between two locations of the divergent side: they are decelerated axially by ϕ when moving downstream, and by B when moving upstream. The populations of reflected plus doubly-trapped electrons constitute the *confined* electron population.

As boundary conditions for the VDFs, it is assumed that there are no sources of particles at the downstream end, $\zeta = +\infty$, while, at the upstream plasma reservoir,

the forward marching VDFs (i.e. with $w_\parallel > 0$ and named f^+) of ions and electrons are known and semi-Maxwellian (except for a monoenergetic case discussed in Sec III), that is

$$f_0^+(E) = n_\star \left(\frac{m}{2\pi T_\star}\right)^{3/2} \exp\left(-\frac{E}{T_\star}\right), \tag{4.7}$$

with $n_\star$ and $T_\star$ reference values of density and temperature. The backward-marching side of each VDF for reflected particles, named f^-, is to be determined.

Macroscopic magnitudes of ions and electrons are obtained from the velocity-integral moments of their VDF. Integration is more conveniently carried out in the invariants space (E, μ), so that for any magnitude χ its velocity integral becomes

$$\langle\chi\rangle(\zeta) = \frac{2\pi B}{m^2} \int\int d\mu dE \frac{\chi f(E,\mu)}{|w_\parallel(\zeta,\mu,E)|}. \tag{4.8}$$

Since doubly-trapped electrons are disconnected from both the upstream and downstream ends, in this stationary, collisionless model, their VDF can only be postulated. Here, following Ref. [83], the VDF expression for the reflected electrons will be also used for doubly-trapped electrons, which means a full replenishment of the doubly-trapped region during the transient MN formation.

The main macroscopic magnitudes for each species are density, particle (parallel) flux, parallel pressure, perpendicular pressure, (parallel) heat fluxes of parallel and perpendicular energy, given, respectively, by

$$n \equiv \langle 1\rangle, \qquad nu = \langle w_\parallel\rangle, \tag{4.9}$$

$$p_\parallel = nT_\parallel = m\langle c_\parallel^2\rangle, \qquad p_\perp = nT_\perp = m\langle w_\perp^2\rangle/2, \tag{4.10}$$

$$q_\parallel = \frac{m}{2}\langle c_\parallel^3\rangle = \frac{m}{2}\langle w_\parallel^3\rangle - \frac{m}{2}nu^3 - \frac{3}{2}p_\parallel u, \tag{4.11}$$

$$q_\perp = \frac{m}{2}\langle w_\perp^2 c_\parallel\rangle = \frac{m}{2}\langle w_\perp^2 w_\parallel\rangle - p_\perp u. \tag{4.12}$$

Here, species subscripts are dropped, u is the (axial) macroscopic velocity of the species, $c_\parallel = w_\parallel - u$ is the diffusion velocity of each species, and $T_\parallel$ and $T_\perp$ are

parallel and perpendicular temperatures. The average pressure is defined as $p = (p_\parallel + 2p_\perp)/3$ and similarly for the average temperature. The parallel heat flux of total energy is $q = q_\parallel + q_\perp$. Notice that: the heat fluxes are indeed diffusive fluxes of thermal energy while the convective fluxes of parallel and perpendicular thermal energy are $(3/2)p_\parallel u$ and $p_\perp u$; only free subpopulations contribute to parallel fluxes of particles and energy; and, in this paraxial model, focused in the MN centerline all perpendicular fluxes are zero, i.e. $\langle w_\perp \rangle = \langle w_\perp^3 \rangle = \langle c_\parallel^2 w_\perp \rangle = 0$.

Using equation (4.8) with $\langle w_\parallel \rangle$ the particle flows are straightforwardly determined:

$$\frac{nu}{B} = \frac{n_\star}{\sqrt{2\pi m} T_\star^{3/2}} \int_{E_0}^{\infty} dE \mu_T(E) \exp\left(-\frac{E}{T_\star}\right) \tag{4.13}$$

with $E_0 = 0$ for ions and to $E_0 = -e\phi_\infty$ for electrons. These flows are constant spatially, which implies that $1/B$ is proportional to the effective cross-section area of the flow.

For the density profiles, taking into account that $f_i^- = 0$ for free ions and $f_i^- = f_i^+$ for reflected ions, the ion density satisfies

$$n_i(B,\phi) = \frac{n_{i\star}}{\sqrt{\pi} T_{i\star}^{3/2}} \int_0^{\infty} \exp\left(-\frac{E}{T_{i\star}}\right) \left(\sqrt{E - e\phi} + \text{sign}[\zeta_{iT}(E) - \zeta]\sqrt{E - e\phi - B\mu_{iT}(E)}\right) dE. \tag{4.14}$$

Similarly, for electrons one has[83]

$$n_e(B,\phi) = \frac{n_{e\star}}{\sqrt{\pi} T_{e\star}^{3/2}} \int_{-e\phi_\infty}^{\infty} \text{sign}[\zeta_{eT}(E) - \zeta] \exp\left(-\frac{E}{T_{e\star}}\right) \sqrt{E + e\phi - B\mu_{eT}(E)} dE + n_{e\star} \exp\frac{e\phi_\infty}{T_{e\star}} \left(\frac{1 + \text{erf}\sqrt{\xi}}{2} \text{e}^{\xi} - \sqrt{\frac{\xi}{\pi}}\right) \tag{4.15}$$

with, in the last term, $\xi(\phi) = e(\phi - \phi_\infty)/T_{e\star}$. Taking the limit $\zeta \to -\infty$ (i.e. $B \to 0$) in these expressions, the upstream densities correspond indeed to the reference values:

$$n_{i0} = n_{i*}, \qquad n_{e0} = n_{e*}.$$

It will later be found that $T_{i0} = T_{i*}$ and $T_{e0} = T_{e*}$ too. This means that, at $\zeta = -\infty$, the back-marching VDFs of ions and electrons are practically semi-Maxwellian. In

other words, at $\zeta \to -\infty$, the contribution of the free populations of ions and electrons is a set of measure zero on the velocity integral moments.

Hereafter, only the case of a current-free plasma beam is discussed, i.e. equal fluxes of ions and electrons in the MN. Then, the total potential drop $|\phi_\infty|$ and the profile of the ambipolar electric potential profile $\phi(\zeta)$ must be such that the plasma beam satisfies the current-free and quasineutrality conditions,

$$e(n_i u_i - n_e u_e) = 0, \qquad n_i(B,\phi) \simeq n_e(B,\phi) \equiv n. \tag{4.16}$$

The iteration procedure on $\phi(\zeta)$ to fulfill the above conditions and obtain the self-consistent solution of the problem is the same than in Ref. [83]. Notice that equations (4.16) states that in a paraxial current-free plasma $u_e = u_i$. The extension of the model to a current-carrying plasma is straightforward, just requiring to change one boundary condition.

Plasma equations are normalized with B_M, n_0, T_{e0}, and $\sqrt{T_{e0}/m_i}$. Then, the dimensionless model turns out to depend only on two parameters: the ion-to-electron temperature ratio and the ion-to-electron mass ratio, T_{i0}/T_{e0} and m_i/m_e.

4.3 Kinetic results

4.3.1 Spatial profiles and influence of the ion VDF form

Reference [83] studied the MN model with Maxwellian electrons and monoenergetic ions with

$$f_{i0}^{+}(E) = \frac{n_{i0} m_i^{3/2}}{4\pi (3T_{i0})^{1/2}} \delta\left(E - \frac{3}{2} T_{i0}\right), \tag{4.17}$$

with δ the Dirac function. Figure 4.2 compares the plasma expansion along the nozzle for the monoenergetic and Maxwellian ion VDFs. Figure 4.2(a) shows that the electric potential profiles $\phi(\zeta)$ are practically the same for both ion VDFs. This indicates that $\phi(\zeta)$ does not depend practically on the velocity dispersion of the ion VDF, which makes sense since it is determined from conditions (4.16) involving only plasma densities and flows. Section 4.3.3 will further compare electric potential drops for the two ion VDFs.

Next, since the electron response depends totally on the relation $\phi(B)$, which is nearly the same for the two ion VDFs, *all* electron macroscopic magnitudes are

almost identical for both distributions, as Figure 4.2(b), (c), (f), and (i) corroborate. Since ions and electrons share density and axial velocity, n and u_i, differences on macroscopic variables between the two ion VDFs are noticeable only for higher velocity moments, such as ion temperatures and heat fluxes. This is well illustrated in Figure 4.2(d), (e), (g), and (h).

Differences in $T_{i\parallel}$ are seen only in the divergent region. Downstream, $T_{i\parallel}$ goes to zero only for the monoenergetic distribution, while a reduced parallel velocity dispersion is kept for the Maxwellian one, i.e. $T_{i\parallel\infty} \neq 0$. On the contrary, $T_{i\perp}$ is the same for both distributions and goes to zero downstream ($T_{i\perp\infty} = 0$) due to the inverse magnetic mirror effect, as it will be discussed later. Whereas ions develop a significant temperature anisotropy along the MN, the electron temperature is practically isotropic except far downstream. Ion and electron heat fluxes present complex behaviors that will be discussed in Section IV. Finally, the qualitative trends shown in Figure 4.2 for the hot-ion case continue to be valid in the cold-ion case, i.e. for $T_{i0}/T_{e0} \ll 1$. Some parametric studies on the influence of T_{i0}/T_{e0} and m_i/m_e on the solution are developed below.

4.3.2 Behavior on the convergent region and the MN throat

The magnetic mirror effect (MME) on both ions and electrons makes the plasma response very different in the convergent side, where it slows down the parallel motion of individual ions and electrons, and the divergent side, where it accelerates axially ions and electrons. When this behavior is combined with the effect of the electric potential, $\phi(\zeta)$, which is similar in both nozzle sides but opposite for ions and electrons, it turns out that the collective MME is very different for ions and electrons.

Figure 4.3 plots the main plasma properties at the magnetic throat M. Figure 4.3(a) shows that the potential fall in the convergent side scales mainly with the electron temperature and lies within the interval

$$-e\phi_M/T_{e0} \sim 0.55 - 0.70, \tag{4.18}$$

if $m_i/m_e > 10^3$ (that is for ion-electron plasmas). Figure 4.3(b) shows that the fraction of free electrons at the MN throat (and therefore in the convergent MN)

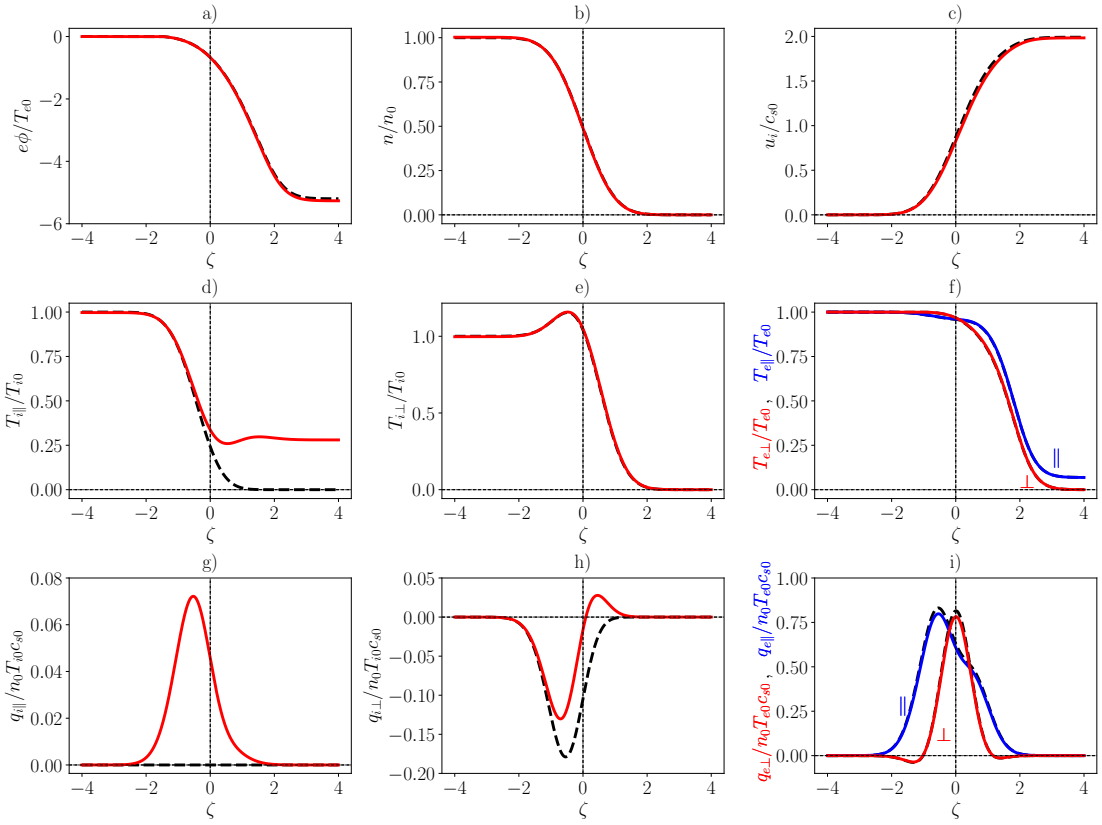

Figure 4.2: Normalized plasma properties for Maxwellian (——— and ———) and monoenergetic (- - -) ions, with $m_i/m_e = 10^4$ and $T_{i0}/T_{e0} = 10$.

is still very small. The increase of that fraction when m_i/m_e decreases is due to a lower electrostatic confinement of electrons, caused by a lower $|\phi_\infty|$. Figure 4.3(c) plots the plasma density at M, which follows approximately the Boltzmann relation, $n_M/n_\star \simeq \exp(e\phi_M/T_{e0}) \sim 0.50 - 0.54$; the next Section will explain this behavior. Figure 4.3(d) plots the ratio of the plasma velocity versus the *reference* sound speed at the throat, $c_{sM} = \sqrt{(T_{eM} + T_{iM})/m_i}$. Notice that the plasma here is a collisionless fluid, and an expression for the real sound speed would require an exact closure of the fluid equations, which the next Section finds unavailable. Nonetheless, it is still reasonable to say that the plasma beam experiences a sonic transition around the nozzle throat.

Figure 4.3(e) and Figure 4.3(f) show the parallel and perpendicular temperatures of ions and electrons at M. While electrons remain practically isothermal in the convergent MN, ion temperature components behave differently and develop an

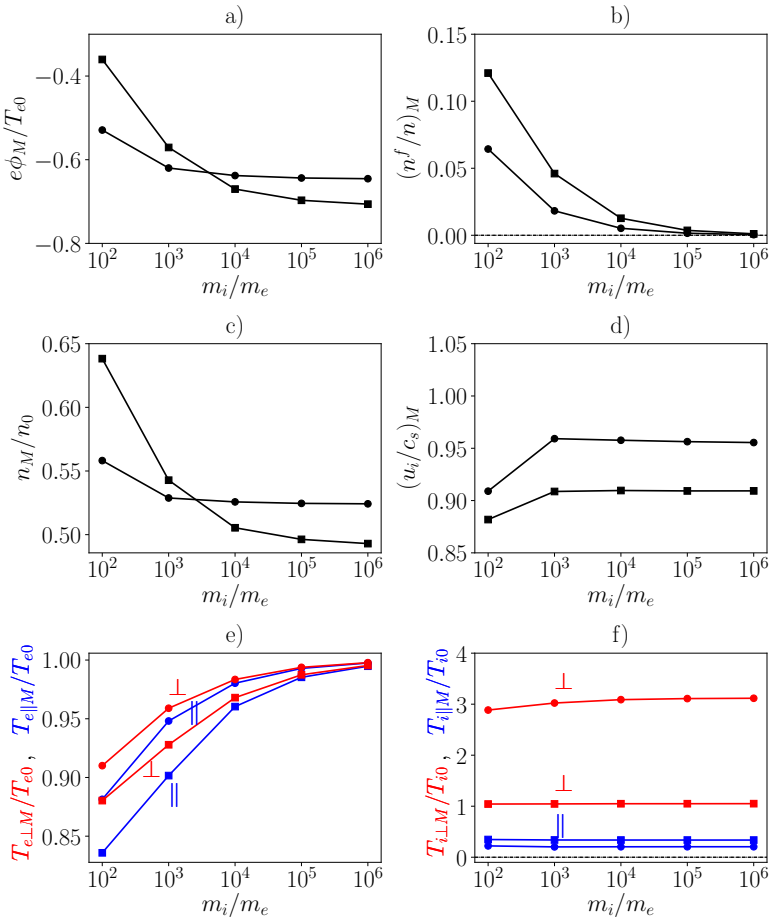

Figure 4.3: Normalized plasma properties at the magnetic throat M, for different m_i/m_e and $T_{i0}/T_{e0} = 0.1$ (—●—) and 10 (—■—). (a) Plasma potential, (b) free electron density, (c) plasma density, (d) ion velocity, (e) electron temperatures, and (f) ion temperatures.

anisotropy. In fact, although $T_{i\parallel}$ decreases similarly for both hot- and cold-ion simulations ($T_{i\parallel} \simeq 0.2T_{i0}$ and $T_{i\parallel} \simeq 0.33T_{i0}$ for cold- and hot-ion cases, respectively), $T_{i\perp}$ increases at the throat. This increase is related to the existence of a low-velocity empty region in the ion VDF at the throat, of characteristic energy $|e\phi_M| \sim T_{e0}$, as discussed in the Appendix 4.5. This empty region becomes more relevant in the integral for $T_{i\perp}$ the lower the characteristic ion energy T_{i0}. Therefore, the temperature anisotropy in the ion population is more marked in the case of initially cold ions, $T_{i0}/T_{e0} \ll 1$.

Both ion and electron particles suffer a similar a magnetic mirror effect, reducing the parallel particle velocity and reflecting back particles with $w_\parallel = 0$. However,

the *collective* MME is very different in the two VDFs populations, due to the different effect of the electric potential on the two species: additional confinement of electrons and parallel acceleration for ions. It is shown later that that the collective MME on a given species appears as the volumetric force $n(T_\perp - T_\parallel) d\ln B/dz$ in its momentum equation, so a collective MME is closely related to the development of temperature anisotropy. Therefore, Figure 4.3(e) and (f) suggest the existence of a strong collective MME on the ions but a negligible one on the electrons. For electrons the individual magnetic mirror plus the electric potential make the VDF to decrease its density along the convergent MN, while remaining nearly Maxwellian and isotropic. Appendix A discusses and plots the evolution of the ion and electron VDFs on the convergent MN, in order to better understand their collective behaviors.

Several works on kinetic models consider the plasma expansion in a divergent MN only, placing the plasma source at the throat M (or nearby) [26, 110]. This configuration makes full sense when plasma processes on the convergent MN are dominated by phenomena different from magnetic guiding, such as plasma production and heating or interaction with chamber walls.

The plasma conditions imposed at the throat in these models generally differ partially with the present ones, for instance on the ion temperature anisotropy and the beam 'near-sonic' macroscopic velocity. This fact must be taken into account for a proper comparison with the present model.

4.3.3 Parametric laws for the total potential fall

The asymptotic downstream values of plasma magnitudes are important variables characterizing the plasma response in the MN. They depend on the two free parameters of the model: the mass ratio, m_i/m_e, which defines the propellant type; and the temperature ratio T_{i0}/T_{e0}, which species stores more internal energy upstream.

The main downstream variable is surely the total electric potential fall in the convergent-divergent MN, plotted in Figure 4.4(a). The dimensionless final potential, $e|\phi_\infty|/T_{e0}$, increases logarithmically with the mass ratio. For electron-ion plasmas -i.e. $m_i/m_e \geq O(10^3)$-, the potential fall (including the drop in the convergent MN) is 5-8 times the upstream electron temperature, which agrees reasonably well with experimental data, taking into account the differences between this model

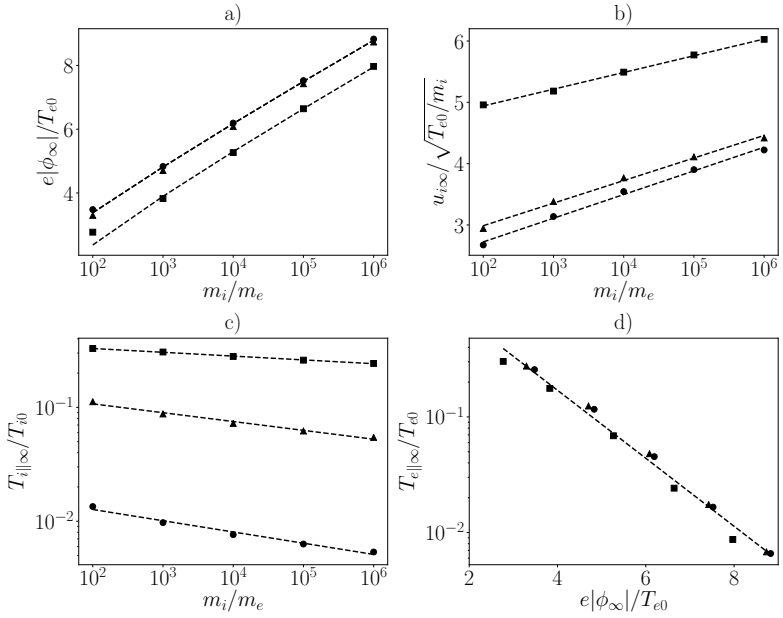

Figure 4.4: (a) Total dimensionless potential drop versus the mass ratio, (b) plasma beam velocity versus the mass ratio, (c) downstream parallel ion temperature versus the mass ratio and (d) downstream parallel electron temperature versos the total potential drop. $T_{i0}/T_{e0} = 0.1$ ($\bullet$), $T_{i0}/T_{e0} = 1.0$ ($\blacktriangle$) and $T_{i0}/T_{e0} = 10$ ($\blacksquare$); the dashed lines correspond to approximate fitting laws.

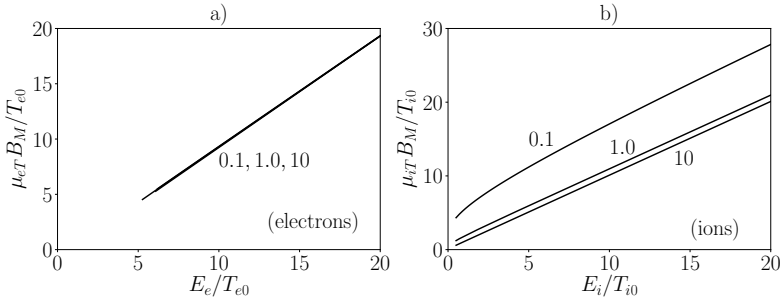

Figure 4.5: Functions $\mu_T(E)$ for ions and electrons, $T_{i0}/T_{e0} = 0.1, 1.0$ and 10. Plots are for $m_i/m_e = 10^4$ but $\mu_{iT}(E)$ and $\mu_{eT}(E)$ are practically independent of m_i/m_e.

and practical configurations [74, 42]. The dimensionless final potential depends weakly on the temperature ratio: it almost does not change from T_{i0}/T_{e0} =0.1 to 1, and only by a 15-20% percent from T_{i0}/T_{e0} =1 to 10. This implies that $|\phi_\infty|$ is set mainly by the electron thermal energy and is consistent with the role of ϕ of confining most of the electron population. Approximate semi-analytical fittings for

$e|\phi_\infty|/T_{e0}$ versus m_i/m_e and T_{i0}/T_{e0} are derived below.

Figure 4.4(b) plots the plasma beam velocity, For the cold-ion case $T_{i0}/T_{e0} = 0.1$, the numerical linear fitting is

$$\frac{u_{i\infty}}{\sqrt{T_{e0}/m_i}} \approx 0.168 \ln \frac{m_i}{m_e} + 1.95, \tag{4.19}$$

and the two coefficients in this linear fitting become (0.160, 2.25) and (0.118,4.40) for $T_{i0}/T_{e0} = 1$ and 10, respectively. In the cold-ion case, one has $u_{i\infty} \approx \sqrt{2e|\phi_\infty|/m_i}$, while a relevant contribution from the conversion of ion thermal energy into kinetic energy is added in the hot-ion cases. In plasma thrusters, the final beam velocity is closely related to the specific impulse, I_{sp}. In this respect it is interesting to observe that, to dominant order, $u_{i\infty} \propto \sqrt{m_e/m_i}\ln(m_i/m_e)$, so that the heavier the propellant is, the larger electric potential fall compensates partially the higher ion-mass penalty in I_{sp}.

Since $u_{i\infty}$ is finite, the continuity equation (4.13) states that the plasma density goes to zero as $n \propto B^{-1}$. The perpendicular temperatures of ions and electrons also go to zero, i.e. $T_{i\perp\infty} = T_{e\perp\infty} = 0$, due to the conservation of the magnetic moment (i.e. the inverse magnetic mirror effect). However, the parallel velocities of ions and electrons keep part of their upstream dispersion and the respective downstream parallel temperatures of ions and electrons are not zero. Figure 4.4(c) plots $T_{i\parallel\infty}/T_{i0}$. For the cold-ion case $T_{i0}/T_{e0} = 0.1$, the numerical linear fitting is

$$\frac{T_{i\parallel\infty}}{T_{i0}} \approx -0.099 \ln \frac{m_i}{m_e} - 3.91 \tag{4.20}$$

The two coefficients in this linear fitting become $(-0.077, -1.87)$ and $(-0.033, -0.96)$ for $T_{i0}/T_{e0} = 1$ and 10, respectively. Figure 4.4(d) shows that the dependence of $T_{e\parallel\infty}/T_{e0}$ on the mass and temperature ratios is through the final electric potential fall, via the numerical linear fitting

$$\ln \frac{T_{e\parallel\infty}}{T_{e0}} = -0.67 \frac{e|\phi_\infty|}{T_{e0}} + 0.89. \tag{4.21}$$

Both final parallel temperature ratios are much less than one and they are lower the higher m_i/m_e and, thus $e|\phi_\infty|/T_{e0}$) are. It can also be concluded that the final electric potential depends more on the electron state than on the ion one.

Next, Figure 4.5 presents $\mu_T(E)$ for ions and electrons for the parametric ranges $m_i/m_e = 10^2$–10^5 and $T_{i0}/T_{e0} = 0.1$–10. As Ref. [83] showed and Figure 4.5(a)

illustrates, the electron function $\mu_{eT}(E)$ is practically independent of the two dimensionless parameters and satisfies rather accurately the linear relation

$$\mu_{eT}(E) \approx E/B_M. \tag{4.22}$$

For Maxwellian ions, Figure 4.5(b) shows that $\mu_{iT}(E)$ is independent of the mass ratio, but depends on T_{i0}/T_{e0}. Only for the hot-ion case the approximation $\mu_{iT}(E) \approx E/B_M$ is applicable. Using these linear approximations for $\mu_{eT}(E)$ and $\mu_{iT}(E)$, analytical expressions are found for the flows of electrons and hot ions in equation (4.13). For mass ratios above $O(10^2)$ and Maxwellian VDFs, these are

$$\frac{nu_e}{B} \simeq \frac{n_{e0}}{B_M}\sqrt{\frac{T_{e0}}{2\pi m_e}}\left(\frac{e|\phi_\infty|}{T_{e0}}+1\right)\exp\left(-\frac{e|\phi_\infty|}{T_{e0}}\right), \tag{4.23}$$

and

$$\frac{nu_i}{B} \simeq \frac{n_{i0}}{B_M}\sqrt{\frac{T_{i0}}{2\pi m_i}} \simeq 0.40\frac{n_{i0}}{B_M}\sqrt{\frac{T_{i0}}{m_i}} \quad \left(\text{for } \frac{T_{i0}}{T_{e0}} \gg 1\right). \tag{4.24}$$

Equating both flows, the total potential fall satisfies the implicit equation

$$\frac{e|\phi_\infty|}{T_{e0}} - \ln\left(1+\frac{e|\phi_\infty|}{T_{e0}}\right) = \ln\sqrt{\frac{m_i T_{e0}}{m_e T_{i0}}} - 0.2, \quad \text{for} \quad \frac{m_i}{m_e} \gg \frac{T_{i0}}{T_{e0}} \gg 1, \tag{4.25}$$

where the offset -0.2 has been added from the linear numerical fitting plotted in Figure 4.4(a). Notice that the second term on the left side of equation (4.25) provides just a mild correction to the first one.

For the cold-ion case, no simple-enough expression for $\mu_{iT}(E)$ has been obtained, but it is found that the dimensionless potential fall depends no more on T_{i0}. A suitable numerical fitting based on the results of Figure 4.4(a) is

$$\frac{e|\phi_\infty|}{T_{e0}} - \ln\left(1+\frac{e|\phi_\infty|}{T_{e0}}\right) = \ln\sqrt{\frac{m_i}{m_e}} - 0.4, \quad \text{for} \quad \frac{T_{i0}}{T_{e0}} \ll 1. \tag{4.26}$$

These two fittings of the MN potential fall for the cold- and hot-ion cases match at $T_{i0}/T_{e0} \approx 1.5$.

Figure 4.2(a) showed that $|\phi_\infty|$ was very similar for Maxwellian and monoenergetic ion VDFs, for same mass and temperature ratio. Indeed, for a monoenergetic and hot-ion VDF, equation (4.17), the ion flow satisfies

$$\frac{nu_i}{B} \simeq \frac{n_{i0}}{B_M}\sqrt{\frac{3T_{i0}}{16m_i}} \simeq 0.43\frac{n_{i0}}{B_M}\sqrt{\frac{T_{i0}}{m_i}}, \quad \text{for} \quad \frac{m_i}{m_e} \gg \frac{T_{i0}}{T_{e0}} \gg 1,$$

which differs very little from equation (4.24) for a Maxwellian VDF, thus justifying the previous observation.

Figure 4.3(a) and equation (4.18) showed that the potential drop in the convergent MN is modest compared to the total potential drop in the MN. Hence, the above scaling laws for $e|\phi_\infty|/T_{e0}$ can then be taken as valid approximations for the potential fall in the divergent nozzle, $e\phi_{\infty M}/T_{e0}$, with $\phi_{\infty M} = \phi_M - \phi_\infty$. Then, the logarithmic dependence of $e\phi_{\infty M}/T_{e0}$ on m_i/m_e resembles much the one for the potential fall in a conventional Debye sheath next to a wall. In this respect, it is worth to compare the model for the magnetic cusp (indeed a convergent MN) studied by Martínez-Sánchez and Ahedo[82] to the present convergent-divergent MN one. In their case the plasma was current-free too, and the convergent MN was followed by a Debye sheath (of zero thickness and non-neutral) and a solid wall located at the MN throat, while here the convergent MN is followed by the divergent MN (of infinite extension and quasineutral).

The total potential fall within their sheath and the one within the present divergent MN have indeed the same role: to confine appropriately most of the electrons in order that the electron current leaking downstream is the correct one (i.e. equal to the ion current for a current-free beam). Electron and ion physics are shown here to be more complex in the divergent MN than in the planar, purely-electrostatic sheath, but the required potential drops for electron confinement are rather similar.

Figure 4.2 showed that most plasma magnitudes reach their downstream asymptotic values around $\zeta \sim 2$, that is $B/B_M \sim 0.01$. Thus, the downstream law is discussed in this subsection are strictly valid only if the plasma continues to be fully-magnetized at $\zeta \sim 2$, which is unlikely (mainly for ions) in many practical cases. Ion and, then, electron demagnetization at an earlier stage of the expansion will certainly modify somehow the plasma response, but collective changes could be rather limited. This judgement is supported by the comparison of the present MN model with the (collisionless, paraxial) unmagnetized plume model by Merino et al. [95] where plasma anisotropic cooling and similar parametric laws for $e|\phi_\infty|/T_{e0}$ are found too.

4.4 Macroscopic plasma description

4.4.1 The equivalent fluid model

Taking velocity moments of the Vlasov equation for a generic VDF, the fluid equations for the bulk variables are obtained. For the present paraxial flow, the main fluid equations for each species are

$$\frac{nu}{B} = \text{const}, \tag{4.27}$$

$$B\frac{d}{d\zeta}\left(\frac{mnu^2}{B}\right) + nZe\frac{d\phi}{d\zeta} + \frac{dp_\parallel}{d\zeta} - (p_\parallel - p_\perp)\frac{d\ln B}{d\zeta} = 0, \tag{4.28}$$

$$\frac{nuZe\phi}{B} + \frac{nu}{B}\left[\frac{mu^2}{2} + \frac{3T_\parallel}{2} + T_\perp\right] + \frac{q_\parallel + q_\perp}{B} = \text{const}, \tag{4.29}$$

$$\frac{nuT_\perp + q_\perp}{B^2} = \text{const}, \tag{4.30}$$

corresponding to the conservation of particles, momentum, total energy, and perpendicular energy, respectively. The constant in the continuity equation was already determined in equation (4.13). The momentum equation (4.28), which cannot be reduced to a first integral, shows $1/B$ as the effective cross-section variation in the convective term, and includes the collective MME as a third volumetric force. The total energy conservation equation (4.29) includes the contributions of the kinetic and thermal energy flows plus the *parallel* heat flows of parallel and perpendicular energies, plus the 'flow of potential energy' (indeed, the integral of the work of the electric field). Dividing this equation by equation (4.27), the conservation of total energy 'per particle' in the ion or electron flow is

$$\frac{mu^2}{2} + \frac{3T_\parallel}{2} + T_\perp + \frac{q_\parallel + q_\perp}{nu} + Ze\phi = \mathcal{E}, \tag{4.31}$$

with $\mathcal{E}$ the total energy per (average) particle. Finally, the very simple form of the perpendicular energy equation (4.30), without kinetic energy flow and electric field work, is due to the paraxial approximation (i.e. it is the perpendicular energy in the centerline). The factor $1/B^2$ in this equation combines the effect of the cross-section variation and the magnetic mirror effect (which increases the perpendicular kinetic energy proportionally to B).

Since these fluid equations are *exact* moments of the Vlasov equation they must be satisfied by the integral velocity moments of the ion and electron VDFs obtained

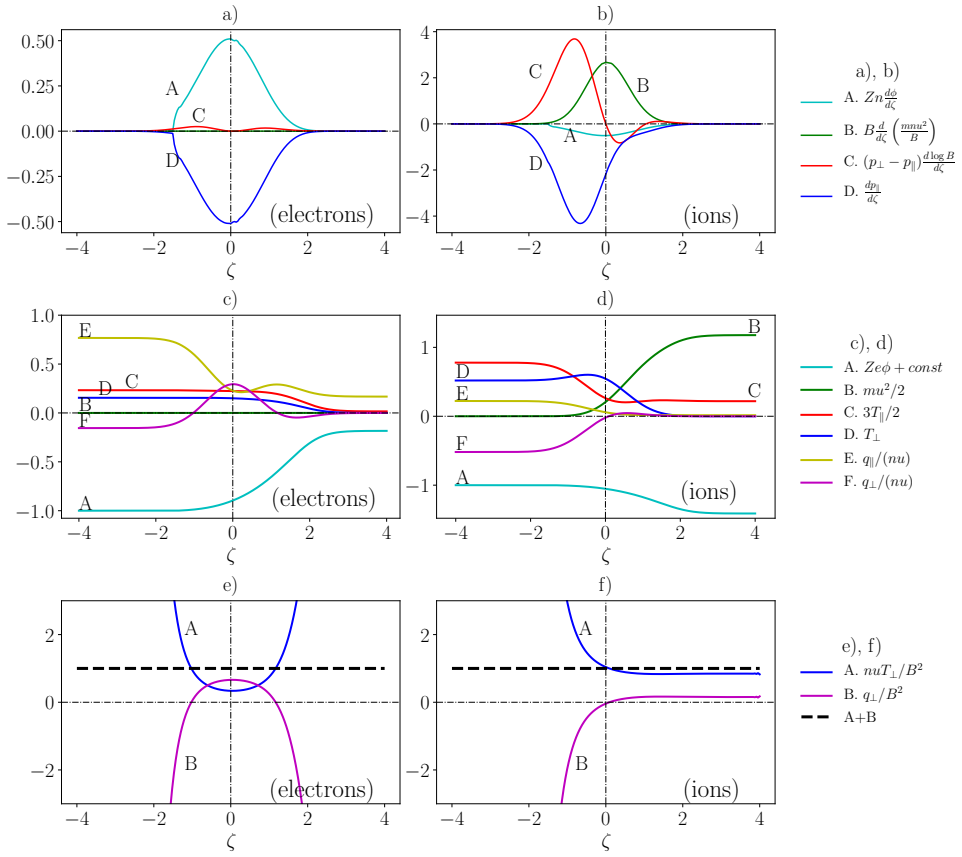

Figure 4.6: Relative contribution for electrons (left) and hot ions (right) of the different terms of the fluid equations of (a)-(b) momentum, (c)-(d) total energy per particle, and (e)-(f) perpendicular energy. Units in vertical axes are arbitrary. Results are for $m_i/m_e = 10^4$ and $T_{i0}/T_{e0} = 10$.

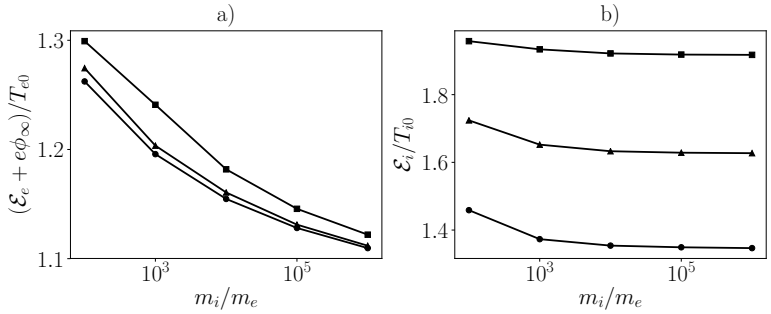

Figure 4.7: (a) $\mathcal{E}_e$ and (b) $\mathcal{E}_i$ of (4.31) as a function of m_i/m_e for three values of $T_{i0}/T_{e0} = 0.1$ (—●—), $T_{i0}/T_{e0} = 1$ (—▲—) and $T_{i0}/T_{e0} = 10$ (—■—).

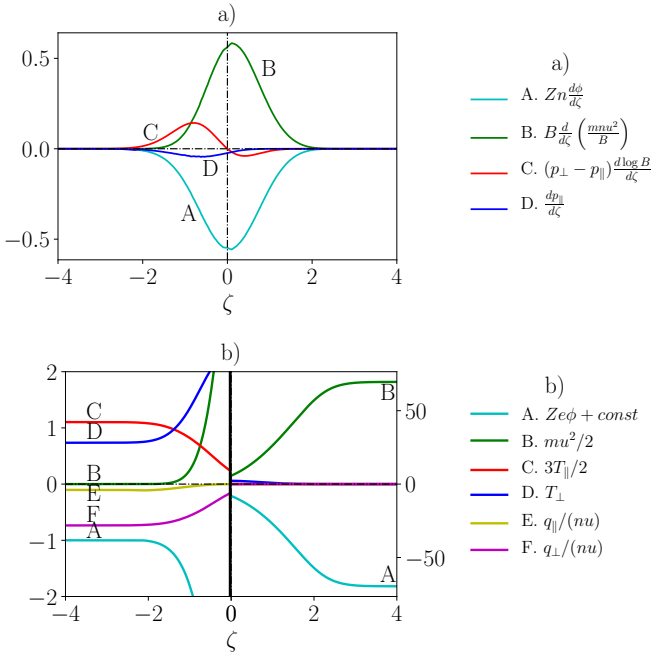

Figure 4.8: Relative contribution of the different terms to the equations for (a) momentum (4.28), and (b) total energy (4.29) for the cold-ion case. Units in vertical axes are arbitrary. Results are for $m_i/m_e = 10^4$ and $T_{i0}/T_{e0} = 0.1$.

directly from the kinetic model. In fact the error in fulfilling these fluid equations measures the error of the numerical integration algorithms; in all cases presented here it has been checked that this error is negligible. The analysis of the fluid terms for $m_i/m_e = 10^4$ and $T_{i0}/T_{e0} = 10$ is presented in Figure 4.6 for electrons (left) and ions (right). Each subplot depicts the different terms of the momentum, the total energy, and the perpendicular energy equations for ions and electrons along the nozzle, thus illustrating the dominant terms in each equation and nozzle region. Concerning plots 4.6(c)-(d), equation (4.31) has been used and the constant on its right-hand side has been included into the potential energy term. This is not possible in plots 4.6(e)-(f) for the flows of perpendicular energy, but units have been set in order that the right-side constant in equation (4.30) is equal to 1.

Starting with electrons and their momentum equation, Figure 4.6(a) shows that inertia terms are negligible, as expected. The collective MME turns out to be marginal *in the whole MN*, due to the small temperature anisotropy except at the far-downstream end. Therefore, electrons present everywhere a near perfect balance

between the electrostatic force and the pressure gradient,

$$en\frac{d\phi}{d\zeta} \simeq \frac{dp_e}{d\zeta}. \tag{4.32}$$

Furthermore, in the convergent part of the MN, since T_e is almost constant, and equation (4.32) becomes the Boltzmann relation. This is not the case in the the divergent MN, where no simple relation among T_e, n, and ϕ have been found.

Regarding the conserved electron energy $\mathcal{E}_e$, Figure 4.7(a) plots its dependence with m_i/m_e and T_{i0}/T_{e0}. Interestingly $\mathcal{E}_e + e\phi_\infty$ is almost universal and close to $(1.2 \pm 0.1)T_{e0}$. Once more it is worth to compare this result to the case of a conventional Debye sheath where $\mathcal{E}_e + e\phi_\infty \simeq 2T_{e0}$. Figure 4.6(c) plots the different contributions to the electron energy balance: the kinetic electron energy is negligible and the potential energy flow is the dominant contribution, which is balanced by the thermal and heat flows, with the dominance of the heat flow of parallel energy. Figure 4.6(e) shows that $q_{e\perp}$ and $T_{e\perp}nu_e$ near-balance each other except in the central region of the MN. Since the electron temperature is nearly-isotropic except in the cold downstream end, a good approximation for the electron energy balance is

$$\frac{5}{2}T_e + \frac{q_e}{nu_e} - e\phi \simeq \mathcal{E}_e, \tag{4.33}$$

with $q_e = q_{e\parallel} + q_{e\perp}$. The error in using this approximate law, in the wide parameter range considered, is found to be below 7% in the whole MN. Regarding the dependence on B, the asymptotic analysis of Ramos *et al.* [106] for the electron population at the downstream end of the nozzle, yielded $nT_{e\parallel}u \propto B$ and $nT_{e\perp}u \propto B^{5/3}$, which is confirmed here. Additionally, it is found here that similar scaling laws apply to the parallel and perpendicular heat fluxes: $q_{e\parallel} \propto B$ and $q_{e\perp} \propto B^{5/3}$. Next Subsection further analyzes electron heat fluxes.

The behavior of the hot ion population, shown on the right plots of Fig. 4.6, presents interesting differences with respect to the electron one. In Fig. 4.6(b) for the ion momentum equation, the electrostatic force is found to be marginal for hot ions (except for a discrete contribution in the divergent region). The momentum flux gain is provided mainly by the two pressure terms; in particular, the macroscopic MME is a dominant contribution in the whole MN. Also, far upstream, the magnetic mirror and the parallel pressure gradient are seen to develop sooner than ion convection. Figure 4.6(d) and (f) for the ion energy show that: the kinetic

energy of ions comes mainly from the electric potential energy and the parallel thermal energy; the heat flux of parallel ion energy can be considered a second-order contribution; and the total flux of perpendicular energy $q_{i\perp} + nu_i T_{i\perp}$ tends to zero at both nozzle ends but is non negligible in the central region of the MN. In the cold-ion case, the response of the electrons is practically the same, but the ion response is simpler, as shown in Figure 4.8. Now, the ion kinetic and electrostatic energies dominate totally the ion response. Figure 4.7(b) plots $\mathcal{E}_i$. There is not a good-enough approximate expression, similar to equation (4.33), for the ion energy. The equation

$$\frac{1}{2}m_i u_i^2 + \frac{3}{2}T_{i\parallel} + T_{i\perp} + e\phi \approx \mathcal{E}_i. \tag{4.34}$$

yields an error of up to 10% in the central region of the nozzle and remains below 2% for both hot- and cold-ion cases along the divergent region of the expansion. Nonetheless, equation (4.34) is not valid far upstream (where relative errors are of order one).

4.4.2 Electron heat fluxes

Using the preceding fluid equations directly, i.e. without solving the kinetic Vlasov equation, requires closure relations for the heat fluxes. Clearly, the CGL double adiabatic limit, $q_\parallel = q_\perp = 0$[35], does not apply. Still, ion heat fluxes are not a dominant contribution to the energy balance and could be ignored in a first approach, as in equation (4.34). This is not the case for the electron heat fluxes, which are further investigated in this subsection.

First, electron heat fluxes do not follow a Fourier law, as it evident from Fig. 4.9, which compares the shapes of the heat fluxes and the temperature gradients and shows that they are not proportional. Furthermore, the upstream and downstream electron heat fluxes satisfy

$$\zeta = -\infty : \quad \frac{q_{e\perp}}{nu_e} = -T_{e0}, \quad \frac{q_{e\parallel}}{nu_e} = \frac{3}{2}T_{e0} + e|\phi_\infty|, \tag{4.35}$$

$$\zeta \to +\infty : \quad \frac{q_{e\perp}}{nu_e} = 0, \quad \frac{q_{e\parallel}}{nu_e} \simeq \mathcal{E}_e \approx 1.2T_{e0}, \tag{4.36}$$

so they are nonzero, in general, while the temperature gradients become null at the two MN ends. These facts indicate that a heat flux in collisionless and collisional

fluids does not represent the same physics. In both fluids, the heat flux is the difference between the total and convective fluxes of total energy, Eqs. (4.11) and (4.12). In a collisional fluid, the heat flux has the simple and clear meaning expressed by the Fourier law: it develops when a temperature gradient exists and its effect is to reduce that gradient. No such meaning and effect extend to a collisionless fluid, where the heat flux is principally a mathematical entity. A physical meaning can theoretically be extracted from the third-order equations in the fluid hierarchy for the transport of $q_{e\parallel}$ and $q_{e\perp}$; see, for instance, Eqs. (43) and (44) of Ref. [107]. However, the complexity of these equations and the presence of next-order terms make uncertain they can unveil a clear physical interpretation of these fluxes.

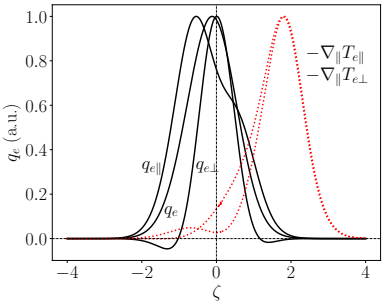

Figure 4.9: Normalized evolution of electron heat fluxes and gradients of temperatures along the nozzle for $m_i/m_e = 10^4$, and $T_{i0}/T_{e0} = 10$.

Instead, in order to understand better the relevance here of the heat fluxes (i.e. the diffusive fluxes of thermal energy), Figs. 4.10(a)-(d) compare them with the convective thermal fluxes. First, Fig. 4.10(a) shows that the total flux of perpendicular energy, $q_{e\perp} + nu_eT_{e\perp}$, is positive all along the MN and tends to zero at both nozzle ends, although only at the downstream end both individual contributions are zero. The negative value of $q_{e\perp}$ at the two asymptotic regions is a good example of its predominantly mathematical character. In the central region of the MN, the total flux of perpendicular energy increases as a consequence of the individual magnetic mirror effect on electrons; as a consequence $q_{e\perp}$ increases (and changes sign). Next, Fig. 4.10(b) compares the two parallel energy fluxes, both being positive along the whole MN. As commented above, the heat flux is about 2.5-4 times the convective flux in the convergent MN in spite of the quasi-constant temperature there. Then, just downstream of the nozzle throat, there is a minimum of the diffusion-to-convection ratio, which balances the magnetic mirror effect on the

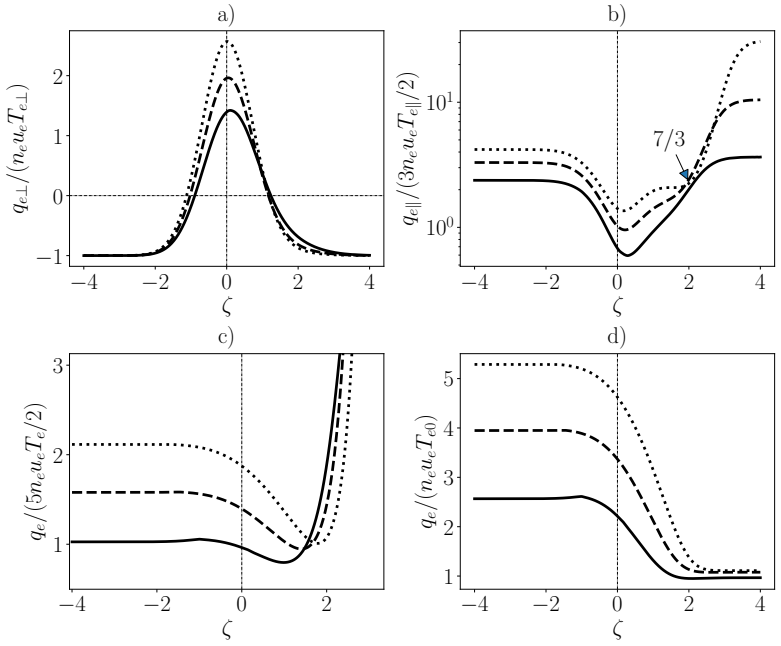

Figure 4.10: (a) Ratio of perpendicular heat flux versus perpendicular thermal energy flux. (b) Ratio of parallel heat flux versus parallel thermal energy flux. (c) Ratio of total heat flux versus thermal energy flux. (d) Ratio of total heat flux versus total flux. $m_i/m_e = 10^3$ (——), 10^4 (- - -), 10^5 (·····), and $T_{i0}/T_{e0} = 10$.

fluxes of perpendicular energy. Further downstream, at $\zeta \approx 2$, all curves intertwine around the value 7/3, and finally the diffusion-to-convection flux ratio increases to the large asymptotic value

$$\frac{2q_{e\parallel}}{3nu_eT_{e\parallel}} \approx 0.8\frac{T_{e0}}{T_{e\parallel\infty}} - 1,$$

obtained from equation (4.31) and Figure 4.7(a).

The splitting of the heat flux of the electron thermal energy into fluxes of parallel and perpendicular thermal energy could be more a disadvantage than a benefit when looking for a comprehensive macroscopic picture of the electron response. Figure 4.10(c) plots the diffusion-to-convection flux ratio of total thermal energy. Compared to Figs. 4.10(a) and (b), this ratio is monotonic down to $\zeta \sim 2$, and then grows to attain a large asymptotic value (not shown there). Figure 4.10(d) plots q_e/nu_e, non-dimensionalized with T_{e0} and confirms that the heat flow q_e/B (which is proportional to q_e/nu_e) is monotonically decreasing. The absence of local extrema around the nozzle throat in figures 4.10(c) and (d), confirms the compensation there

of the magnetic mirror effects on parallel and perpendicular heat fluxes, caused by the exchange between perpendicular energy diffusive flux, $m_e\langle w_\perp^2 c_\parallel\rangle/2$, and parallel energy diffusive flux, $m_e\langle c_\parallel^3\rangle/2$.

In summary, in terms of the electron energy, three regions can be identified in the MN: (1) the convergent region which is near isothermal but with a rather large heat flux, (2) the main divergent region, reaching until $B/B_M \sim 0.01$, with both T_e and q_e/B decreasing, and (3) the far downstream region, with q_e/B near constant and T_e still decreasing to its asymptotic value.

The changing behavior of q_e along the MN and its unclear physical basis does not help to derive a closure relation for the set of electron fluid equations. Nonetheless, to end this subsection, let us comment a crude phenomenological law for q_e, which in the end is going to be equivalent to the phenomenological polytropic law, often used to analyze plasma expansions. Based on Figure 4.10(c), let us take an average value of the diffusion-to-convection flux ratio, i.e. q_e/nu_eT_e =const or, in vector formulation,

$$\boldsymbol{q}_e = \bar{\alpha}\; nT_e\boldsymbol{u}_e, \tag{4.37}$$

with $\bar{\alpha}$ a constant. This is substituted in the stationary internal energy equation

$$\nabla\cdot\left(\frac{5}{2}T_e n\boldsymbol{u}_e + \boldsymbol{q}_e\right) = \boldsymbol{u}_e\cdot\nabla p_e + Q_e, \tag{4.38}$$

where, for compactness, Q_e groups all volumetric sources of internal energy. For the stationary, collisionless case, it is $Q = 0$ and $\nabla\cdot n\boldsymbol{u}_e = 0$, and a straightforward integration of the energy equation yields

$$T_e \propto n^{\bar{\gamma}-1} \quad \text{with} \quad \bar{\gamma} = \frac{5+2\bar{\alpha}}{3+2\bar{\alpha}}, \tag{4.39}$$

with $\bar{\gamma}$ an effective polytropic coefficient. The adiabatic case $\bar{\alpha} = 0$ corresponds to $\bar{\gamma} = 5/3$ and, as the relative heat flux increases, $\bar{\gamma}$ decreases. For instance, the intermediate value $\alpha = 7/2$, extracted from Figure 4.10(c), o yields $\bar{\gamma} \approx 1.2$, a value close to some experimental evidence [42, 78, 69, 70, 74]. Implementing the crude closure (4.37) in the energy equation (4.33) yields the known law between the electric potential fall and the polytropic coefficient,[95]

$$\frac{e|\phi_\infty|}{T_{e0}} \approx \frac{\bar{\gamma}}{\bar{\gamma}-1}. \tag{4.40}$$

This implies that $\bar{\gamma}$ depends on the mass and temperature ratios: for the cold-ion case and using equation (4.26) one has

$$\bar{\gamma} \approx 1 + \left(1 + \ln \sqrt{\frac{m_i}{2\pi m_e}}\right)^{-1}. \tag{4.41}$$

In summary, in a collisionless plasma, the polytropic law (4.39) is equivalent to a constant diffusion-to-convection energy flux law (4.37). Indeed the variation of q_e/nu_eT_e along the nozzle is equivalent to the variation of the 'local polytropic coefficient'

$$\gamma = 1 + \frac{d\ln T_e}{d\ln n} \tag{4.42}$$

computed in Ref. [95], for instance. The advantage of the flux-based law proposed here is that it is easily extended to a weakly collisional plasma expansion. However, the main point to stand out is that both of them are crude phenomenological closures of a collisionless fluid model and do not reproduce the real electron energy balance, mainly in the divergent MN, which generally is the region of most practical interest. This would partially explain that some experimental data requires to be matched with piecewise polytropic laws [69, 42]. In any case, these simple laws have a practical value for fluid simulations, since they provide acceptable spatial profiles of the electric potential, and the plasma density and temperatures.

4.5 Summary and conclusions

A previous work on a kinetic paraxial model of collisionless magnetized plasma, channelled by a convergent-divergent MN, has been complemented here in several directions. One of the central studies has been on magnetic mirror effects. In the fully-magnetized case, those are equally important to ion and electron particles, but macroscopically, magnetic mirror effects manifest only if temperature anisotropy is generated. Contrary to naive intuition, it has been shown that the collective mirror effect is very mild on electrons, in both convergent and divergent regions, except very far downstream (where anyway the electron pressure and temperature are residual).

On the contrary, magnetic mirror effects are shown to be strong on ions, generating a large temperature anisotropy in the ion population. Furthermore, ions

change from having $T_{i\perp}/T_{i\parallel} > 1$ in the convergent MN to $T_{i\perp}/T_{i\parallel} \to 0$ far downstream. Related also to the ion temperature, the comparison of the plasma response when the upstream ion VDF is monoenergetic or Maxwellian shows changes only on second and higher order velocity moments, such as T_i and q_i.

The collisionless macroscopic (i.e. fluid) equations for ions and electrons have been analyzed using the moments of the kinetic solution. First, the ion fluid behavior is different for the cold- and hot-ion cases. While in the first case ion dynamics are dominated by the ambipolar electric field, in the second one the anisotropic pressure and the collective magnetic mirror effect have dominant roles and even ion heat fluxes are not fully negligible in the energy balance.

Since collective magnetic mirror effects are small for electrons, their momentum equation reduces to the standard equilibrium between the electric and pressure forces, but no simple relation between p_e and n (such as the Boltzmann relation) can be invoked in general. In the present collisionless case, the equations for parallel and perpendicular electron energies are the most challenging ones theoretically, since electron heat fluxes are dominant terms in them *even* in the regions where the electrons are practically isothermal. The electron heat flow q_e/B is large and near-constant in the convergent nozzle and then decreases around the throat and the divergent nozzle to reach a downstream asymptotic value. In almost the whole MN, the diffusive thermal flux q_e is larger than the convective one, $(5/2)T_e n u_e$, so its variation along the nozzle is related closely to the total potential fall.

The electron heat fluxes are far from fulfilling a Fourier-type law; in fact, a physical meaning for them in a collisionless fluid is uncertain. Without it, a heat flux is just the mathematical difference between the total (physical) energy flux and what is defined as the convective flux. The search of a physical basis should be further pursued analyzing the corresponding third-order electron fluid equation.

Here, in order to find an approximate closure of the fluid equations, a simple phenomenological law based on a constant diffusion-to convective thermal flux ratio has been discussed. It has been demonstrated to be equivalent to the often invoked polytropic closure, but presents the advantage of being applicable to weakly-collisional discharges too. In any case, these simple laws, although practical, do not reproduce the locally changing physics of the real collisionless discharges.

Due to their practical interest, the parametric dependence of $e|\phi_\infty|/T_{e0}$ on the two free parameters of the model, the propellant mass and temperature ratios, has

been assessed and good analytical approximations have been derived. Similar laws have been obtained for the final beam velocity and parallel temperatures of ions and electrons. Finally and motivated by a previous work on the plasma discharge in a convergent MN followed by a Debye sheath and a wall, the similarities and differences between the electron confinement and electric current control by a very thin sheath and by the semi-infinite divergent region of a MN have been discussed.

The goal of the present paraxial MN model has been to understand fundamental kinetic aspects of a collisionless plasma discharge and their macroscopic manifestation. The implementation of the new findings in the 2D or 3D electron fluid models used, for instance, by the codes DIMAGNO [9], FUMAGNO [92] or EP2PLUS [37, 38] should improve the simulations of plasma expansions in real configurations such as those of space electric thrusters.

Appendix 4.A: Evolution of the velocity distribution functions

In the parametric plane (μ, E), the VDF of each species, f, is constant to first order along the ζ direction. This constant propagation of f from the upstream plasma reservoir is only interrupted by the turning points of the axial velocity, which are given by (4.5), that is

$$L_\zeta : \quad E(\mu;\zeta) = Ze\phi(\zeta) + \mu B(\zeta). \tag{4.43}$$

This equation constitutes a family of straight lines in the (μ, E) plane, with ζ as parameter. For each location ζ, the region locally apt for having particles is the one above the corresponding L_ζ. Far upstream and downstream, the lines are horizontal, while at the MN throat, the line has maximum slope, B_M:

$$L_0 : \quad E(\mu) = 0, \tag{4.44}$$

$$L_M : \quad E(\mu) = B_M\mu + Ze\phi_M, \tag{4.45}$$

$$L_\infty : \quad E(\mu) = Ze\phi_\infty. \tag{4.46}$$

These three lines, together with the envelope Σ of family (4.43), delimit the regions of phase space of free, reflected, and doubly-trapped particles. Figure 4.11 displays these lines for electrons ($Z = -1$) and ions ($Z = 1$) in the cold ions case. There

are four distinct electron regions in the (μ, E) plane, separated by L_∞, L_M and Σ. Region A contains the high-energy, low-μ electrons that manage to escape the MN, i.e., free electrons, for all values of ζ. Region B has reflected electrons initially, and then becomes energetically forbidden downstream as ζ increases. Region C has reflected electrons initially, then becomes forbidden, and then allowed again but empty. Finally, the special region D is delimited by the envelope Σ, formed by line (4.43) in the divergent part of the MN. This region transitions from having reflected electrons, to being forbidden, to having doubly-trapped electrons, to being forbidden again. It is the only region of the parametric plane that can host doubly-trapped electrons. In the case of ions, Σ is the relevant boundary for free (region A). To its right (region C), reflected ions exist initially, then this region becomes forbidden, and then available and empty again..

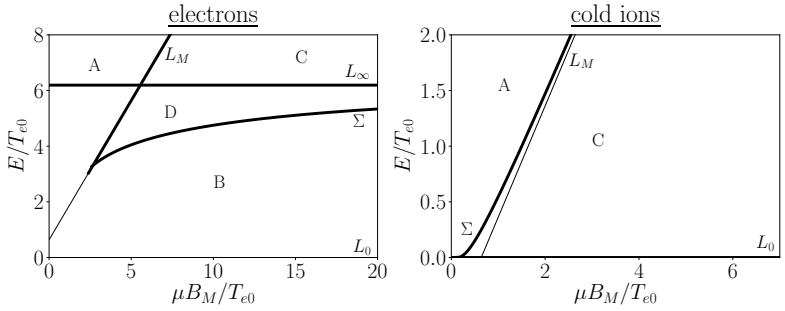

Figure 4.11: Regions in the (μ, E) plane for electrons and ions in the cold ion case, showing the lines L_0, L_M, L_∞ and the envelope Σ. The thicker lines delimit regions where different types of particles are allowed and correspond to: A, free particles; B (only electrons), reflected low energy particles, then forbidden; C, reflected high energy particles, then forbidden, then empty; D (only electrons), reflected particles, then forbidden, then doubly-trapped particles, then forbidden again.

In order to illustrate the evolution of the ion and electron VDFs along the magnetic nozzle and complement the discussion in the main text, Figure 4.12 plots three examples in the $(w_\parallel, w_\perp)$ velocity plane. The first column corresponds to electrons (for the cold-ion case). The second column corresponds to cold Maxwellian ions (a Maxwellian f_{i0}^+ with $T_{i0}/T_{e0} = 0.1$) and the third one to hot ions (a Maxwellian f_{i0}^+ with $T_{i0}/T_{e0} = 10$). For additional illustration, the thick black rings on the two last columns correspond roughly to a monoenergetic f_{i0}^+.

The three lines L_0, L_M and L_∞ of (4.44), (4.45), and (4.46) become the following

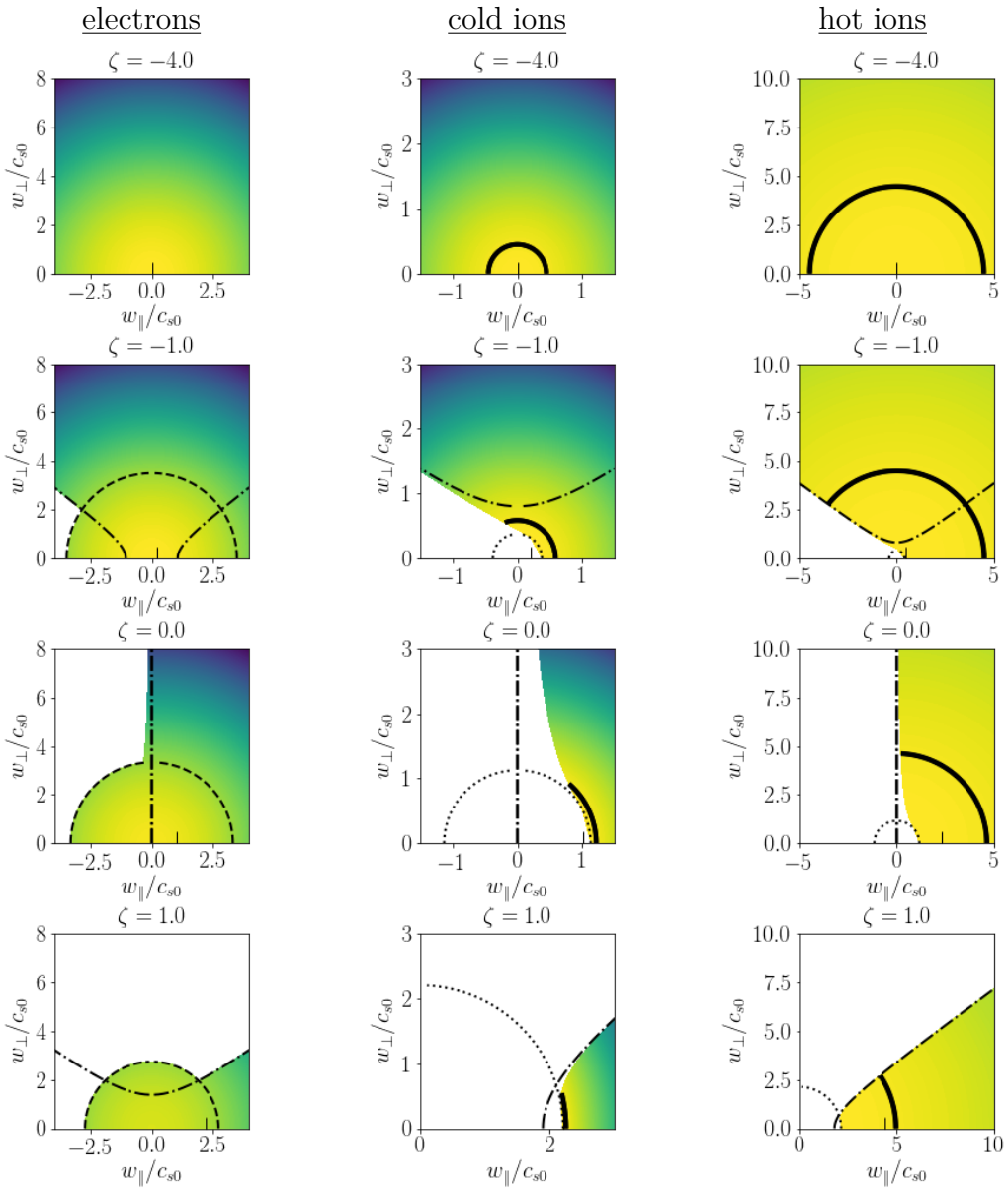

Figure 4.12: Electron and ion VDFs in the velocity plane at four different spatial locations. First column is for electrons in the cold-ion case. Second and Third columns are for a Maxwellian f_{i0}^{+} with $T_{i0}/T_{e0} = 10$ and 0.10, respectively; the thick solid line is for the equivalent monoenergetic case of f_{i0}^{+}. The mass ratio is $m_i/m_e = 10^4$; $c_{s0} = \sqrt{T_{e0}/m_i}$. Dotted lines are for L_0, dash-and-dot ones for L_M, and dashed ones for L_∞. The vertical tick in the x-axis is the local value of the macroscopic velocity u_i. Observe that the $w_\parallel$ axis is shifted in this last row.

conical sections in the velocity $(v_\parallel, v_\perp)$ plane:

$$L_0: \qquad w_\parallel^2 + w_\perp^2 = -\frac{2Ze}{m_\alpha}\phi(\zeta), \tag{4.47}$$

$$L_M: \qquad w_\parallel^2 - \left(\frac{B_M}{B(\zeta)} - 1\right) w_\perp^2 = \frac{2eZ_\alpha}{m_\alpha}\left[\phi_M - \phi(\zeta)\right], \tag{4.48}$$

$$L_\infty: \qquad w_\parallel^2 + w_\perp^2 = -\frac{2Ze}{m_\alpha}\left[\phi(\zeta) - \phi_\infty\right]. \tag{4.49}$$

These lines are plotted in Figure 4.12 as a dotted semi-circle, dash-and-dot hyperbola, and dashed circle, respectively. The envelope Σ is the free boundary of the coloured region, joining with the other curves smoothly. Observe that L_M for ions and electrons are conjugated hyperbolas, and that these hyperbolas become straight lines at $\zeta = 0$, position where they swap the major axis direction. In all plots, those particles on the $w_\parallel > 0$ side of the plane that do not have a corresponding image particle on the $w_\parallel < 0$ side are free particles; regions where particles exist for both $w_\parallel > 0$ and $w_\parallel < 0$ represent reflected or doubly-trapped particles.

In the case of electrons (first column in the Figure), only L_M and L_∞ shape the regions of the VDF. Electrons within the L_∞ semicircle cannot reach the downstream end of the MN, and electrons above the hyperbola L_M cannot reach the nozzle throat. Therefore, only electrons above L_∞ and to the right of L_M are free electrons. For $\zeta < 0$ the rest of them are reflected electrons. For $\zeta > 0$, those below L_∞ and L_M are reflected, while those between these two lines are doubly-trapped ones.

In the case of ions (two last columns), only L_0 and Σ (which approaches L_M in most plots) play a role as indicated in the analysis of the (μ, E) plane. The L_0 semi-circle delimits a region below which no ions exist. For $\zeta < 0$, the forward-moving ions located above Σ cannot reach the throat and are reflected back; below Σ and above L_0, most of the ions are free and the region $w_\parallel < 0$ is almost empty. For $\zeta > 0$, all ions are free ions, and are located to the right of Σ and above L_0. Far upstream essentially all ions are reflected and the ion VDF is Maxwellian. As the expansion begins, an empty region appears (and correspondingly, the free ions can be identified).

At the throat and beyond all ions are free ions. In the divergent side, the empty region grows further, and the hyperbola of (4.48) becomes more eccentric until far downstream only ions with $w_\perp \to 0$ exist.

The different behavior of $T_{i\perp}$ at the throat M for hot- and cold- ions, shown in Figure 4.3(f), can be explained in view of the ion VDF of Figure 4.12. At the throat ($\zeta = 0$), the ion VDF would extend the semiplane $w_\parallel > 0$ and yield $T_{i\perp} = T_{i0}$, were it not for the empty region below the semi-circle L_0 and the arc of envelope Σ. The relevance of this empty region in the integral definition of $T_{i\perp}$ is small for hot-ions but large for cold-ions, leading to the observed $T_{i\perp} \simeq T_{i0}$ in the hot case and $T_{i\perp} \simeq 3T_{i0}$ in the cold case.

CHAPTER

FIVE

Kinetic study of hot and cold electrons co-existence in magnetic nozzles

This Chapter studies the formation of a quasi-neutral steepened layer in a magnetic nozzle by means of a three species (cold xenon ions, hot and cold electrons) collisionless kinetic model, based on the model of Ref.[83] and Chapter 4. A parametric analysis of the solution is provided for the main plasma properties and the thermodynamics of the hot and cold electron species is studied separately. The fraction of hot electrons, as well as their temperature ratio with respect to the cold electrons, determine the total potential drop along the nozzle, which in turn, defines the amount of free escaping electrons. The electron cooling of the hot population is analyzed in detail, showing that they can be strongly affected by the magnetic mirror effect. The maximum plasma potential drop for the same plasma energy at the source is obtained when the hot to cold electrons density ratio at the plasma reservoir is ≈ 3 %. The main energy exchange between species is between the parallel energy flow of hot electrons and the ion kinetic energy flow.

5.1 Introduction

The coexistence of a low temperature plasma with a small population of "hot" (suprathermal) electrons has been widely observed both in nature and in laboratory, such as in the solar wind [53], laser-plasma interactions [111], pulsed-discharge plasmas [79] and electric propulsion thrusters[118]. Energetic electrons can alter significantly the plasma beam expansion, and in electric propulsion thrusters, they can modify the overall system power balance. In material processing, they can even lead to undesirable effects, such as surface damage[135], while in current-free plasma expansions, they can induce the formation of a steepened potential layer [59].

In the field of electric propulsion, regarding the existence of hot electrons, two devices deserve special attention: the so-called Helicon Double Layer (HDL) Thruster [34, 121] and the Electron Cyclotron Resonance (ECR) Thruster[66, 112]. Both of them belong to the electrodeless thruster type, where plasma is quasi-neutrally expanded on the magnetic nozzle (MN) and ions are accelerated due to the ambipolar electric field. In the HDL thruster, there is abundant experimental evidence of a high energetic tail in the electron distribution function [31, 39, 138, 120], although its origin is still unclear, and this is not always present. Furthermore, there is still uncertainty regarding the formation of the electric potential structure in a HDL thruster, and whether it comes from the co-existence of two distinguished electron populations or from two populations of positive ions. However, as was pointed out in Refs. [8, 5, 88], in the outer space, without the interaction with the background chamber pressure, the generation of a small fraction of hot electrons could form a double layer structure in the MN plume of a HDL thruster, what justifies the application of the present study to these devices. With respect to the ECR thruster, there are abundant experiments in ECR sources reporting the generation of a hot electron tail [18, 50, 100, 84]. Recently, Boivin *et al.* have investigated the Electron Energy Probability Function of a microwave low pressure ECR plasma by means of a Langmuir probe and optical emission spectroscopy, finding that it consists of a combination of two Maxwellian populations with disparate temperatures [22]. In addition, an experiment by Jandovitz *et al.* demonstrated the existence of keV electrons in a capacitively-coupled RF plasma source, which could have direct implications in other electric propulsion devices [58].

In a current-free plasma expansion into vacuum, it is well established in the

Literature that the presence of a hot electron population can lead to the formation of a Current-Free Double-Layer (CFDL), which consists of a steepened potential drop localized in a very narrow non-neutral spatial layer. It is important to recall that in a single electron temperature current-free plasma expanding into vacuum, an ambipolar electric field develops naturally due to the difference in the ion and electron dynamics, accelerating ions and confining electrons. The difference in a multiple electron temperature plasma, is that a large portion of the total potential drop can occur in a very localized region of the expansion. If quasi-neutrality is maintained throughout all the expansion, this region can be named as "Quasi-neutral Steepened Layer" (QSL) [8]. Depending on the density fraction of these hot electrons, and their temperature with respect the cold population, the electric potential gradient can be strengthened in such a way that it ends up breaking quasi-neutrality; a non-neutral double layer is formed connecting the two quasi-neutral regions of the expansion. In these cases, the CFDL is considered to be a limit case of the QSL.

Several authors have contributed to the understanding of this phenomenon, both in the laboratory and in the modelling side [116, 5, 88, 76, 1, 126, 119, 59]. Hairapetian and Stenzel were the first to study experimentally the effect of hot electrons in expanding plasmas, and demonstrate the relation between a three species plasma with two electron populations of disparate temperatures and the formation of a steepened potential layer, showing that the total potential fall depends on the density and temperature of the hot electron population [59]. Ahedo and Martínez-Sánchez developed a simple current-free double layer (CFDL) collisionless plasma model, which faithfully reproduced the Hairapetian and Stenzel experiment [8]. In their work, they state that the formation of the double layer is not critically related to the assumption of Maxwellian electrons (two isothermal electron populations), but could influence the CFDL parametric domain, and more importantly, could modify significantly the downstream plasma properties. This last statement constitutes the main motivation of the present study.

In a collisionless magnetized plasma expansion, the electron population does not necessarily follow the Boltzmann relation [24]. While ions are accelerated, a significant part of the electron population is trapped in the magnetic nozzle due to the ambipolar electric potential ("confined" electrons), but a small fraction of the most energetic electrons will escape and neutralize the ion beam ("free" electrons). In

this scenario, a population of doubly-trapped electrons bouncing between two locations of the magnetic nozzle can exist due to the combination of magnetic mirroring and electrostatic barriers [110, 70]. The emergence of empty regions in the electron velocity phase space results in an effective electron cooling [83, 95], which indeed leads to an anomalous closure for the fluid equation hierarchy. As well, asymptotically, the parallel and perpendicular components of the electron temperature decay differently [106]. To the best knowledge of the authors, these kinetic effects have not been considered when modelling the formation of a QSL or double layer in a current-free magnetized plasma expansion, which leaves fundamental questions unanswered.

This Chapter explores the kinetic aspects on the formation of a QSL in a current-free plasma expansion, by re-formulating the model of Ref. [83] to include two electron populations with disparate temperatures. The total potential drop as a function of the hot to cold electrons density fraction at the source and temperature ratio is studied, together with its effect on the hot electrons thermodynamics. The contribution of free, trapped and reflected particles to the macroscopic quantities of both species is studied and results are compared with the response of a two species ion-electron plasma.

The chapter layout is as follows: Section 5.2 describes the formulation of the kinetic model with the main assumptions. Section 5.3 studies the plasma response with the two electron species. Section 5.4 shows a parametric study of the main plasma properties as a function of the model parameters. Section 5.5 analyzes the propulsive performance of the nozzle in terms of specific impulse and energy exchange. Finally, Section 5.6 gathers the main conclusions of this work.

5.2 Kinetic model of a three species plasma

The steady-state paraxial kinetic model of Chapter 4 is extended here to include two electron species with disparate temperatures. Typical topologies for the μ_m curves of both ions and electrons are shown in Figure 5.1.

In this work, the subscript "s" will be used for any *species*, and "h" and "c" will stand specifically for *hot* and *cold* electron species, respectively. The forward VDF of ions and electrons consists of a mono-energetic ion VDF and two Maxwellian

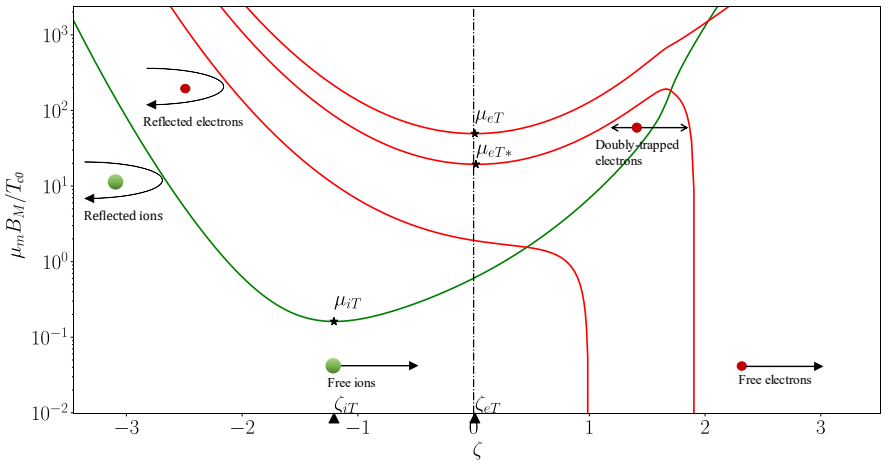

Figure 5.1: Topology of the curves μ_m for ions and electrons.

electron VDFs with disparate temperatures,

$$f_i^+(E_i) = \frac{n_{i0} m_i^{3/2}}{4\pi(3T_{i0}^{1/2})} \delta\left(E_i - \frac{3}{2}T_{i0}\right), \tag{5.1}$$

$$f_s^+(E_e) = \frac{n_{s0}}{(2\pi)^{3/2}} \left(\frac{m_e}{T_{s0}}\right)^{3/2} \exp\left(\frac{-E_e}{T_{s0}}\right), \tag{5.2}$$

with n_{i0}, n_{s0}, T_{i0}, and T_{s0} density and temperature values at the source for each species. The superscripts "f", "t" and "r" will be used for the subpopulations of free, doubly-trapped and reflected particles. *A priori*, both cold and hot electrons contain *all* type of particles, although each subpopulation weights differently on the contribution to the different macroscopic quantities of each species. This will be discussed later.

The contributions of the different subpopulations (free, reflected, doubly-trapped) to the macroscopic moments consider the fluid velocity of the species (u_c, u_h), and not the specific velocity of the subpopulation (u_c^f, u_c^r, u_c^t). In other words, the parallel drift velocity is equal to $c_\parallel = w_\parallel - u$, being $w_\parallel$ the particle parallel velocity and u the fluid velocity of each species (u_c, u_h)

The profile of the ambipolar electric potential $\phi(z)$ needs to be determined so

that quasi-neutrality and current-free conditions are satisfied.

$$n_i = n_h + n_c, \tag{5.3}$$

$$n_i u_i = n_h u_h + n_c u_c. \tag{5.4}$$

An iterative algorithm equivalent to the one in Chapter 4 is used to obtain the self-consistent solution of the problem, for a given value of the model parameters. Once the ambipolar potential profile $\phi(z)$ is determined, any moments of the distribution function can be computed, and kinetic and macroscopic features of the expansion can be analyzed.

Four dimensionless parameters arise from the normalization of the problem: The ion to electron mass ratio m_i/m_e, the ratio between the ion temperature and the electron temperature T_{i0}/T_{c0}, the upstream density ratio of hot electrons $\alpha_0 = n_{h0}/n_{i0}$, and the upstream temperature ratio between the cold and the hot populations $\theta_0 = T_{h0}/T_{c0}$. For this work, the first two parameters are fixed to $m_i/m_e = 2.39 \cdot 10^5$ and $T_{i0}/T_{c0} = 0.01$, representing a plasma beam with cold Xenon ions. Notice that the variation of the solution with these two parameters was already studied in Ref. [83] and in Chapter 4.

5.3 Plasma response with cold and hot electrons

To analyze the response of the two electron species, α_0 and θ_0 have been fixed to 0.03 and 10, respectively. As it will be seen in Section 5.4, these values are representative of the formation of a QSL in a MN. Regarding all the macroscopic quantities (temperatures, heat fluxes, etc.), these are computed with respect to their own species; thus, considering their own density and fluid velocity.

The plasma potential longitudinal profile is plotted in Figure 5.2(a), where a localized steepened drop is observed in the vicinity of $\zeta \approx 2$. In a single ion-electron plasma, most of the potential drop occurs in a more extensive region (between $\zeta = 0$ and $\zeta = 2$ approximately [6]).

Plasma density, represented in Figure 5.2(b), has two differentiated regions; upstream the QSL ($\zeta < 1.3$), cold electrons govern the expansion, while downstream

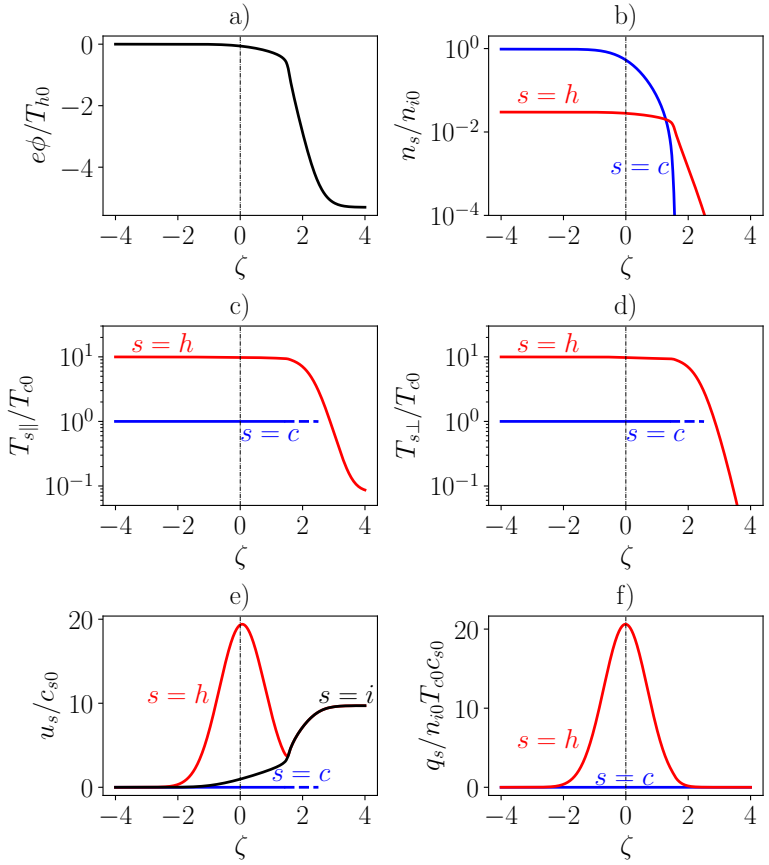

Figure 5.2: Spatial profiles of plasma properties from the cold ("s=c" ——) and hot ("s=h" ——) electron species separately. (a): plasma potential, (b): plasma density, (c): parallel electron temperature, (d): perpendicular electron temperature, (e): fluid velocity, where the the black solid line "s=i" represents the fluid ion velocity and (f): electron heat fluxes. Case for $\alpha_0 = 0.03$ and $\theta_0 = 10$.

the QSL ($\zeta > 1.3$), hot electrons become dominant. In the first region, the hot electrons density remains almost constant, while in the second region, the cold electrons density drops dramatically and becomes almost negligible. Therefore, it can be concluded that, for the represented case, cold electrons "do not exist" beyond $\zeta \approx 2$. For this reason, from this location downwards, the evolution of the cold fluid properties is not depicted in Figure 5.2.

The parallel and perpendicular components of the electron temperatures are shown in Figure 5.2(c) and (d), respectively. The cold electron species is isotropic throughout all the expansion, since the energy distribution function is almost "com-

plete"; all energies are below the escape energy. Oppositely, anisotropy is developed downstream in the hot electrons VDF, analogously to a simple two-species (ion-electron) plasma expansion [83, 6].

The fluid velocity of both negative species is depicted in Figure 5.2(e), normalized with an effective "sonic" velocity at the source c_{s0}, which is defined as a function of the source density ratio α_0 and the source species temperatures T_{c0} and T_{h0},

$$c_{s0} = \sqrt{\frac{1}{m_i \left(\frac{1-\alpha}{T_{c0}} + \frac{\alpha}{T_{h0}}\right)}}. \tag{5.5}$$

This subplot reveals that the fluid velocity of the cold electron species is zero, $u_c = 0$, along all the expansion, which implies that this population is completely confined. Consequently, the current-free condition (equation (5.4)) remains

$$n_i u_i \simeq n_h u_h. \tag{5.6}$$

Figure 5.2(e) shows that downstream of the QSL, the fluid velocity of the hot electrons u_h is exactly the ion fluid velocity u_i, which is an inherent consequence of the current-free condition. From equation 5.6, and defining $\alpha = n_h/n_i$, one has

$$u_h = \frac{u_i}{\alpha}. \tag{5.7}$$

The ion fluid velocity u_i increases along all the expansion, while α is almost constant in the convergent region (see Figure 5.2(b)). However, close to the QSL, α increases dramatically, which is seen as a macroscopic deceleration of u_h. Indeed, the QSL decelerates hot electrons to ensure $u_h \approx u_i$ downstream of the QSL, where this population dominates. After the QSL, $u_h \approx u_i$.

Regarding the electron heat fluxes, plotted in Figure 5.2(e) and (f), it turns out that since the cold electron species is practically confined, its parallel heat fluxes are completely negligible. For the hot electrons, the situation is different, and no simple relation of the heat fluxes with the convective terms *a priori* exists [6].

The main thermodynamic properties of the hot and cold electrons are governed by the contribution of the different subpopulations (free, reflected and doubly-trapped) to the macroscopic quantities. Here, it has been verified that cold electrons

are mainly reflected particles; where the contribution of doubly-trapped particles starts to be significant, the cold electrons density is already negligible. Regarding hot electrons, these are composed of both doubly-trapped and free particles. The type of particles governing the expansion of each species is coherent with the results shown in Figure 5.2.

5.4 Parameter dependence of main plasma properties

This section presents a parametric study of the main plasma properties with α_0 and θ_0. The study is limited to the parametric domain given by $\alpha_0 = [0.01 - 0.1]$ and $\theta_0 = [5 - 20]$.

The variation of the main plasma properties with α_0 is shown in Figure 5.3 for $\theta_0 = 10$, and the variation with θ_0 is depicted in Figure 5.4 for $\alpha_0 = 0.03$. The plasma potential profile and its gradient are plotted in Figures 5.3(a)-5.4(a) and 5.3(b)-5.4(b), respectively. A QSL is observed in the divergent region of the expansion, represented by a localized steepened plasma potential drop, whose location shifts upstream as α_0 increases, and whose strength increases as θ_0 increases. The spatial location of the QSL is very weakly dependent on the temperature ratio (although it slightly shifts upstream when increasing θ_0). The region affected by the QSL is narrower for larger values of θ_0.

The ion fluid velocity, depicted in Figures 5.3(c)-5.4(d), behaves analogously to the plasma potential profile. The ion Mach number M, shown in Figures 5.3(d)-5.4(d), is defined as follows:

$$M = \frac{u_i}{\frac{1}{\sqrt{m_i\left(\frac{1-\alpha}{T_c}+\frac{\alpha}{T_h}\right)}}}. \tag{5.8}$$

In a regular two-species (ion-electron) MN expansion, the ion fluid velocity is sonic in the vicinity of the magnetic throat, and the local sound speed $c_s = \sqrt{T_e/m_i}$ decreases downstream due to the electron cooling [83], but in a three species plasma with two Maxwellian electron populations, the local sound speed increases from $\sqrt{T_c/m_i}$ to $\sqrt{T_h/m_i}$, which leads to a minimum in the local Mach number. In the present model, these two effects co-exist in the expansion, and therefore, the local sound speed could have a non-monotonic behaviour. The electron cooling

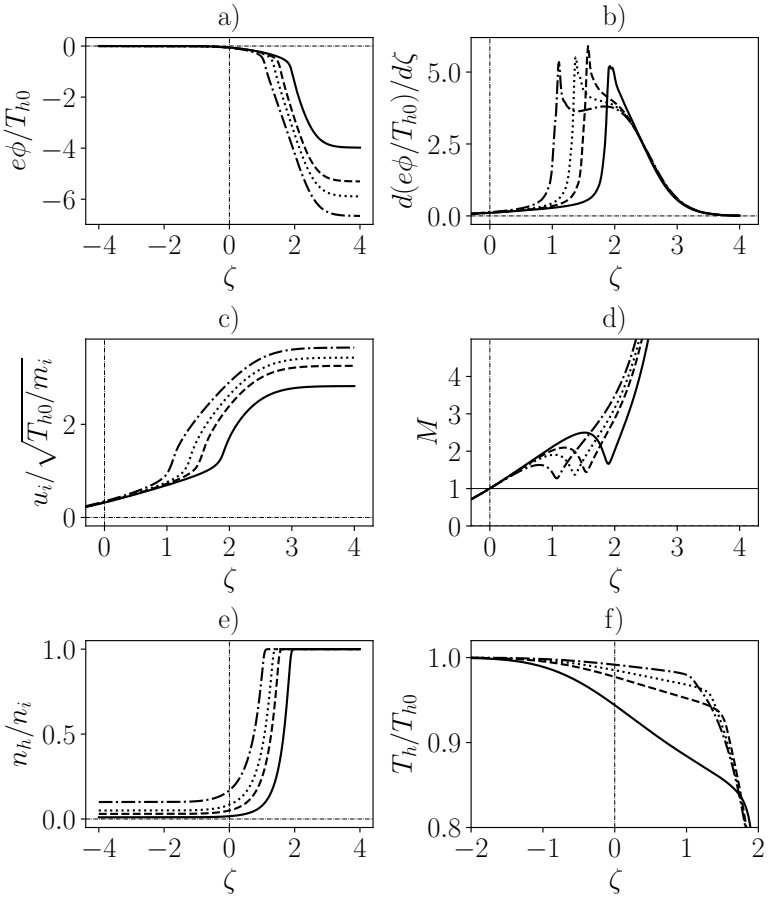

Figure 5.3: α_0 parametric plots. Profiles of main plasma properties for $\theta_0 = 10$ and $\alpha_0 = 0.01$ (——), $\alpha_0 = 0.03$ (- - -), $\alpha_0 = 0.05$ (·····) and $\alpha_0 = 0.10$ (-·-·-). Subplots are for (a) Plasma potential, (b) Plasma potential gradient (c) Ion velocity (d) Local Mach number (e) α and (f) Hot electron temperature.

counteracts the increase of the local sound speed, and consequently, extends the parametric space of the quasi-neutral steepened layer domain. For all the results presented here, there is only one sonic point in the expansion; several sonic crossings will lead to a non-neutral double layer [5], a domain not covered by the present model. These results show how the ion Mach number M, in the vicinity of the QSL, approaches the sound speed (and the non-neutral DL domain) for larger values of θ_0.

The hot electrons density ratio n_h/n_i is shown in Figures 5.3(e)-5.4(e) along the expansion. If we compare this plot with Figures 5.3(a)-5.4(a), respectively, it is

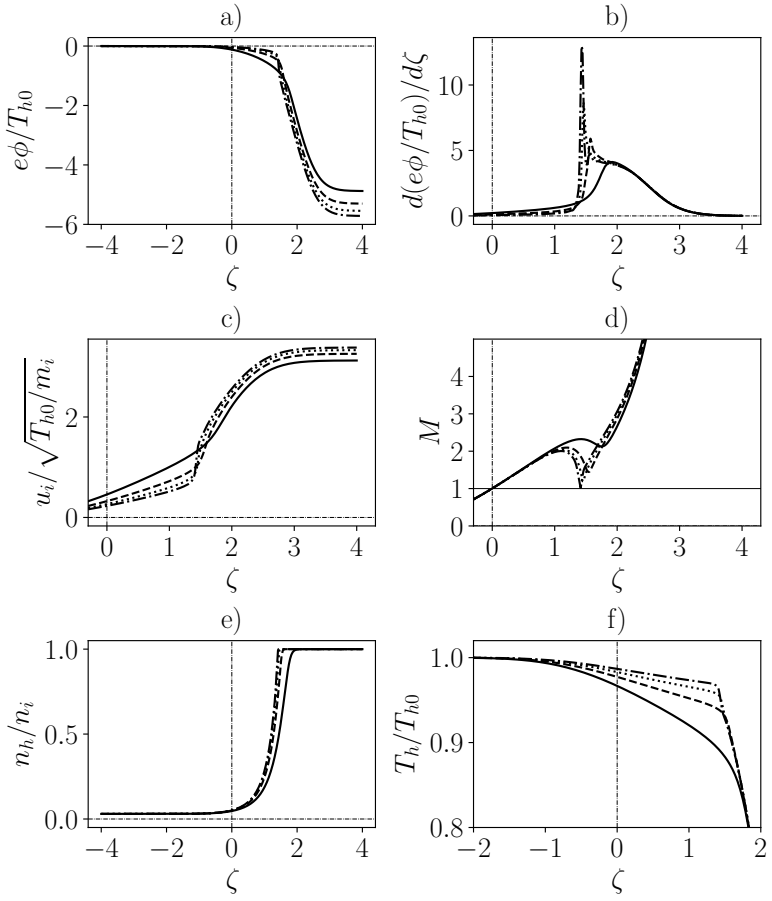

Figure 5.4: θ_0 parametric plots. Spatial variation of main plasma properties for $\alpha_0 = 0.03$ and $\theta_0 = 5$ (——), $\theta_0 = 10$ (- - -), $\theta_0 = 15$ (·····) and $\theta_0 = 20$ (-·-·-). Subplots are for (a) Plasma potential, (b) Plasma potential gradient (c) Ion velocity (d) Local Mach number (e) Plasma density and (f) α.

clear that the hot electrons come to dominate the expansion right after the QSL. These results suggest that the location of the QSL in the expansion is determined by the fraction of hot electrons at the source, while the temperature ratio will basically increase its strength.

Plasma density is plotted in Figure 5.5 as a function of the ambipolar plasma potential. It is clear that the hot electrons come to dominate the expansion right after the QSL, which is represented as a change of slope in the $\log n - \phi$ relation. Figure 5.5(b) shows how increasing θ_0 narrows the extension of the QSL region.

Finally, the electron temperature of hot electrons, $T_h = T_{h\parallel}/3 + 2T_{h\perp}/3$, is

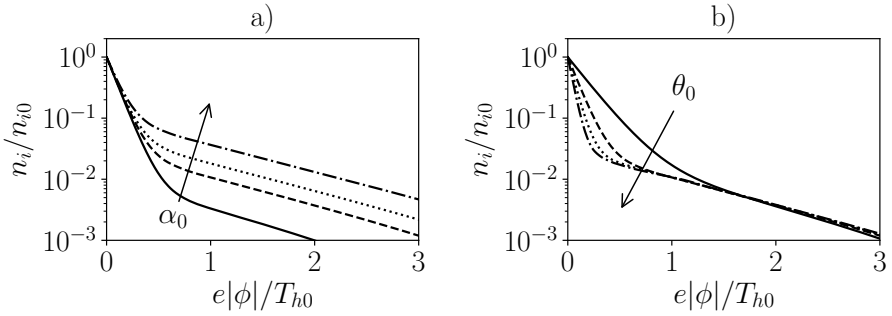

Figure 5.5: Plasma density profile as a function of the electric potential. (a): Cases for $\theta_0 = 10$ and $\alpha_0 = 0.01$ (——), $\alpha_0 = 0.03$ (- - -), $\alpha_0 = 0.05$ (·····) and $\alpha_0 = 0.10$ (-·-·-). (b): Cases for $\alpha_0 = 0.03$ and $\theta_0 = 5$ (——), $\theta_0 = 10$ (- - -), $\theta_0 = 15$ (·····) and $\theta_0 = 20$ (-·-·-).

depicted in Figures 5.3(f)-5.4(f) from $\zeta = -2$ to $\zeta = 2$, since it is where it presents the largest variation (outside this range it remains almost unchanged). A higher cooling rate is observed in this region for lower values of α_0, and lower values of θ_0; this is, where the lowest total potential drop is observed. From all the cases represented here, $\alpha_0 = 0.01$ and $\theta_0 = 5$ has the largest cooling rate in the QSL region; Figure 5.6 plots the parallel and perpendicular components of the electron temperature from $\zeta = -2$ to $\zeta = 2$. A strong anisotropy is observed, which is a collective effect of the magnetic mirror and the electric potential drop [6]. This plot reveals an important aspect of the expansion: hot electrons are more affected by the magnetic mirror effect at lower values of α_0 and θ_0. The rationale behind this statement is the contribution of free electrons to the macroscopic moments. At lower values of α_0 and θ_0, the total potential drop of the nozzle is lower, the contribution of the free population is larger (more electrons are able to overcome the total potential drop).

The macroscopic effect of the magnetic mirror and the electric potential drop can be evaluated by computing the contribution of the different terms to the electron momentum equation, as was shown in Ref. [6]. Figure 5.7 shows the electron momentum equation broken down into the different terms. To spot the differences, two cases are plotted: $\alpha_0 = 0.01$ and $\alpha_0 = 0.03$, both for $\theta_0 = 5$. In the first case, the anisotropic term can not be neglected, and affects significantly the shape of the parallel pressure gradient.

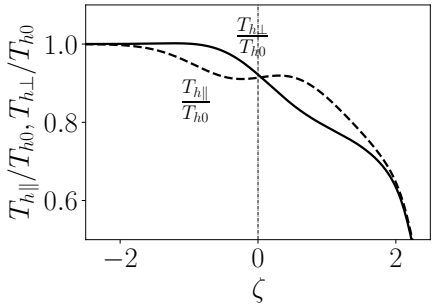

Figure 5.6: Perpendicular temperature (——) and parallel temperature (- - -) of hot electrons for $\theta_0 = 5$ and $\alpha_0 = 0.01$.

To conclude, the thermodynamics of the hot population is more affected by the magnetic mirror effect in those cases where the total potential drop decreases, while it behaves as in a single ion-electron plasma for large values of $e|\phi_\infty|/T_{h0}$. Notice that this analysis is analogous to the "hot ions" case of Chapter 4, where we saw that they were barely affected by the potential drop, and strongly by magnetic mirroring.

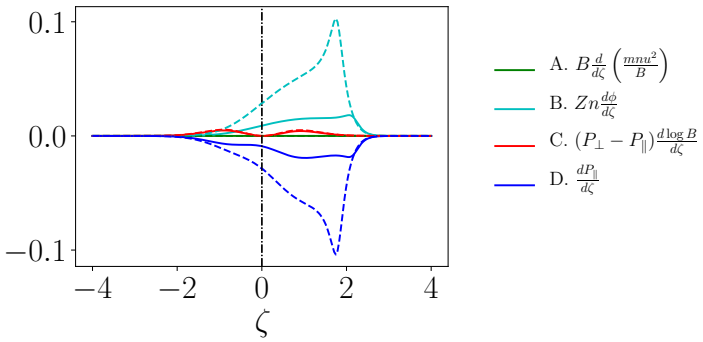

Figure 5.7: Contribution of the different terms to the hot electrons momentum equation for $\theta_0 = 5$, $\alpha_0 = 0.01$ (solid) and and $\alpha_0 = 0.03$ (dashed).

5.4.1 Limit of the QSL parametric domain

The kinetic model iterates numerically the profile of the ambipolar plasma potential $\phi(z)$ in order to minimize the local error at each point of the mesh. Systematically, it is considered that a solution has been found when the mean quadratic error is below the desired tolerance. However, as it is shown in Figure 5.8(b), for some regions of

the parametric domain, the established tolerance is not reached because the quasi-neutrality relative error breaks in a very localized region of the mesh. Here, it has been found that in the parametric domain defined by $\alpha_0 = [0, 1]$ and $\theta_0 = [0, 20]$, the non-compliance of the desired tolerance is directly linked to a very narrow non-neutral spatial region. Figure 5.8(a) shows the maximum relative error on the compliance of the local quasi-neutrality condition. It has been verified that regions with a large maximum local error ($\geq 10\%$) belong to the parametric domain of a non-neutral double layer identified by Ahedo and Martínez Sánchez [8]. Although the quasi-neutrality error found here is very localized, and the two converged regions could be analyzed separately, an additional model for the non-neutral region should be implemented in order to properly solve the complete expansion. The current model can not solve the plasma expansion if a non-neutral double layer is present, and therefore we are limited to the QSL domain.

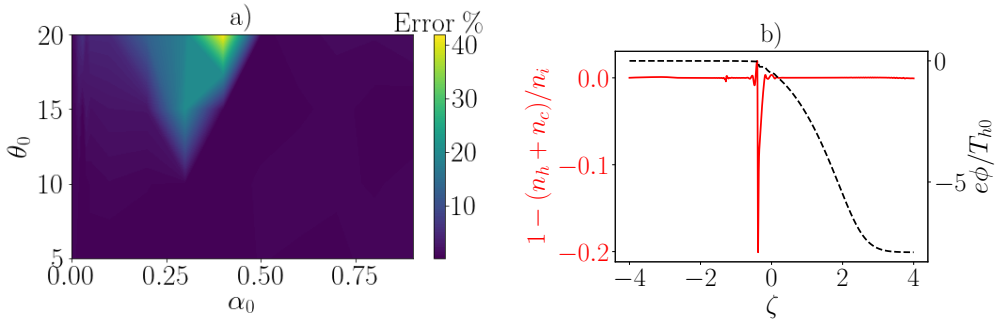

Figure 5.8: a) Color map of the maximum quasi-neutrality relative percentage of local error as a function of the model parameters α_0 and θ_0 b) Quasi-neutrality relative local error (———) for $\alpha_0 = 0.3$ and $\theta_0 = 15$ together with the ambipolar plasma potential profile (- - -).

5.5 Analysis of the propulsive performance of the nozzle

The isothermal behaviour of electrons assumed by some fluid models leads to an unbounded plasma potential, and consequently, an infinite ion beam acceleration. In our kinetic model, since the total potential drop has a finite value, it is possible to study the effect of expanding a three-species plasma on the total acceleration of the plume. Since in the cold ion limit ($T_{i0} \ll T_{e0}$), which is the case studied here, the final ion velocity scales with $\sqrt{2e|\phi_\infty|/m_i}$, the total potential drop $e|\phi_\infty|$ is used

to quantify the effect of α_0 and θ_0 in the total specific impulse of the MN. It must be noticed that in a simple ion-electron plasma, $e|\phi_\infty|$ is only related to the ion to electron mass ratio m_i/m_e and the ion to electron temperature ratio T_{i0}/T_{e0} [83].

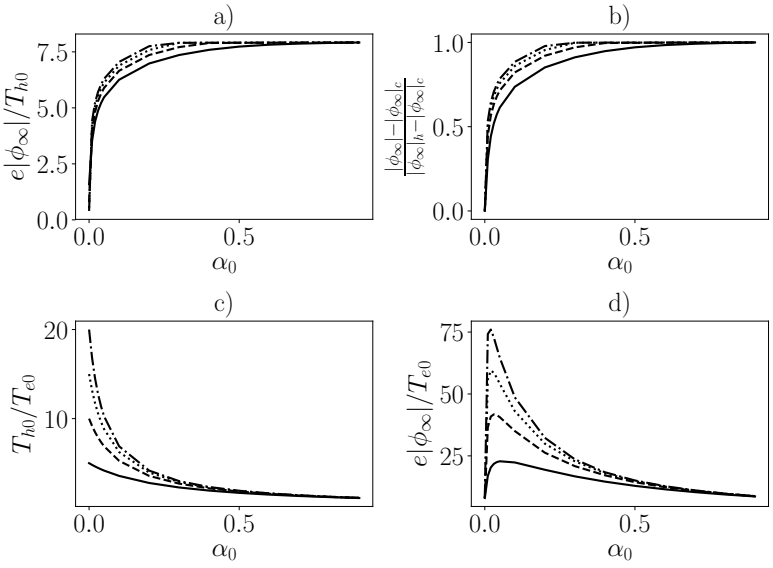

Figure 5.9: (a) Parametric solution of the total potential drop against T_{h0}, (c) Normalized parametric solution of the total potential drop (c) values of T_{h0}/T_{e0} in the parametric domain of α_0 and θ_0 and (d) Parametric solution of the total potential drop against T_{e0}. Curves are for $\theta_0 = 5$ (——), $\theta_0 = 10$ (- - -), $\theta_0 = 15$ (·····) and $\theta_0 = 20$ (-·-·-).

To evaluate the influence of α_0 and θ_0 on the specific impulse, Figure 5.9(a) plots the total potential drop with respect to T_{h0} as a function of α_0 for four different values of θ_0. As α_0 increases, $e|\phi_\infty|/T_{h0}$ approaches an asymptotic value and becomes independent of α_0, as it is expected; for larger values of θ_0, this value is reached with a lower fraction of hot electrons. However, it is important to notice that curves in Figure 5.9(a) have different values at $\alpha_0 = 0$. In order to properly assess the influence of this parameter, the curves have been normalized and plotted in Figure 5.9(b). These two figures show that with a small amount of hot electrons, the total potential drop scales mostly with T_{h0}. However, since without hot electrons the total potential drop scales with T_{c0}, its value necessarily depends on the temperature ratio. From Figure 5.9(b), one can extrapolate and deduce that for a very large value of θ_0, the corresponding curve will have an infinite slope.

The shape of curves in Figure 5.9(a) and (b) has several implications. For

$0 < \alpha_0 < 0.2$, the total potential drop with respect the hot electrons temperature is lower than for a two species ion-electron plasma, which affects the thermodynamics of the hot electrons species. Since hot electrons see a lower potential drop, they will be less confined (the contribution of free particles will be larger). One of the most important consequences, as it has been shown in the previous section, is that they will be more affected by the magnetic mirror effect. For electrons, a large electric potential drop diminishes the collective effect of the magnetic mirror.

Figure 5.9(a) suggests that there is a value of α_0 for a given θ_0 that will give the maximum specific impulse of the nozzle. In other words, there is a minimum amount of the hot electrons density fraction which ensures that the total potential drop scales with the hot electrons temperature, and increasing the value of this fraction will increase the energy deposited into the plasma, but will not increase the specific impulse anymore. In order to study this, an effective source temperature is defined as:

$$T_{e0} = (1 - \alpha_0)T_{c0} + \alpha_0 T_{h0}. \tag{5.9}$$

In our model, which does not account for any energy losses, this temperature is equivalent to the total energy deposited into the plasma source.

Figure 5.9(c) shows the dependence of the ratio T_{h0}/T_{e0} with θ_0 and α_0. By multiplying the curves of Figure 5.9(a) by T_{h0}/T_{e0} (the corresponding curves of Figure 5.9(c)), Figure 5.9(d) is obtained, which shows the total potential drop with respect to T_{e0}, which increases linearly with α_0 from T_{c0} to T_{h0}. Notice that $e|\phi_\infty|$ scales with T_{c0} for $\alpha_0 = 0$ and with T_{h0} for $\alpha_0 = 1$.

Figure 5.9(d) enables the identification of the value of α_0 for which the largest electric potential drop (i.e., specific impulse) is obtained for the same "effective" energy at the source. In this regard, the value of $e|\phi_\infty|/T_{e0}$ must be indistinguishable when $\alpha_0 = 0$ and when $\alpha_0 = 1$ as long as ions remain "cold" with respect to the electrons, and this is confirmed by the solution.

For each θ_0, there is a value of α_0 where the ratio $e|\phi_\infty|/T_{e0}$ is maximum. This value turns out to be around $\alpha_0 = 0.03$; this is, 3% of the initial electron density belonging to the hot electron species. However, it slightly decreases with θ_0. From this analysis, we conclude that the optimum value of the hot electrons density fraction at the source is around 3%. Increasing this value will need more energy

to be deposited at the source, and will not improve significantly the total specific impulse of the nozzle.

Particular attention should be paid to this analysis, since although a QSL can provide a large gain in specific impulse, it can also imply a significant increment in the power deposited. The correct assessment of the propulsive quality of the magnetic nozzle must study how much power is required to obtain the same T_{e0} (which ,in turn, will depend on the heating mechanism). In our model, since there are no power losses possible, the efficiency of the nozzle is considered to be 100 %. Notice that the total energy equation for each species in the paraxial limit is

$$\frac{nuZe\phi}{B} + \frac{nu}{B}\left[\frac{mu^2}{2} + \frac{3T_\parallel}{2} + T_\perp\right] + \frac{q_\parallel + q_\perp}{B} = \text{const.} \tag{5.10}$$

Along the expansion, there is an energy exchange between the electric potential and the rest of the terms. A detailed analysis of the internal energy transfer of each species separately was performed in Chapter 4, so here we focus on the energy transfer between species by means of the ambipolar electric potential. First, since the constant nu/B is several orders of magnitude smaller for the cold electrons, this population does not contribute *at all* to the total energy flow balance; it is the total thermal energy flow of hot electrons what is converted into kinetic ion energy flow. However, not all the electron energy flow is transferred into energy flow, since far downstream there is a remaining non-negligible electron parallel heat flow, as was seen in Chapter 4. Regarding the cold electrons energy flows, they are completely negligible in the total plasma energy balance and therefore they are not involved in the electron-ion energy transfer.

5.6 Conclusions

The kinetic model of Ref. [83] and Chapter 4 has been extended to include a three species plasma MN with cold xenon ions and cold and hot electrons, which allows to study the formation of a QSL in a current-free plasma expansion. Two dimensionless parameters govern the expansion, the ratio of hot electrons density α_0 and the temperature ratio between the hot and the cold electron species θ_0.

The plasma response when a QSL is formed has been discussed. The cold electron species turns out to be a completely confined isothermal population (conclud-

ing that for them, the hypothesis of Boltzmann's relation is a good approximation), and it governs the expansion upstream of the QSL. The thermodynamics of the hot electrons has been found to be analogous to the one of electrons in a two species ion-electron plasma, and to be driven by the total potential drop of the MN.

A parametric study of the quasi-neutral solution has been performed. A QSL is formed in the studied parametric domain, and its spatial location depends on the value of α_0. It has been shown that the role of θ_0 is mainly to increase the intensity of the QSL. The plasma response to the parametric variation of α_0 and θ_0 presented here is consistent with the fluid-Boltzmann model developed by Ahedo in Ref. [5]. However, in the kinetic model presented here, the plasma potential tends asymptotically to a finite value $e|\phi_\infty|$, something that cannot be modelled in Ref. [5]. This feature modifies the main plasma response in the divergent side of the expansion.

In the parametric study, it has been shown that as $e|\phi_\infty|/T_{h0}$ decreases, hot electrons are macroscopically more affected by the magnetic mirror effect (the contribution of free electrons is larger), showing a large anisotropy along the expansion. This phenomenon has not been observed before when analyzing the MN of xenon ions and a single electron species, and reveals an important aspect of the expansion: if the fraction of hot electrons is very small, which is the case of interest, they will be strongly affected by the magnetic mirror effect. The analysis is analogous to the "hot ions" case studied in Chapter 4.

The finite total potential drop of the nozzle has allowed to perform a parametric analysis of the MN performance in terms of specific impulse. It has been shown that the ratio between the total potential drop and the hot electrons temperature increases with θ_0 and α_0, as expected. For $\alpha_0 > 0.2$, the total potential drop $e|\phi_\infty|$ scales directly with T_{h0}, for all the cases represented here. For the same plasma energy at the source, the maximum acceleration of the ion beam occurs in the vicinity of $\alpha_0 \approx 0.03$ in the parametric domain studied here, almost independently of θ_0.

Finally, the electron energy equation reveals that the cold electron species does not contribute *at all* to the total energy balance and the energy exchange in the nozzle is from the hot electron parallel flows to the ion kinetic energy flow, with a remaining parallel heat flow of hot electrons far downstream.

CHAPTER

SIX

Anisotropic bi-Maxwellian electrons expanding in magnetic nozzles

This chapter analyzes the collisionless plasma expansion in a magnetic nozzle where the upstream electron velocity distribution function is formulated as bi-Maxwellian (different temperatures in the parallel and perpendicular directions to the magnetic field line). Two steady-state paraxial models are implemented: a convergent-divergent kinetic model and a hybrid divergent model. Solutions are obtained for xenon ions, for a wide range of the electron temperature anisotropy ratio. The kinetic effects, as well as the macroscopic plasma response, when expanding an anisotropic bi-Maxwellian EVDF in a magnetic nozzle are described. The main contributions and limitations of the present study are highlighted.

6.1 Introduction

In thermodynamic equilibrium, one can expect the velocity distribution function of a certain species to have a Maxwellian shape. However, in particular situations, this distribution can be far from Maxwellian; for instance, a collisionless plasma immersed in a varying magnetic field can develop a large anisotropy due to the magnetic mirror effect. As well, in ECR sources, due to the nature of the heating mechanism, electrons absorb energy in the direction perpendicular to the magnetic field lines, which is transferred to the parallel direction by means of collisional events or inverse magnetic mirror. However, in a low density regime, collisions can be insufficient to ensure thermodynamic equilibrium, resulting in an anisotropic electron velocity distribution function (EVDF) with a larger kinetic energy dispersion in the perpendicular direction.

In the ECR thruster, the EVDF can be highly anisotropic at the thruster exit [62, 54, 52, 60], but the implications in the thruster performance are still unclear. There is experimental evidence of electron temperature anisotropy in ECR sources [11, 13, 85, 25]. The most outstanding work is the one from Amemiya *et al.*, where they measured perpendicular electron temperatures up to 30 % larger than parallel electron temperatures inside an ECR source [13]. However, there is a lack of experimental evidence regarding electron anisotropy along the MN of an ECR thruster. Sercel did measure different values for the parallel and perpendicular electron temperatures, although he attributed them to possible errors in the experiments [113]. Measuring accurately enough the parallel and perpendicular components of the electron temperature along a MN is not trivial, and it is a current field of research (the error in the electron temperature obtained by means of Langmuir Probes can be around 20 % [57] in both components). Recapitulating, there is experimental evidence of electron temperature anisotropy inside ECR sources, but there is a lack of experimental data regarding temperature anisotropy along the MN of ECR thrusters. Therefore, developing theoretical models capable of predicting the plasma response along a MN when the EVDF at the thruster exit is anisotropic is becoming a critical need.

To contribute to the understanding of these phenomena, this chapter is devoted to exploring the evolution along a MN of a non-isotropic electron distribution function already at the plasma reservoir. Two paraxial models have been developed

based on the model of Ref. [83]; a fully-kinetic convergent-divergent model, and a hybrid divergent model. The results of both models are presented here, analyzing the impact of expanding an anisotropic EVDF along a MN.

The present chapter is organized as follows: Section 6.2 presents the convergent-divergent kinetic model and a parametric analysis of the results. Section 6.3 shows the results obtained with a divergent hybrid model with fluid ions and kinetic electrons. Finally, Section 6.4 summarizes the main contributions of this work, as well as suggestions for advances in the modelling side.

6.2 Convergent-divergent model

The convergent-divergent kinetic model is analogous to the model of Ref. [83] and Chapters 4 and 5, with a Maxwellian ion distribution function and an anisotropic bi-Maxwellian EVDF at the plasma source, given by:

$$f_e^+(w_\parallel, w_\perp) = \frac{m_e n_{e*}}{(2\pi)^{3/2} T_{e\perp *}} \left(\frac{m_e}{T_{e\parallel *}}\right)^{1/2} \exp\left(-\frac{m_e w_\parallel^2}{2T_{e\parallel *}} - \frac{m_e w_\perp^2}{2T_{e\perp *}}\right). \tag{6.1}$$

By assuming conservation of mechanical energy and magnetic moment, one can express the distribution function in terms of these two invariants, leading to:

$$f_e^+(E_e, \mu_e) = \frac{m_e n_{e*}}{(2\pi)^{3/2} T_{e\perp *}} \left(\frac{m_e}{T_{e\parallel *}}\right)^{1/2} \exp\left(\frac{B_0 \mu_e}{T_{e\perp *}}\left(-1 + \frac{T_{e\perp *}}{T_{e\parallel *}}\right)\right) \exp\left(\frac{-E_e}{T_{e\parallel *}}\right) \tag{6.2}$$

Equation (6.2) reveals that f_e^+ is not a function only of the electron energy E_e, as it was in the isotropic case, but it also depends on the electron magnetic moment μ_e. Moreover, the ratio $T_{e\parallel *}/T_{e\perp *}$ defines the sign of the exponential function, which must be considered when evaluating the integral moments. In principle, as in Chapters 4 and 5, n_{e*}, $T_{e\parallel *}$ and $T_{e\perp *}$ are reference magnitudes, and are not necessarily the electron density and temperatures at the source. However, as long as the initial value of the magnetic field is several orders of magnitude lower than the magnetic field at the throat, $f_e^+ \simeq f_e^-$, and the reference magnitudes n_{e*}, $T_{e\parallel *}$ and $T_{e\perp *}$ are exactly the density, parallel and perpendicular electron temperatures at the source, respectively. For all the results presented here, this condition is perfectly satisfied, and therefore $n_{e*} \simeq n_{e0}$, $T_{e\parallel *} \simeq T_{e\parallel 0}$ and $T_{e\perp *} \simeq T_{e\perp 0}$. The same applies

for ions, meaning $T_{i*} \simeq T_{i0}$. In the rest of the Chapter, the reference magnitudes will be referred directly as the source magnitudes.

After normalizing the quasi-neutrality and current-free equations, the formulation leads to three dimensionless parameters: the already known ion to electron mass ratio m_i/m_e and ion to electron temperature reference ratio $T_{i0}/T_{e\|0}$ and the electron parallel to perpendicular reference temperature ratio $T_{e\|0}/T_{e\perp 0}$. The results presented in this Chapter are exclusively for xenon ions.

6.2.1 Kinetic effects: isotropization of the EVDF

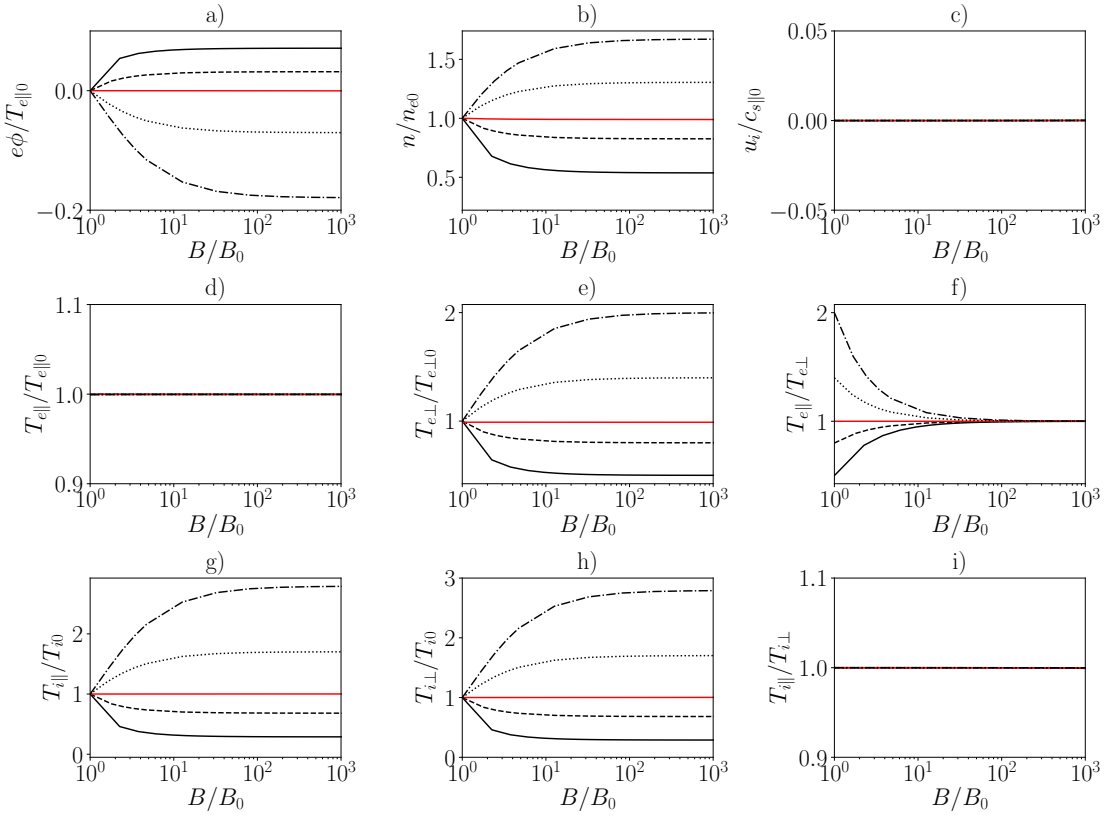

Figure 6.1: Evolution of main plasma properties along the convergent side of the expansion. The magnetic throat is located at $B/B_0 = 10^7$. Cases are for $T_{i0}/T_{e\|0} = 0.1$ and $T_{e\|0}/T_{e\perp 0} = [0.5, (\text{——}), 0.8\ (\text{- - -}), 1.0\ (\text{——}), 1.4\ (\cdots\cdots)$ and $2.0\ (\text{-·-·-})]$.

The plasma response in a convergent-divergent MN when the EVDF is bi-Maxwellian at the plasma reservoir differs from the Maxwellian case only in the convergent region. Figure 6.1 plots the main plasma properties as a function of

B/B_0 for different values of $T_{e\|0}/T_{e\perp 0}$, where B_0 is the magnetic field at the upstream source. In these simulations, the magnetic throat is located at $B_M/B_0 > 10^3$. The isotropic solution (shown as a red solid line in Figure 6.1) within this region is almost constant; therefore, all the variations observed are directly related to the anisotropic character of the EVDF.

Figure 6.1(a) shows that as the magnetic field increases, an additional electric potential gradient is developed, whose sign depends on the sign of $T_{e\|0} - T_{e\perp 0}$. If $T_{e\|0} > T_{e\perp 0}$, there is an additional negative potential drop, but if $T_{e\perp 0} > T_{e\|0}$, a positive potential drop is developed, which implies that the electric potential profile losses its monotonic character. However, this potential drop is negligible with respect the total potential drop along the MN ($\approx 8T_{e\|0}$ for xenon ions), which in turn, is not modified with the parameter $T_{e\|0}/T_{e\perp 0}$, as it is shown in Figure 6.2, which represents the complete solution of the ambipolar plasma potential profile along the convergent-divergent expansion for three different values of $T_{e\|0}/T_{e\perp 0}$.

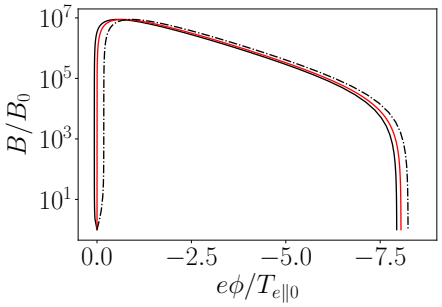

Figure 6.2: Solution of the ambipolar plasma potential along the convergent-divergent expansion. Cases are for $T_{i0}/T_{e\|0} = 0.1$ and $T_{e\|0}/T_{e\perp 0} = [0.5, (\text{——}), 1.0 (\text{——}) \text{ and } 2.0 (\text{-·-·-})]$.

Regarding electrons, the most significant effect is that there is an "isotropization" of the EVDF; the perpendicular component of the electron temperature increases or decreases to match the parallel component as B increases, as it is shown in the subplots of the second row of Figure 6.1. This isotropization is a direct consequence of the magnetic mirror in a collisionless non-Maxwellian plasma. In the absence of collisions, each particle conserves its total energy, and its magnetic moment is conserved due to the the fully magnetization assumption. The distribution function $f_e(E_e, \mu_e)$ is constant along each magnetic line. In the region plotted in Figure 6.1, $f_e^+(E_e, \mu_e) \simeq f_e^-(E_e, \mu_e)$, since the magnetic field is still several orders

of magnitude lower than the value at the magnetic throat, and there are hardly any empty regions in the EVDF.

Then, according to equation (6.2), the following quantity is invariant in this region:

$$\frac{B_0\mu_e}{T_{e\perp 0}}\left(-1+\frac{T_{e\perp 0}}{T_{e\parallel 0}}\right)-\frac{E_e}{T_{e\parallel 0}}=const. \tag{6.3}$$

By replacing E_e and μ_e with the total energy and magnetic moment conservation equations, respectively, the invariant remains as follows:

$$\frac{m_e}{2}\left(\frac{w_\parallel^2+w_\perp^2}{T_{e\parallel 0}}\right)-\frac{e\phi}{T_{e\parallel 0}}+\frac{B_0}{B}\left(\frac{1}{T_{e\perp 0}}-\frac{1}{T_{e\parallel 0}}\right)\frac{m_e w_\perp^2}{2}=const. \tag{6.4}$$

In the velocities space $(w_\parallel, w_\perp)$, equation (6.4) has an elliptical shape, whose eccentricity is initially defined by the second term of the equation. As B increases, the second term of equation (6.4) decreases. Therefore, f_e is circularized as B increases its value; in other words, there is an isotropization of the electron velocity distribution function. This basic phenomenon is just a consequence of how f_e is redistributed in the velocities space along the expansion. Even if the curves $f_e = const$ are initially elliptical, in the absence of collisions, particles can only "move" in this space phase in circumferences due to energy conservation.

The isotropization effect is visualized in Figure 6.3, which represents f_e in the velocities space, at three different values of B/B_0, for two different cases $T_{e\parallel 0}/T_{e\perp 0} = 0.5$ (left), and $T_{e\parallel 0}/T_{e\perp 0} = 2.0$ (right). The black solid line, which represents one curve of $f_e = const$, is circularized as B increases. This isotropization phenomenon has also an impact on the local density. As it is plotted in Figure 6.1(b), there is an increase of the plasma density if $T_{e\parallel 0}/T_{e\perp 0} > 1.0$, and a decrease if $T_{e\parallel 0}/T_{e\perp 0} < 1.0$. The effect on the fluid velocity, shown in Figure 6.1(c), is almost negligible, since changes in u are proportional to changes in B/n (mass conservation).

Finally, regarding ions, Figure 6.1(g)-(i) show the evolution of the ion temperature in this region, which is directly linked to the ambipolar electric potential gradient. An additional negative gradient ($T_{e\parallel 0}/T_{e\perp 0} > 1.0$), increases the ratio of the curves corresponding to $f_i = const$ in the ion velocities space, which without any other kinetic effect, implies an increase of the ion temperature. The opposite

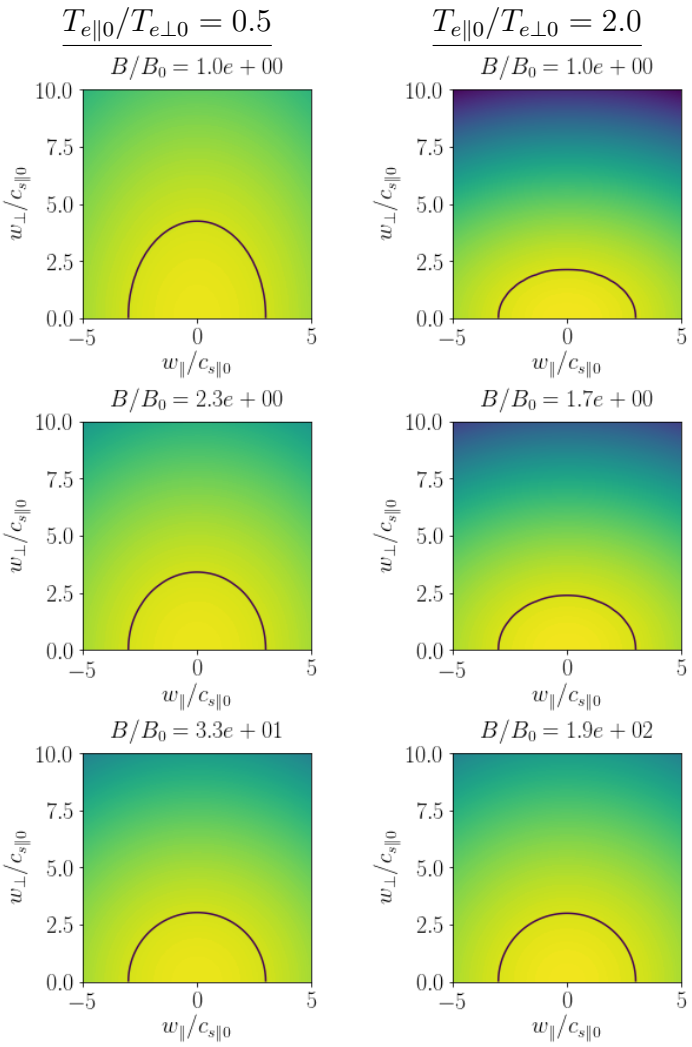

Figure 6.3: Electron VDF in the velocity plane at three different spatial locations. The black solid lines represent curves of $f_e = const$. Results are for $T_{i0}/T_{e\|0} = 0.1$.

behaviour is observed for $T_{e\|0}/T_{e\perp 0} < 1.0$. It is important to notice that the ion temperature remains isotropic in this region, since the ambipolar potential profile by itself is not an anisotropy generation mechanism. The evolution of the IVDF in the initial region is plotted in Figure 6.4, where it is shown how the increase/decrease of the ion temperature is a direct effect of the electric potential gradient in this region.

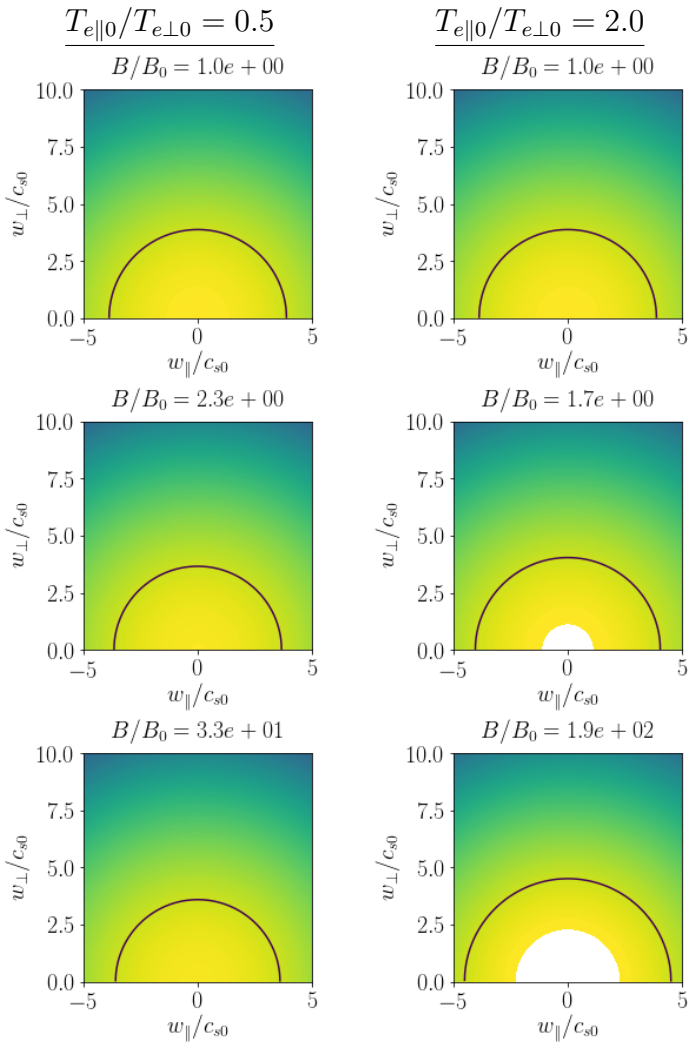

Figure 6.4: Ion VDF in the velocity plane at three different spatial locations. The black solid lines represent curves of $f_i = const$. Results are for $T_{i0}/T_{e\parallel 0} = 0.1$.

6.2.2 Macroscopic plasma response

The previous subsection has shown the kinetic effects responsible for the variation of the main plasma properties along the convergent MN, when the EVDF is postulated as bi-Maxwellian at the upstream source. From a "fluidic" macroscopic point of view, it is possible to study the plasma response by analyzing the plasma momentum equation (4.28).

Figure 6.5 shows the contribution to the total electron and ion momentum of

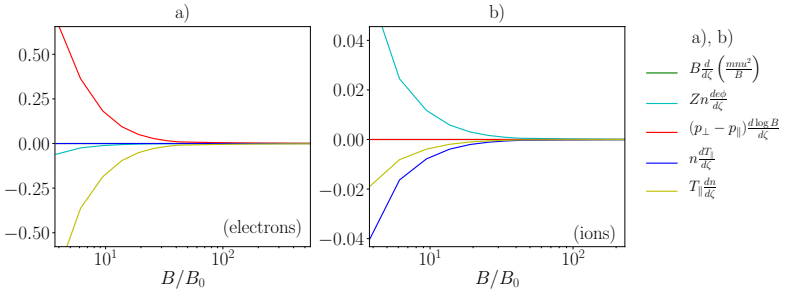

Figure 6.5: Relative contribution for electrons (left) and ions (right) of the different terms of the momentum equation. Units in vertical axes are arbitrary. Results are for $T_{i0}/T_{e\|0} = 0.1$ and $T_{e\|0}/T_{e\perp 0} = 0.5$.

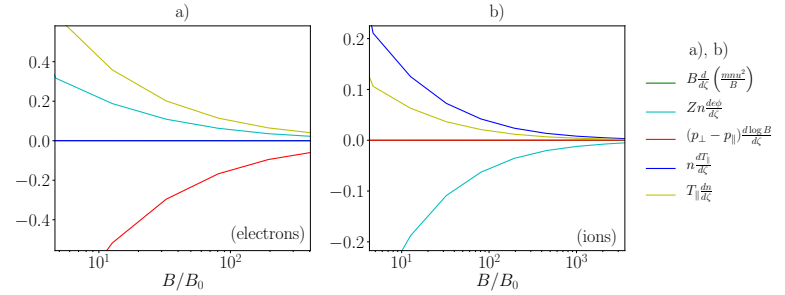

Figure 6.6: Relative contribution for electrons (left) and ions (right) of the different terms of the momentum equation. Units in vertical axes are arbitrary. Results are for $T_{i0}/T_{e\|0} = 0.1$ and $T_{e\|0}/T_{e\perp 0} = 2.0$.

the different terms in equation (4.28), for $T_{e\|0}/T_{e\perp 0} = 0.5$. Regarding electrons, the anisotropic term of the pressure tensor $n(T_\perp - T_\|)d\ln B/dz$, which is not zero anymore, is balanced with a strong density gradient, and a small electric potential gradient for the high anisotropic cases. Ions see the effect of the anisotropic EVDF by means of the developed density gradient and electric potential gradient. Although these two have opposite signs, an additional gradient is needed to balance the ion momentum equation, which is assumed by the parallel ion temperature (see Figure 6.5(b)). The perpendicular ion temperature suffers the same variation than the parallel ion temperature, maintaining $T_{i\perp} \simeq T_{i\|}$ in this upstream region. Finally, Figure 6.6 shows the contribution of the different terms to the momentum equation for $T_{e\|0}/T_{e\perp 0} = 2.0$. In contrast with the case where $T_{e\|0}/T_{e\perp 0} = 0.5$, here the "isotropization" effect is longer, and needs a higher gradient of the magnetic field in order to be completed. An anisotropic EVDF with $T_{e\perp 0} > T_{e\|0}$ has higher

electron magnetic moments than an EVDF with $T_{e\perp 0} < T_{e\parallel 0}$, and the larger the magnetic moment of the particle, the "faster" (spatially) will be the energy transfer to the parallel direction due to the magnetic mirror effect.

6.3 Divergent model

The convergent-divergent model developed in the previous section has shown that the initially anisotropic EVDF becomes isotropic as B/B_0 increases, and therefore the divergent side of the expansion is barely affected by the initial shape of the EVDF upstream. Since this isotropization is directly linked to the convergent character of the MN, the results can not be extrapolated to an only divergent MN. In order to study this feature, a divergent MN model, which considers fluid cold ions and bi-Maxwellian electrons has been developed. The model is analogous to the one of Section 3.4.1, but with a bi-Maxwellian EVDF. The dimensionless parameters which govern the expansion are the ion Mach number defined as

$$M_0 = \frac{u_i}{\sqrt{T_{e\parallel *}/m_i}}, \tag{6.5}$$

the ion to electron mass ratio m_i/m_e, and the electron temperature anisotropy ratio $T_{e\parallel *}/T_{e\perp *}$. The solution shows that due to the large confinement of the electrons, $n_{e*} \simeq n_{e0}$, $T_{e\parallel *} \simeq T_{e\parallel 0}$ and $T_{e\perp *} \simeq T_{e\perp 0}$, so the reference magnitudes will be treated as the source magnitudes in the rest of the document.

Since the most interesting cases for this Thesis are for $T_{e\parallel 0}/T_{e\perp 0} < 1$, solutions have been obtained for $T_{e\parallel 0}/T_{e\perp 0} = 1.0$, $T_{e\parallel 0}/T_{e\perp 0} = 0.95$ and $T_{e\parallel 0}/T_{e\perp 0} = 0.75$. Figure 6.7 shows the evolution of the main plasma properties along the expansion. Contrary to what happens in the previous convergent-divergent model, the profile of the electric potential is always monotonically decreasing. As Figure 6.7(a) illustrates, as $T_{e\parallel 0}/T_{e\perp 0}$ decreases, the main acceleration region occurs in a smaller magnetic field gradient, but the total plasma potential drop against the mean electron temperature at the source remains unchanged. The main reason behind this phenomenon is that in an anisotropic EVDF, the mean value of the electrons magnetic moment is higher, which implies that the energy transfer from the perpendicular to the parallel direction takes place in a smaller magnetic field gradient. Notice

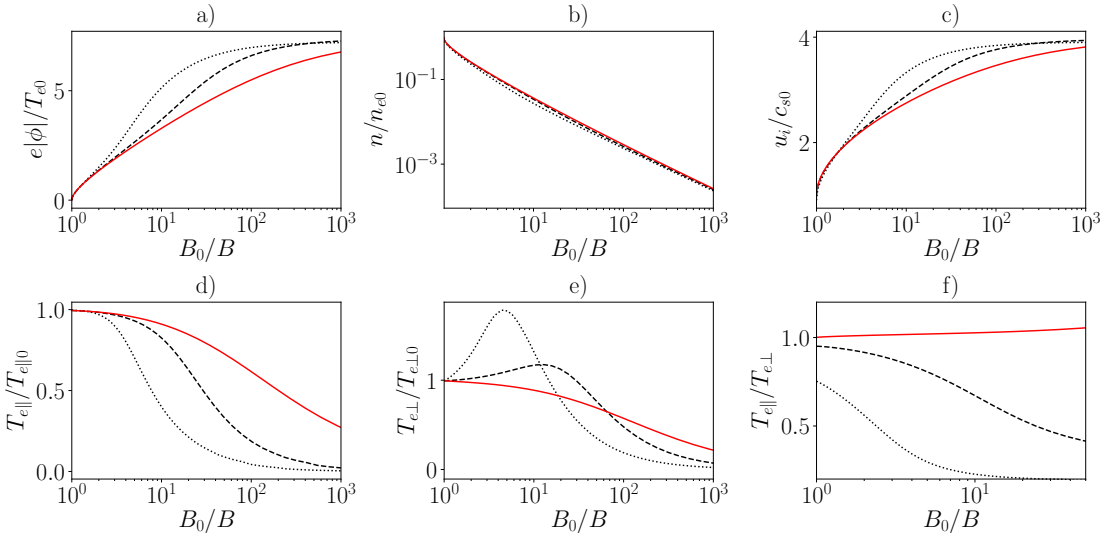

Figure 6.7: Evolution of main plasma properties along the divergent side of the expansion. Cases are for $T_{e\parallel 0}/T_{e\perp 0} = [0.75$, (·····), 0.95 (- - -), and 1.0 (▬)].

that a small degree of anisotropy at the plasma source is already enough to modify significantly the plasma potential profile.

Plasma density is shown in Figure 6.7(b); since the main acceleration region is shorter, the density drops "faster" than in the isotropic case. The effect on the ion velocity, plotted in Figure 6.7(c), is analogous to the electric potential profile.

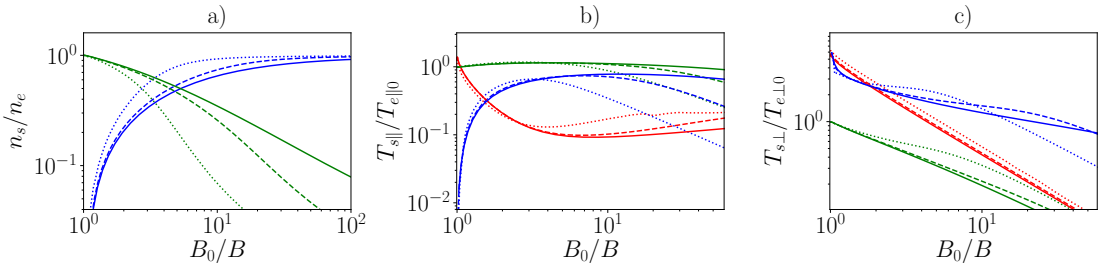

Figure 6.8: Contribution of the different electron subpoplations to the main electron properties. Reflected (green), doubly-trapped (blue) and free (red). Cases are for $T_{e\parallel 0}/T_{e\perp 0} = [0.75$, (dotted), 0.95 (dashed), and 1.0 (solid)].

The subplots of the second row of Figure 6.7 show the evolution of the electron temperatures along the expansion. As it was expected, the "isotropization" effect is no longer present, and the plasma response is exactly the opposite. The parallel electron temperature decreases "faster" than in the isotropic case, and the

perpendicular component increases in the near region, reaches a maximum, and then decreases.

In order to understand the evolution of the parallel and perpendicular electron temperatures, it is crucial to analyze separately the electron temperatures of the different types of particles (reflected, doubly-trapped and free). Figure 6.8 shows the electron density, parallel and perpendicular temperatures of each subpopulation. In the isotropic case (solid lines), the parallel temperature of the doubly-trapped subpopulation increases initially, while the perpendicular component decreases. When anisotropy is present, there is an additional kinetic feature which counteracts the decrease of perpendicular temperature: the eccentricity of the curves $f_e = const$ increases. This effect is seen as a decrease of the perpendicular temperature gradient, as it is shown in Figure 6.8(c). The same rationale can be applied to the reflected subpopulation.

The perpendicular temperature of each subpopulation decreases along the expansion as a due to the inverse magnetic mirror effect. However, an increase is observed in the total perpendicular electron temperature of Figure 6.7(e), which is a result of weighting the temperatures of the different subpopulations (reflected, doubly-trapped and free) with their respective densities. Figure 6.8(a) shows that the electron density is governed by reflected particles at the upstream source, and then by the doubly-trapped subpopulation. In the anisotropic case, the location where the doubly-trapped subpopulation dominates is closer to the magnetic throat. Moreover, the peak on the perpendicular electron temperature profile can exceed its value at the source, since the mean perpendicular temperature of the doubly-trapped subpopulation is larger than the mean perpendicular temperature of the whole electron species.

To illustrate the evolution of the EVDF along the expansion, Figure 6.9 shows the EVDF at three different values of B_0/B, for $T_{e\parallel 0}/T_{e\perp 0} = 0.75$, and for $T_{e\parallel 0}/T_{e\perp 0} = 1.0$. In the first case, the curves of $f_e = const$ are initially elliptical due to the anisotropy of the EVDF. As B decreases, the eccentricity of these ellipses increases (without taking into account the void regions). This effect is only present in initially anisotropic EVDFs.

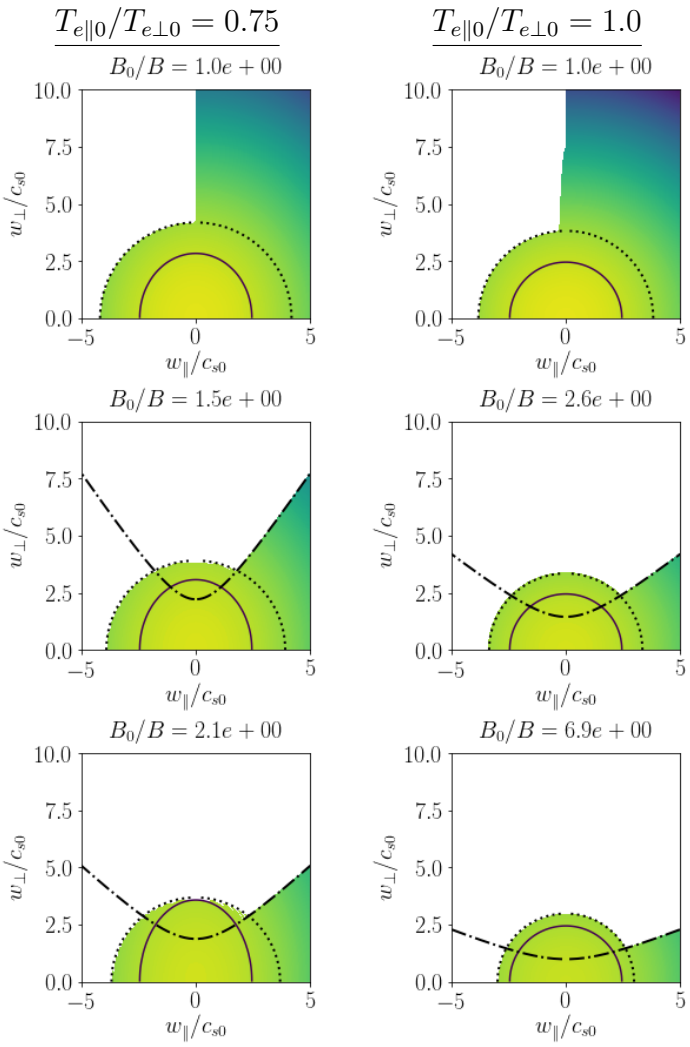

Figure 6.9: Electron VDF in the velocity plane at three spatial locations close to the magnetic throat. First column is for $T_{e\|0}/T_{e\perp 0} = 0.75$ and second column for $T_{e\|0}/T_{e\perp 0} = 1.0$. The solid lines represent curves of $f = const.$

6.4 Summary of results and final discussion

We have studied the expansion of an anisotropic EVDF in a MN. The problem is of high interest, since in some plasma sources, such as the ECR, a high level of anisotropy can be achieved.

Two models have been studied: a convergent-divergent fully kinetic model and an only-divergent hybrid model. The convergent-divergent model has been solved

for $T_{e\|0}/T_{e\perp 0} = [0.5 - 2.0]$. There is an "isotropization" of the EVDF in the convergent region. In the velocities space, the EVDF is re-distributed along circumferences as B increases, transferring energy from the parallel component to the perpendicular direction due to the magnetic mirror effect. This phenomenon takes place before the "void" regions start to be noticeable, and results in an isotropization of the EVDF. Particularly, the perpendicular electron temperature increases or decreases to match the parallel component.

The isotropization of the EVDF is directly linked to the magnetic field gradient. For the cases with $T_{e\perp 0} > T_{e\|0}$, this feature takes place in a smaller gradient; the larger the magnetic moment of the particles, the more sensible they are to magnetic field strength variations. Regarding the main plasma properties, density and electric potential gradients are also developed in the region where the EVDF is becoming more isotropic. These additional gradients ensure that from a macroscopic point of view, the total momentum of electrons is perfectly conserved. Finally, ions see the the electric potential gradients developed in the convergent region. An increase/decrease of the ion temperature (both in the parallel and perpendicular components) is observed due to this effect, remaining isotropic throughout all this region, where the magnetic mirror effect is still not noticeable.

In an only divergent expansion, the opposite behaviour has been observed; there is an increase of the anisotropic electron temperature ratio as B decreases. The perpendicular electron temperature increases, while the parallel component decreases "faster" than in the isotropic case.

To conclude, this study has shown that an anisotropic EVDF expanding in a MN, does not conserve its anisotropic temperature ratio, since due to the magnetic mirror effect, the EVDF is re-distributed in circumferences in the velocities space, regardless its initial shape. This kinetic effect results in an isotropization of the EVDF in the convergent expansion, and in an increase of the electron temperature anisotropy in the divergent side.

As a final remark, it must be said that several limitations have been encountered when solving the entire models. In the case of the convergent-divergent kinetic model, it has not been possible to obtain solutions for $B_0/B_M > 10^{-3}$ when $T_{e\perp 0} \neq T_{e\|0}$, which has limited the study presented here. Unfortunately, the study is incomplete since numerical convergence has been impossible to achieve in relevant parametric regions. Therefore, other numerical algorithms must be tested in

future investigations, in order to achieve a better numerical convergence. The hybrid divergent model, as it is formulated right now, also presents some limitations. The initial guess on the plasma potential profile needed to initiate the numerical algorithm needs to be very close to the solution itself. However, as it has been shown in the previous section, the solution varies significantly when introducing a weak anisotropy in the EVDF. The code, as it is right now, does not solve properly the model if the initial guess is too far away from the solution. Finally, the fact that the doubly-trapped electron population is anisotropic is limiting the utility of this study, since the steady-sate model has no means to determine which is exactly its distribution function.

CHAPTER

SEVEN

Conclusions and future work

This chapter outlines the main contributions of this Thesis and proposes future lines of research.

7.1 Review and main contributions

The main goal of this Thesis was to contribute to the understanding of the physical phenomena involved in MN thrusters, such as the Helicon Plasma Thruster (HPT) or the Electron Cyclotron Resonance (ECR) Thruster. Particularly, this Thesis has been focused on the electron and ion thermodynamics along the nozzle. On the theoretical side, the kinetic steady-state paraxial model developed previously by Martínez Sánchez *et al.* [83] has allowed to study fundamental physical phenomena related to the plasma behaviour along a MN. The model has been extended and re-formulated to consider different plasma conditions at the upstream source and different MN topologies, which is essential to reproduce the real plasma conditions in existing MN thrusters. On the experimental side, different diagnostics have been used to characterize the main plasma properties along the MN of an ECR thruster; the research has been focused on studying plasma diamagnetism, ion acceleration and electron cooling, among others. The work performed in this Thesis has allowed to compare the kinetic model of Ref. [83] with real experimental data. Since this Thesis has been carried out in two different research centers, the results are divided into two parts: (i) experimental research of ONERA's ECR thruster, (ii) modelling of MN expansions at EP2 group. The main contributions are detailed below.

7.1.1 Experimental research along the MN of an ECR Thruster

The MN of two ECR thruster prototypes (permanent magnet and solenoid ONERA's ECR thrusters) has been studied by means of different plasma diagnostics. The main contributions are related to two different topics, which correspond to Chapters 2 and 3, respectively.

In Chapter 2, the induced magnetic flux of the permanent magnet ECR thruster has been measured for the first time by means of a non-intrusive diamagnetic loop, whose principle of operation is based on the induction Faraday's law. This research presents an innovative procedure to estimate the mean perpendicular pressure inside MN thrusters. The main contributions are complied as follows.

- It has been demonstrated that the integration of the diamagnetic loop signal during the thruster shutdown allows to estimate the mean perpendicular electron pressure inside the ECR thruster. This technique is potentially of high interest, due to the difficulties of measuring plasma properties inside thruster sources, and can provide useful information regarding the plasma conditions at the thruster exit.

- The calibration procedure has been described, and the main sources of error have been identified. Particularly, the influence of eddy currents in the thruster walls has been found to be crucial. The effect of eddy currents on different thruster wall materials has been addressed, identifying graphite as the best option for implementing this diagnostic without modifying significantly the thruster performance.

- The diamagnetic loop detects large plasma oscillations during operation. While in the present set-up, this involves uncertainty in the measurements, in a different configuration it could help to characterize the transient phenomena during operation.

- A parametric study of the induced magnetic flux at different operating conditions has been performed. It has been found that it increases with the applied power and presents a maximum in the mass flow rate range. These trends agree well with the direct magnetic thrust measurements performed by Vialis

et al. in Ref. [130] in the same ECR thruster. This result is very relevant, since diamagnetic flux and magnetic thrust are directly related.

- By means of a plasma model, one can relate the integrated magnetic flux with the mean perpendicular electron pressure inside the plasma source. As an example, two models (1D and 2D) have been implemented, illustrating the limitations of using a simple 1D model. Being able to estimate the mean perpendicular electron temperature inside the thruster source by means of a non-intrusive diagnostics constitutes a substantial progress in the experimental research field.

- The influence of the loop radii has been illustrated by testing two loops with significantly different dimensions. It has been shown that the smallest loop provides a better estimate of the mean perpendicular pressure inside the source, since the 2D effects of the induced magnetic field in the plume can be disregarded.

Continuing with the experimental research, the plume of ONERA's ECR thruster has been characterized by means of different diagnostics: a cylindrical Langmuir probe for estimating the electron density, plasma potential and mean temperature along the nozzle, Laser Induces Fluorescence for measuring the mean ion kinetic energy and a Faraday gridded probe to obtain angular profiles of current density. The mean plasma properties of the two thrusters mentioned above have been characterized at different operating conditions (different mass flow rates). In Chapter 3, the experimental set-up is explained in detail, as well as the main results and discussion. The main outcomes of this experimental research are summarized below.

- For equal absorbed measured absorbed power and different mass flow rates, the plasma potential, electron density and electron temperature profiles have been obtained. The collection of these data was essential to understand the plasma behaviour along the MN and to further compare with theory. The obtained profiles were reproduced with high repeatability.

- An effective electron cooling along ONERA's ECR thruster MN has been measured for the first time. Interestingly, the electron cooling trends found

in the permanent magnet thruster differ from the ones found in the solenoid thruster. An effective and constant polytropic coefficient of 1.23 ± 0.02 was found in the permanent magnet version, while two clearly different coefficients (1.55 and 1.17) were identified in the case of the solenoid thruster. Although the spatial region where the measurements were obtained was the same, the MN topologies were different, being larger for the permanent magnet thruster. The deviation from simple cooling laws is more visible downstream (where the magnetic field has dropped more) in the expansion.

- The LIF set-up has allowed to measure the ion velocity profile close to the thruster exit, and even inside the ECR source. However, very close to the magnets, the Zeeman splitting effect is visible and it can corrupt the measurements. Velocities up to 16 km/s have been measured.

- The most innovative part of this research has been to combine the measurements from the Langmuir Probe and from the LIF set-up to obtain complete profiles of the plasma potential, assuming the total ion energy is conserved. By overlapping these curves in the region where they operated simultaneously, one can reconstruct the complete plasma potential profile, which is of high interest to compare with theoretical 1D models.

- The data from the angular scans of current density obtained with the Faraday probe have been used to estimate the mass utilization efficiency at each operating conditions, which has helped to interpret the results.

7.1.2 Magnetic Nozzle Modelling at EP2

The paraxial model developed my Martínez Sánchez *et al.* [83], extended to include different MN configurations and upstream plasma conditions, has been the basis of the theoretical research carried out in this Thesis. The kinetic formulation of ions and electrons allows to consider magnetic mirroring and electric potential barriers, which are two of the main principles of operation of MN. Furthermore, a finite potential drop is obtained as part of the solution, and an effective collisionless electron cooling is developed along the expansion. For all this, the model of Ref. [83] represents a step forward in MN modelling, and allows to perform multiple parametric studies varying the boundary conditions of the problem.

The experimental data of the main plasma properties along the ECR MN were compared to a paraxial steady-state model similar to the one of Ref. [83], with two main differences: the magnetic field is fully divergent, and ions were modelled as a fluid species. Chapter 3 details the comparison for different thruster operating conditions; the main contributions are listed as follows.

- A least-square method was implemented to compare the experimental data with the aforementioned model. The main difficulty was to estimate the real sonic transition in the nozzle, since the plasma was created in a fully divergent magnetic field. Since the model assumes an initial Mach number, the least-square method was implemented to minimize the total error between the experimental data and the model prediction, estimating a possible sonic transition of the plasma flow.

- The plasma potential, ion velocity and density profiles agree well with the model. However, the highest error was found in the electron temperature; concretely, for the lower mass flow rates. This discrepancy is probably due to anisotropic effects, since at lower mass flow rates, a higher anisotropy is expected. As well, the uncertainty regarding the computation of the electron temperature by means of Langmuir Probe measurements is quite large (20 %).

- In this work, we advanced that the sonic transition of the plasma flow was probably shifted from the maximum magnetic field strength location. Our statement was based on the comparison of the experimental ion velocity profiles with the model predictions. This hypothesis was experimentally confirmed later by Collard *et al.* [40].

Apart from comparing with experimental data, the model formulated in Ref. [83] has been complemented and extended to investigate further and understand fundamental kinetic aspects of MN expansions. The main studies can be divided into two main parts; first, the macroscopic manifestation of the kinetic effects (Chapter 4), and then, the non-Maxwellian character of EVDF at the plasma reservoir and its impact on the plasma expansion (Chapters 5 and 6).

Regarding the first part, the main contributions of the study are drawn below.

- The macroscopic expression of the magnetic mirror effect has been discussed, showing that it is only relevant when a large anisotropy is developed.

- Contrary to intuition, it has been demonstrated that macroscopically, the magnetic mirror effect is very mild on electrons, since they do not develop anisotropy until very far downstream. In contrast, ions are strongly affected in the convergent region, being larger the effect for hot ions.

- Ions have been formulated as mono-energetic and Maxwellian upstream. The plasma response is very similar, and differences have only been found in the second and third order fluid quantities.

- Since electrons are (macroscopically) barely affected by the magnetic mirror effect, there is an almost perfect balance between the ambipolar potential field and he pressure gradients.

- In an attempt to find a closure to the electron fluid equation hierarchy based on the kinetic solution, the contribution of the heat fluxes along the expansion has been investigated. It has been found that these fluxes are dominant along all the expansion, and in general larger than the convective thermal energy flows. Although this study has enabled to identify the relevance of the diffusive and convective terms in the energy equation, it has not been possible to find a unique closure that fairly reproduces the plasma behaviour.

- It has been demonstrated that a constant diffusion/convection thermal energy flux is equivalent to the commonly used polytropic law. The first one is more useful, since it closes the fluid equation hierarchy in the energy level.

- The physical meaning of the collisionless heat fluxes has been discussed, showing that without evaluating the four-order terms, we can only attribute them a mathematical connotation.

- Useful parametric laws relating the downstream plasma properties with the model parameters (ion to electron mass ratio and ion to electron source temperature ratio) have been derived, which allow to predict the main expansion properties without solving the entire model.

The model has been extended to expand non-Maxwellian EVDFs. The study is of high interest, since it is crucial to understand how the conditions at the plasma reservoir affect the MN expansion and the downstream properties. Chapters 5 and 6 are devoted to explore an EVDF with a small fraction of hot electrons, and an EVDF with a bi-Maxwellian anisotropic distribution, respectively. In the first case, the main contributions are related to the total potential drop of the nozzle and the study of the hot electrons thermodynamics. The forward upstream EVDF has been formulated as two Maxwellian distributions with disparate temperatures, and the plasma response is governed by the density and temperature ratio of hot/cold electrons upstream. The main conclusions of this investigation are the following:

- The formation of a quasi-double-layer (quasi-neutral) has been studied as a function of the model parameters. It has been shown that its location is determined by the hot to cold electrons density ratio at the source α_0, while the temperature ratio θ_0 mainly increases its strength. Results are coherent and consistent with a previous work by Martínez Sánchez and Ahedo of a three species fluid model (with Maxwellian electrons) [5].

- The cold electron species has been found to be a completely isothermal and confined species. The hot electron species governs the electron cooling along the expansion. It has been shown that the total potential drop $e|\phi_\infty|/T_{h0}$ determines the thermodynamics of the hot electrons. For the cases where this parameter is below its value in a single ion-electron plasma, the contribution of free particles to the hot electron species modifies its behaviour; they become much more anisotropic in the convergent and divergent expansion (the magnetic mirror effect is no more negligible macroscopically).

- Since $e|\phi_\infty|/T_{h0}$ is a key parameter to understand the hot electrons thermodynamics, a parametric study of its value as a function of the *new* model parameters has been performed. It has been shown that for $\alpha_0 < 0.2$, the total potential drop scales basically with the hot electrons temperature at the source. However, there is a parametric domain where the total potential drop is lower. These cases are the most interesting ones, since in real devices, hot electrons constitute only a small fraction of the electrons source density. A large anisotropy is developed close to the magnetic throat, which is a direct effect of the magnetic mirror effect.

- For the same plasma energy at the source, it has been identified that with 3 % of hot electrons at the source, the specific impulse of the nozzle is maximized. This result could be useful for MN electric propulsion devices which generate two electron distributions at the source, although in reality, this parameter is difficult to control.

Finally, the formulation of the model with bi-Maxwellian anisotropic electrons at the source has been presented. This preliminary study constitutes the first attempt to model MN expansions of anisotropic EVDFs within the EP2 group. The main goal was to investigate how electrons anisotropy influences the plasma expansion dynamics. Two models have been analyzed; a fully kinetic convergent-divergent model, where ions were treated as Maxwellian and electrons as bi-Maxwellian with different parallel and perpendicular temperatures, and an only divergent hybrid model with fluid ions and bi-Maxwellian kinetic electrons. In the following lines, the main conclusions regarding this study are outlined.

- In the convergent-divergent model, there is an "isotropization" effect on the convergent side of the expansion, where the perpendicular temperature increases or decreases to match the parallel component as B increases. This isotropization is a direct kinetic effect of magnetic mirroring in initially non-Maxwellian distributions.

- In the divergent model, the effect is the opposite: the initial electron anisotropy temperature ratio increases. The acceleration region is shorter compared to the isotropic case when the perpendicular electron source temperature is larger than the parallel component.

- Numerical limitations have been found when solving the model, which has limited the parametric analysis presented here. Other different numerical algorithms must be tested in order to achieve a better numerical convergence.

To conclude, this Thesis has contributed to the understanding of the fundamental physical phenomena that govern MN expansions, reaffirming the need for experimental and theoretical findings and investigations to be fully aligned. From the theoretical point of view, this Thesis has contributed to understand the macroscopic expression of the kinetic effects (magnetic mirror and ambipolar plasma potential

barriers), and the effects of expanding non-Maxwellian EVDFs. On the experimental side, a new diagnostic has been developed to measure the induced magnetic flux inside an ECR thruster, which has allowed to estimate the mean perpendicular plasma pressure. The mean plasma properties have been characterized along the MN by means of electrostatic probes and optical diagnostics, and compared with the paraxial steady-state model studied here.

7.2 Future work

The ultimate goal of all scientific research must be to cross-check the theoretical assumptions with experimental validation. In this regard, a roadmap for future work is proposed below.

On the theoretical side, the future work must be oriented in two directions: first, the kinetic model must be implemented in 2D and 3D electron fluid models, in order to perform more complete and rigorous simulations of MN plasma thrusters. The most challenging part is precisely the 2D character of the solution itself; one can not solve independently each magnetic streamline (unless the plasma is assumed fully magnetized, which is unpractical). The current-free assumption is a global boundary condition, which should be formulated to consider each section of the plasma plume. Ideally, the kinetic model should be implemented and solved as part of the 2D, 3D models. However, a limited intermediate step would be to apply fluid closure laws to the electron fluid equation hierarchy of 2D and 3D models, based on the results of this Thesis.

Apart from the implementation in 2D and 3D codes, additional work should be done regarding the formulation of the kinetic model. The nature of the doubly-trapped electron population is still unclear. A time-dependent, collisional model should be implemented in order to study not only the shape of the EVDF, but also the existence regions of doubly-trapped particles in the velocities phase space. In this regard, the research of Sánchez-Arriaga *et al.* showed that these regions could be populated up to 25 % only due to non-stationary effects of the electric potential [110]. However, collisions must be taken into account to properly model the fulfilment of these regions.

The postulate of non-Maxwellian EVDFs at the plasma source has re-opened uncertainties regarding the formulation of the doubly-trapped and reflected elec-

trons. The present model considers they have the same functional dependence as the source electrons. This assumption is plausible for a Maxwellian EVDF, but becomes meaningless for a bi-Maxwellian (anisotropic) assumption, since one should understand that since this population is isolated from the source, electrons in these regions would eventually collide and isotropize. Postulating the doubly-trapped electrons with a different EVDF is not particularly difficult, and should be the first change to be implemented in the anisotropic model. This implementation is specially important regarding the divergent MN model.

Finally, from the experimental point of view, we outline three important missing studies. First, plasma conditions at the thruster exit should be properly characterized since as we have seen here, the assumption of the ion and electron VDFs at the "upstream" source are crucial to determine the MN performance. In this regard, non-intrusive diagnostics are recommended, such as Thomson scattering, or laser induced measurements. Second, this Thesis has characterized only the center line of the MN. 3D set-ups should be implemented in order to have a complete map of the main plasma properties. Last, experiments should be oriented to measure anisotropic plasma properties, along the MN and in the plasma source. In this Thesis, we have been able to estimate the mean perpendicular electron pressure at the source, but it is insufficient to provide information about the EVDF anisotropy.

Bibliography

[1] Ane Aanesland, Christine Charles, MA Lieberman, and RW Boswell. Upstream ionization instability associated with a current-free double layer. *Physical review letters*, 97(7):075003, 2006.

[2] Milton Abramowitz and Irene A Stegun. *Handbook of mathematical functions: With formulas, graphs, and mathematical tables*, volume 55. Courier Corporation, 1965.

[3] J.C. Adam, J.P. Boeuf, N. Dubuit, M. Dudeck, L. Garrigues, D. Gresillon, A. Heron, G.J.M. Hagelaar, V. Kulaev, N. Lemoine, et al. Physics, simulation and diagnostics of Hall effect thrusters. *Plasma Physics and Controlled Fusion*, 50:124041, 2008.

[4] European Space Agency. Technology readiness level. https://sci.esa.int/web/future-missions-department/-/56048-technology-readiness-levels.

[5] E. Ahedo. Double-layer formation and propulsive assessment for a three-species plasma expanding in a magnetic nozzle. *Physics of Plasmas*, 18:033510, 2011.

[6] E. Ahedo, S. Correyero, J. Navarro-Cavallé, and M. Merino. Macroscopic and parametric study of a kinetic plasma expansion in a paraxial magnetic nozzle. *Plasma Sources Science and Technology*, 29(4):045017, (submitted for publication).

[7] Eduardo Ahedo. Plasmas for space propulsion. *Plasma Physics and Controlled Fusion*, 53(12):124037, 2011.

[8] Eduardo Ahedo and Manuel Martínez Sánchez. Theory of a Stationary Current-Free Double Layer in a Collisionless Plasma. *Physical Review Letters*, 103(13):1–4, 2009.

[9] Eduardo Ahedo and Mario Merino. Two-dimensional supersonic plasma acceleration in a magnetic nozzle. *Physics of Plasmas*, 17(7):073501, 2010.

[10] Eduardo Ahedo and Mario Merino. On plasma detachment in propulsive magnetic nozzles. *Physics of Plasmas*, 18(5):053504, 2011.

[11] H. Aikawa. The measurement of the anisotropy of electron distribution function of a magnetized plasma. *Journal of the Physical Society of Japan*, 40(6):1741–1749, 1976.

[12] B Albertazzi, A Ciardi, M Nakatsutsumi, T Vinci, J Béard, R Bonito, J Billette, M Borghesi, Z Burkley, SN Chen, et al. Laboratory formation of a scaled protostellar jet by coaligned poloidal magnetic field. *Science*, 346(6207):325–328, 2014.

[13] Hiroshi Amemiya, Hitoshi Oyama, and Yuichi Sakamoto. Experiment on the anisotropy of electron temperature in ecr plasma. *Journal of the Physical Society of Japan*, 56(7):2401–2412, 1987.

[14] A Ando, M Inutake, K Hattori, M Shibata, and Y Kasashima. ICRF heating and plasma acceleration with an open magnetic field for the advanced space thruster. *Fusion science and technology*, 51(2T):72–74, 2007.

[15] Y. Arakawa and A. Sasoh. Steady-state permanent magnet magnetoplasmadynamic thruster. *Journal of Propulsion and Power*, 5:301–304, 1989.

[16] Alexey V. Arefiev and Boris N. Breizman. Magnetohydrodynamic scenario of plasma detachment in a magnetic nozzle. *Physics of Plasmas*, 12(4):043504, 2005.

[17] A.V. Arefiev and B.N. Breizman. Ambipolar acceleration of ions in a magnetic nozzle. *Physics of Plasmas*, 15(4):042109, 2008.

[18] C Barué, M Lamoureux, P Briand, A Girard, and G Melin. Investigation of hot electrons in electron-cyclotron-resonance ion sources. *Journal of Applied Physics*, 76(5):2662–2670, 1994.

[19] SN Bathgate, MMM Bilek, and DR Mckenzie. Electrodeless plasma thrusters for spacecraft: a review. *Plasma Science and Technology*, 19(8):083001, 2017.

[20] O.V. Batishchev. Minihelicon plasma thruster. *Plasma Science, IEEE Transactions on*, 37(8):1563–1571, 2009.

[21] E Bickford Hooper, Barry W Stallard, and Michael A Makowski. Whistler wave driven plasma thruster. In *AIP Conference Proceedings*, number 3 in 271, pages 1419–1424. AIP, AIP, 1993.

[22] S Boivin, X Glad, L Latrasse, A Sarkissian, and L Stafford. Probing suprathermal electrons by trace rare gases optical emission spectroscopy in low pressure dipolar microwave plasmas excited at the electron cyclotron resonance. *Physics of Plasmas*, 25(9):093511, 2018.

[23] JH Booske, MJ McCarrick, SR Douglass, JA Paquette, RF Ellis, and WD Getty. Frequency compensation of a diamagnetic loop using a digital data acquisition system. *Journal of Physics E: Scientific Instruments*, 20(6):627, 1987.

[24] Rod W Boswell, Kazunori Takahashi, Christine Charles, and Igor D Kaganovich. Non-local electron energy probability function in a plasma expanding along a magnetic nozzle. *Frontiers in Physics*, 3:14, 2015.

[25] MD Bowden, T Okamoto, F Kimura, H Muta, Kiichiro Uchino, K Muraoka, T Sakoda, M Maeda, Y Manabe, M Kitagawa, et al. Thomson scattering measurements of electron temperature and density in an electron cyclotron resonance plasma. *Journal of applied physics*, 73(6):2732–2738, 1993.

[26] B.N. Breizman, M.R. Tushentsov, and A.V. Arefiev. Magnetic nozzle and plasma detachment model for a steady-state flow. *Physics of Plasmas*, 15:057103, 2008.

[27] Daniel L Brown, Mitchell LR Walker, James Szabo, Wensheng Huang, and John E Foster. Recommended practice for use of faraday probes in electric propulsion testing. *Journal of Propulsion and Power*, 33(3):582–613, 2016.

[28] KTAL Burm, WJ Goedheer, and DC Schram. Mach numbers for gases and plasmas in a convergent-divergent cascaded arc. *Physics of Plasmas*, 6(6):2628–2635, 1999.

[29] R.L. Burton and P.J. Turchi. Pulsed plasma thruster. *J. Propulsion and Power*, 14:716–735, 1998.

[30] F Cannat, T Lafleur, J Jarrige, P Chabert, P-Q Elias, and D Packan. Optimization of a coaxial electron cyclotron resonance plasma thruster with an analytical model. *Physics of Plasmas*, 22(5):053503, 2015.

[31] C. Charles. High density conics in a magnetically expanding helicon plasma. *Applied Physics Letters*, 96(5):051502–051502, 2010.

[32] C. Charles and R. Boswell. Current-free double-layer formation in a high-density helicon discharge. *Applied Physics Letters*, 82(9):1356–1358, 2003.

[33] C. Charles, R.W. Boswell, and M.A. Lieberman. Xenon ion beam characterization in a helicon double layer thruster. *Applied Physics Letters*, 89(26):261503, 2006.

[34] Christine Charles, Rod Boswell, P Alexander, C Costa, Orson Sutherland, Leigh Pfitzner, R Franzen, Jeff Kingwell, A Parfitt, Pierre-Etienne Frigot, et al. Helicon double layer thrusters. In *42nd AIAA/ASME/SAE/ASEE Joint Propulsion Conference & Exhibit*, page 4838, 2006.

[35] G.F. Chew, M.L. Goldberger, and F.E. Low. The boltzmann equation and the one-fluid hydromagnetic equations in the absence of particle collisions. *Proceedings of the Royal Society of London A*, 236:112–118, 1956.

[36] D.L. Chubb. Fully ionized quasi-one-dimensional magnetic nozzle flow. *AIAA Journal*, 10(2):113–114, 1972.

[37] Filippo Cichocki, Adrián Domínguez-Vázquez, Mario Merino, and Eduardo Ahedo. Hybrid 3D model for the interaction of plasma thruster plumes with nearby objects. *Plasma Sources Science and Technology*, 26(12):125008, 2017.

[38] Filippo Cichocki, Mario Merino, and Eduardo Ahedo. A 3d electron fluid model to study magnetic field effects on an expanding plasma thruster plume. In *Space Propulsion Conference 2018*, 00295, Seville, Spain, May 14-18, 2018. Association Aéronautique et Astronautique de France.

[39] S.A. Cohen, X. Sun, N.M. Ferraro, E.E. Scime, M. Miah, S. Stange, N.S. Siefert, and R.F. Boivin. On collisionless ion and electron populations in the magnetic nozzle experiment (MNX). *IEEE Transactions on Plasma Science*, 34(3):792–803, 2006.

[40] TA Collard and BA Jorns. Magnetic nozzle efficiency in a low power inductive plasma source. *Plasma Sources Science and Technology*, 28(10):105019, 2019.

[41] C. S. Corr and R. W. Boswell. High-beta plasma effects in a low-pressure helicon plasma. *Phys. Plasmas*, 14(12):122503, December 2007.

[42] S Correyero, J Jarrige, D Packan, and E Ahedo. Plasma beam characterization along the magnetic nozzle of an ECR thruster. *Plasma Sources Science and Technology*, 28(9):095004, 2019.

[43] Sara Correyero, Mario Merino, Paul-Quentin Elias, Julien Jarrige, Denis Packan, and Eduardo Ahedo. Characterization of diamagnetism inside an ECR thruster with a diamagnetic loop. *Physics of Plasmas*, 26(5):053511, 2019.

[44] Sara Correyero, Jaume Navarro-Cavallé, and Eduardo Ahedo. Expansion of a collisionless magnetized plasma plume with bi-maxwellian electrons. In *52nd Joint Propulsion Conference*, page 5035, Salt Lake City, Utah, July 25-27, 2016. American Institute of Aeronautics and Astronautics.

[45] Sara Correyero Plaza, Julien Jarrige, Denis Packan, and Eduardo Ahedo Galilea. Measurement of anisotropic plasma properties along the magnetic nozzle expansion of an electron cyclotron resonance thruster. In 35^{th} *International Electric Propulsion Conference*, IEPC-2017-437, Atlanta, GA, 2017. Electric Rocket Propulsion Society.

[46] K. Dannenmayer, P. Kudrna, M. Tichy, and S. Mazouffre. Measurement of plasma parameters in the far-field plume of a hall effect thruster. *Plasma Sources Sci. Technol.*, 20(065012), 2011.

[47] C.A. Deline, R.D. Bengtson, B.N. Breizman, M.R. Tushentsov, J.E. Jones, D.G. Chavers, C.C. Dobson, and B.M. Schuettpelz. Plume detachment from a magnetic nozzle. *Physics of Plasmas*, 16(3):033502, 2009.

[48] F. Diaz and R. Chang. The VASIMR rocket. *Scientific American*, 283(5):90–97, 2000.

[49] F.R.C. Diaz, J.P. Squire, R.D. Bengtson, B.N. Breizman, F.W. Baity, and M.D. Carter. The physics and engineering of the VASIMR engine. In *36th AIAA/ASME/SAE/ASEE Joint Propulsion Conference & Exhibit*, AIAA 2000-3756, 2000.

[50] Xuan Tong Ding, Yi Liu, GC Guo, EY Wang, KL Wong, LW Yan, JQ Dong, JY Cao, Y Zhou, J Rao, et al. Observation of internal kink instability purely driven by suprathermal electrons in the hl-1m tokamak. *Nuclear Fusion*, 42(5):491, 2002.

[51] MJ Druyvesteyn and Fi M Penning. The mechanism of electrical discharges in gases of low pressure. *Reviews of Modern Physics*, 12(2):87, 1940.

[52] Paul-Quentin Elias. Advances in the kinetic simulation of the microwave absorption in an ecr thruster. In 35^{th} *International Electric Propulsion Conference*, IEPC-2017-361, Atlanta, GA, 2017. Electric Rocket Propulsion Society, Fairview Park, OH.

[53] WC Feldman, JR Asbridge, SJ Bame, MD Montgomery, and SP Gary. Solar wind electrons. *Journal of Geophysical Research*, 80(31):4181–4196, 1975.

[54] Santo Gammino, Giovanni Ciavola, Luigi G Celona, David Mascali, and Fabio Maimone. Numerical simulations of the ecr heating with waves of different frequency in electron cyclotron resonance ion sources. *IEEE Transactions on Plasma Science*, 36(4):1552–1568, 2008.

[55] Richard Geller. *Electron cyclotron resonance ion sources and ECR plasmas*. CRC Press, 1996.

[56] E. F. Gibbons and D. B. Miller. Experiments with an electron cyclotron resonance plasma accelerator. *AIAA Journal*, 2(1):35–41, January 1964.

[57] VA Godyak and VI Demidov. Probe measurements of electron-energy distributions in plasmas: what can we measure and how can we achieve reliable results? *Journal of Physics D: Applied Physics*, 44(23):233001, 2011.

[58] Amelia Greig, Christine Charles, and Roderick W Boswell. Simulation of main plasma parameters of a cylindrical asymmetric capacitively coupled plasma micro-thruster using computational fluid dynamics. *Frontiers in Physics*, 2:80, 2015.

[59] G. Hairapetian and RL Stenzel. Particle dynamics and current-free double layers in an expanding, collisionless, two-electron-population plasma. *Physics of Fluids B: Plasma Physics*, 3:899, 1991.

[60] Jean Carlos Porto Hernandez and Paul-Quentin Elias. Full-pic simulation of an ecr plasma thruster with magnetic nozzle. In 36^{th} *International Electric Propulsion Conference*, IEPC-2019-232, Vienna, Austria, 2019. Electric Rocket Propulsion Society, Fairview Park, OH.

[61] W. M. Hooke, M. A. Rothman, J. Sinnis, and J. Adam. Temperature and power measurements in a plasma heated by absorption of ion cyclotron waves. *Phys. Fluids*, 8(6):1146, 1965.

[62] E.B. Hooper. Plasma flow resulting from electron cyclotron resonance heating on a magnetic hill. *Physics of Plasmas*, 2:4563, 1995.

[63] Ian H Hutchinson. Principles of plasma diagnostics. *Plasma Physics and Controlled Fusion*, 44(12):2603, 2002.

[64] M. Inutake, A. Ando, K. Hattori, H. Tobari, and T. Yagai. Characteristics of a supersonic plasma flow in a magnetic nozzle. *J. Plasma Fusion Res.*, 78(12):1352–1360, 2002.

[65] R.G. Jahn. *Physics of Electric Propulsion*. Dover, 2006.

[66] J. Jarrige, P.Q. Elias, F. Cannat, and D. Packan. Performance comparison of an ECR plasma thruster using argon and xenon as propellant gas. In *33rd International Electric Propulsion Conference*, Paper 2013-420, Washington D.C., October 7-10, 2013. Electric Rocket Propulsion Society, Fairview Park, OH.

[67] Julien Jarrige, Sara Correyero Plaza, Paul-Quentin Elias, and Denis Packan. Investigation on the ion velocity distribution in the magnetic nozzle of an

ecr plasma thruster using lif measurements. In 35^{th} *International Electric Propulsion Conference*, IEPC-2017-382, Atlanta, GA, 2017. Electric Rocket Propulsion Society, Fairview Park, OH.

[68] Julien Jarrige, Paul-Quentin Elias, Félix Cannat, and Denis Packan. Characterization of a coaxial ecr plasma thruster. In *44th AIAA Plasmadynamics and Lasers Conference, San Diego*, 2013.

[69] June Young Kim, KS Chung, Seongcheol Kim, Jong Hyeon Ryu, Kyoung-Jae Chung, and YS Hwang. Thermodynamics of a magnetically expanding plasma with isothermally behaving confined electrons. *New Journal of Physics*, 20(6):063033, 2018.

[70] June Young Kim, Jae Young Jang, KS Chung, Kyoung-Jae Chung, and YS Hwang. Time-dependent kinetic analysis of trapped electrons in a magnetically expanding plasma. *Plasma Sources Science and Technology*, 28(07LT01), 2019.

[71] A.D. Kodys and E.Y. Choueiri. A critical review of the state-of-the-art in the performance of applied-field magnetoplasmadynamic thrusters. In *41st AIAA Joint Propulsion Conference and Exhibit*, volume 4247, 2005.

[72] G. Krülle, M. Auweter-Kurtz, and A. Sasoh. Technology and application aspects of applied field magnetoplasmadynamic propulsion. *J. Propulsion and Power*, 14(5):754–763, 1998.

[73] K. Kuriki and O. Okada. Experimental study of a plasma flow in a magnetic nozzle. *Physics of Fluids*, 13(9):2262, 1970.

[74] T Lafleur, F Cannat, J Jarrige, PQ Elias, and D Packan. Electron dynamics and ion acceleration in expanding-plasma thrusters. *Plasma Sources Science and Technology*, 24(6):065013, 2015.

[75] T.A. Lafleur, D. Rafalskyi, P. Chabert, and A. Aanesland. Proof-of-concept demonstration of the PEGASES plasma thruster. In *34th International Electric Propulsion Conference*, paper 2015-114, Kobe, Japan, July 6-10, 2015. Electric Rocket Propulsion Society, Fairview Park, OH.

[76] MA Lieberman, C. Charles, and RW Boswell. A theory for formation of a low pressure, current-free double layer. *Journal of Physics D: Applied Physics*, 39(15):3294, 2006.

[77] M.A. Lieberman and A.J. Lichtenberg. *Principles of plasma discharges and materials processing*. John Wiley and Sons, Hoboken, NJ, 2005.

[78] JM Little and EY Choueiri. Electron cooling in a magnetically expanding plasma. *Physical Review Letters*, 117(22):225003, 2016.

[79] JM Liu, JS De Groot, JP Matte, TW Johnston, and RP Drake. Measurements of inverse bremsstrahlung absorption and non-maxwellian electron velocity distributions. *Physical review letters*, 72(17):2717, 1994.

[80] B.W. Longmier, E.A. Bering, M.D. Carter, L.D. Cassady, W.J. Chancery, F.R.C. Díaz, T.W. Glover, N. Hershkowitz, A.V. Ilin, G.E. McCaskill, et al. Ambipolar ion acceleration in an expanding magnetic nozzle. *Plasma Sources Science and Technology*, 20:015007, 2011.

[81] W.M. Manheimer and R.F. Fernsler. Plasma acceleration by area expansion. *IEEE Transactions on Plasma Science*, 29:75–84, 2001.

[82] Manuel Martínez-Sánchez and Eduardo Ahedo. Magnetic mirror effects on a collisionless plasma in a convergent geometry. *Physics of Plasmas*, 18(3):033509, 2011.

[83] Manuel Martínez-Sánchez, Jaume Navarro-Cavallé, and Eduardo Ahedo. Electron cooling and finite potential drop in a magnetized plasma expansion. *Physics of Plasmas*, 22(5):053501, 2015.

[84] D Mascali, L Celona, S Gammino, G Castro, R Miracoli, FP Romano, L Malferrari, F Odorici, R Rizzoli, GP Veronese, et al. An investigation on the formation of suprathermal electrons in a b-min ecr machine and a novel method for their damping. *Plasma Sources Science and Technology*, 22(6):065006, 2013.

[85] M Mausbach and K Wiesemann. An experimental study of the anisotropy of the electron distribution function in an ecr plasma by means of a double retarding field analyser. *Plasma physics and controlled fusion*, 32(4):281, 1990.

[86] Stéphane Mazouffre. Electric propulsion for satellites and spacecraft: established technologies and novel approaches. *Plasma Sources Science and Technology*, 25(3):033002, 2016.

[87] Mario Merino. *Analysis of magnetic nozzles for space plasma thrusters*. PhD thesis, Universidad Politécnica de Madrid, 2013.

[88] Mario Merino and Eduardo Ahedo. Two-dimensional quasi-double-layers in two-electron-temperature, current-free plasmas. *Physics of Plasmas*, 20(2):023502, 2013.

[89] Mario Merino and Eduardo Ahedo. Plasma detachment in a propulsive magnetic nozzle via ion demagnetization. *Plasma Sources Science and Technology*, 23(3):032001, 2014.

[90] Mario Merino and Eduardo Ahedo. Influence of electron and ion thermodynamics on the magnetic nozzle plasma expansion. *IEEE Transactions on Plasma Science*, 43(1):244–251, Jan 2015.

[91] Mario Merino and Eduardo Ahedo. Effect of the plasma-induced magnetic field on a magnetic nozzle. *Plasma Sources Science and Technology*, 25(4):045012, 2016.

[92] Mario Merino and Eduardo Ahedo. Fully magnetized plasma flow in a magnetic nozzle. *Physics of Plasmas*, 23(2):023506, 2016.

[93] Mario Merino and Eduardo Ahedo. Magnetic nozzles for space plasma thrusters. In J. Leon Shohet, editor, *Encyclopedia of Plasma Technology*, volume 2, pages 1329–1351. Taylor and Francis, 2016.

[94] Mario Merino and Eduardo Ahedo. Contactless steering of a plasma jet with a 3D magnetic nozzle. *Plasma Sources Science and Technology*, 26(9):095001, 2017.

[95] Mario Merino, Javier Mauriño, and Eduardo Ahedo. Kinetic electron model for plasma thruster plumes. *Plasma Sources Science and Technology*, 27(3):035013, 2018.

[96] M. Nagatomo. Plasma acceleration by high frequency electromagnetic wave in staticmagnetic field gradient. In *6th Electric Propulsion and Plasmadynamics Conference*, page 660. American Institute of Aeronautics and Astronautics, September 1967.

[97] J Navarro-Cavallé, M Wijnen, P Fajardo, and E Ahedo. Experimental characterization of a 1 kw helicon plasma thruster. *Vacuum*, 149:69–73, 2018.

[98] Jaume Navarro-Cavallé, S. Correyero, and E. Ahedo. Collisionless electron cooling on magnetized plasma expansions: advances on modelling. In 34^{th} *International Electric Propulsion Conference*, paper 2015-117, Kobe, Japan, July 6-10, 2015. Electric Rocket Propulsion Society.

[99] J Noland, O Tarvainen, J Benitez, D Leitner, C Lyneis, and J Verboncoeur. Studies of electron heating on a 6.4 GHz ECR ion source through measurement of diamagnetic current and plasma bremsstrahlung. *Plasma Sources Sci. Technol.*, 20(3):035022, April 2011.

[100] MA Ochando, F Medina, B Zurro, KJ McCarthy, MA Pedrosa, A Baciero, D Rapisarda, JM Carmona, and D Jiménez. Effect of suprathermal electrons on the impurity ionization state. *Plasma physics and controlled fusion*, 48(11):1573, 2006.

[101] C.S. Olsen, M.G. Ballenger, M.D. Carter, F.R. Chang Diaz, M. Giambusso, T.W. Glover, A.V. Ilin, J.P. Squire, B.W. Longmier, E.A. Bering, and P.A. Cloutier. Investigation of plasma detachment from a magnetic nozzle in the plume of the vx-200 magnetoplasma thruster. *Plasma Science, IEEE Transactions on*, 43(1):252–268, 2015.

[102] D. Pavarin, F. Ferri, M. Manente, D. Curreli, Y. Guclu, D. Melazzi, D. Rondini, S. Suman, J. Carlsson, C. Bramanti, E. Ahedo, V. Lancellotti, K. Katsonis, and G. Markelov. Design of 50W helicon plasma thruster. In *31th International Electric Propulsion Conference*, IEPC 2009-205, 2009.

[103] Daniel Pérez-Grande. *Fluid modeling and simulation of the electron population in Hall effect thrusters with complex magnetic topologies*. PhD thesis, Universidad Carlos III de Madrid, Leganés, Spain, 2018.

[104] S. Pottinger, V. Lappas, C. Charles, and R. Boswell. Performance characterization of a helicon double layer thruster using direct thrust measurements. *Journal of Physics D: Applied Physics*, 44(23):235201, 2011.

[105] M. Prioul, A. Bouchoule, S. Roche, L. Magne, D. Pagnon, M. Touzeau, and P. Lasgorceix. Insights on physics of Hall thrusters through fast current interruptions and discharge transients. In *27th International Electric Propulsion Conference, IEPC-01-059*, 2001.

[106] Jesús Ramos, Mario Merino, and Eduardo Ahedo. Three dimensional fluid-kinetic model of a magnetically guided plasma jet. *Physics of Plasmas*, 25(6):061206, 2018.

[107] J.J. Ramos. Dynamic evolution of the heat fluxes in a collisionless magnetized plasma. *Physics of Plasmas*, 10:3601, 2003.

[108] Abdolrahim Rezaeiha and Tony Schönherr. Review of worldwide activities in liquid-fed pulsed plasma thruster. *Journal of Propulsion and Power*, 30(2):253–264, 2014.

[109] B.R. Roberson, R. Winglee, and J. Prager. Enhanced diamagnetic perturbations and electric currents observed downstream of the high power helicon. *Physics of Plasmas*, 18(5):053505, 2011.

[110] Gonzalo Sánchez-Arriaga, Jiewei Zhou, E Ahedo, Manuel Martínez-Sánchez, and Jesús José Ramos. Kinetic features and non-stationary electron trapping in paraxial magnetic nozzles. *Plasma Sources Science and Technology*, 27(3):035002, 2018.

[111] M Schnürer, R Nolte, Th Schlegel, MP Kalachnikov, PV Nickles, P Ambrosi, and W Sandner. On the distribution of hot electrons produced in short-pulse laser-plasma interaction. *Journal of Physics B: Atomic, Molecular and Optical Physics*, 30(20):4653, 1997.

[112] J.C. Sercel. Simple model of plasma acceleration in a magnetic nozzle. In *21st International Electric Propulsion Conference*, volume 1, 1990.

[113] J.C. Sercel. *An experimental and theoretical study of the ECR plasma engine*. PhD thesis, California Institute of Technology, 1993.

[114] JOEL SERCEL. Electron-cyclotron-resonance (ecr) plasma thruster research. In *24th Joint Propulsion Conference*, page 2916, 1988.

[115] Shunjiro Shinohara, Hiroyuki Nishida, Takao Tanikawa, Tohru Hada, Ikkoh Funaki, and Konstantin P Shamrai. Development of electrodeless plasma thrusters with high-density helicon plasma sources. *IEEE Transactions on Plasma Science*, 42(5):1245–1254, 2014.

[116] N. Singh. Current-free double layers: A review. *Physics of Plasmas*, 18(12):122105, 2011.

[117] R. L. Stenzel and J. M. Urrutia. Electron magnetohydrodynamic turbulence in a high-beta plasma. i. plasma parameters and instability conditions. *Phys. Plasmas*, 7(11):4450–4456, November 2000.

[118] X. Sun, S.A. Cohen, E.E. Scime, and M. Miah. On-axis parallel ion speeds near mechanical and magnetic apertures in a helicon plasma device. *Physics of Plasmas*, 12:103509, 2005.

[119] X. Sun, A.M. Keesee, C. Biloiu, E.E. Scime, A. Meige, C. Charles, and R.W. Boswell. Observations of ion-beam formation in a current-free double layer. *Physical Review Letters*, 95:025004, 2005.

[120] K. Takahashi, C. Charles, R. Boswell, W. Cox, and R. Hatakeyama. Transport of energetic electrons in a magnetically expanding helicon double layer plasma. *Applied Physics Letters*, 94(19):191503, 2009.

[121] K. Takahashi, T. Lafleur, C. Charles, P. Alexander, R.W. Boswell, M. Perren, R. Laine, S. Pottinger, V. Lappas, T. Harle, et al. Direct thrust measurement of a permanent magnet helicon double layer thruster. *Applied Physics Letters*, 98:141503, 2011.

[122] Kazunori Takahashi and Akira Ando. Laboratory observation of a plasma-flow-state transition from diverging to stretching a magnetic nozzle. *Physical Review Letters*, 118(22):225002, 2017.

[123] Kazunori Takahashi, Christine Charles, Rod Boswell, and Akira Ando. Performance improvement of a permanent magnet helicon plasma thruster. *Journal of Physics D: Applied Physics*, 46(35):352001, 2013.

[124] Kazunori Takahashi, Christine Charles, Rod Boswell, and Akira Ando. Effect of magnetic and physical nozzles on plasma thruster performance. *Plasma Sources Science and Technology*, 23(4):044004, 2014.

[125] Kazunori Takahashi, Christine Charles, Rod Boswell, and Akira Ando. Adiabatic expansion of electron gas in a magnetic nozzle. *Physical review letters*, 120(4):045001, 2018.

[126] Kazunori Takahashi, Christine Charles, Rod W Boswell, and Tamiya Fujiwara. Electron energy distribution of a current-free double layer: Druyvesteyn theory and experiments. *Physical review letters*, 107(3):035002, 2011.

[127] Kazunori Takahashi, Aiki Chiba, Atsushi Komuro, and Akira Ando. Experimental identification of an azimuthal current in a magnetic nozzle of a radiofrequency plasma thruster. *Plasma Sources Sci. Technol.*, 25(5):055011, August 2016.

[128] C.A. Thomas, N. Gascon, and M.A. Cappelli. Nonintrusive characterization of the azimuthal drift current in a coaxial e cross b discharge plasma. *Physical Review E*, 74(5):056402, 2006.

[129] Koji Uo. Perpendicular temperature of the c-stellarator plasma. *Phys. Fluids*, 8(2):384, 1965.

[130] T Vialis, J Jarrige, and D Packan. Separate measurements of magnetic and pressure thrust contributions in a magnetic nozzle electron cyclotron resonance plasma thruster. In *Space Propulsion Conference*, 499, Seville, Spain, May 2018.

[131] Théo Vialis, Julien Jarrige, Ane Aanesland, and Denis Packan. Direct thrust measurement of an electron cyclotron resonance plasma thruster. *Journal of Propulsion and Power*, 34(5):1323–1333, 2018.

[132] R. Winglee, T. Ziemba, L. Giersch, J. Prager, J. Carscadden, and B.R. Roberson. Simulation and laboratory validation of magnetic nozzle effects for the high power helicon thruster. *Physics of Plasmas*, 14(6):063501, 2007.

[133] Thomas M York, Barry A Jacoby, and Pavlos Mikellides. Plasma flow processes within magnetic nozzle configurations. *Journal of Propulsion and Power*, 8(5):1023–1030, 1992.

[134] S. Yoshikawa, M. A. Rothman, and R. M. Sinclair. Absorption of ion cyclotron waves by one component of a two-ion plasma. *Phys. Rev. Lett.*, 14(7):214–216, February 1965.

[135] Jiaguo Zhang, Eckhart Fretwurst, Robert Klanner, Ioana Pintilie, Joern Schwandt, and Monica Turcato. Investigation of x-ray induced radiation damage at the si-sio2 interface of silicon sensors for the european xfel. *Journal of Instrumentation*, 7(12):C12012, 2012.

[136] Yunchao Zhang, Christine Charles, and Rod Boswell. Thermodynamic study on plasma expansion along a divergent magnetic field. *Physical review letters*, 116(2):025001, 2016.

[137] J. Zhou, G. Sánchez-Arriaga, E. Ahedo, M. Martínez-Sánchez, and J.J. Ramos. Collisional effects in non-stationary plasmas expansions along convergent-divergent magnetic nozzles. In *Space Propulsion Conference 2018*, 00332, Seville, Spain, 2018. Association Aéronautique et Astronautique de France.

[138] P. Zhu and R.W. Boswell. Observation of nonthermal electron tails in an RF excited argon magnetoplasma. *Phys. Fluids B*, 3(4):869–874, 1991.